The Henryk Niewodniczański Institute of Nuclear Physics
Polish Academy of Sciences

In-situ liquid cell TEM synthesis, dissolution and Au decoration of Ce_xO_y nanoaggregates with various oxidation states studied by XANES and STXM

Tomasz Roman Tarnawski

Thesis submitted for the degree of
Doctor of Philosophy in Physics

Supervisor:
prof. dr hab. inż. Magdalena Parlińska-Wojtan

Auxiliary supervisor:
dr hab. inż. Joanna Depciuch-Czarny

Kraków, 2025

I would like to express my gratitude to my Supervisors:
prof. dr hab. inż. Magdalena Parlińska-Wojtan and dr hab. inż. Joanna Depciuch-Czarny
for introducing me and guiding me through the world of nanotechnology
and liquid phase microscopy.

A special thanks to my collaborators and colleagues from Institute of Nuclear Physics PAS,
who made the last 4 years such an exciting and joyful adventure. Special thanks to
dr inż. Bartosz Klębowski, dr Wojciech Tomczyk and dr Mohammad Sadegh Shakeri
for their tips, help, support and contribution.

My gratitude goes also to all my colleagues and friends from
Fritz Haber Institute of the Max Planck Society in Berlin,
who made this adventure even bigger.

I would like to express my special gratitude to my friends, my parents, my sister
and my fiancée, who motivated and supported me during all this amazing time.

Acknowledgements

This work was founded by the grant from the National Science Centre 2019/35/B/ST5/04140. T.R.T. acknowledges financial support provided by the Polish National Agency for Academic Exchange NAWA under the Program STER - Internationalization of doctoral schools (Project PPI/STE/2020/1/00020 and BPI/STE/2023/1/00027/U/00001) for supporting his internship at the Fritz Haber Institute of the Max Planck Society. T.R.T. thanks the Institute of Engineering Materials and Biomaterials of the Silesian University of Technology for the use of the Titan FEI TEM instrument and the Biological and Chemical Research Centre, University of Warsaw, for the use of the Talos F200 FEI TEM instrument, built within the project co-financed by the European Union from the European Regional Development Fund under the Operational Program Innovative Economy, 2007−2013. This work was partially developed under the provision of the Ministry of Science and Higher Education project "Support for research and development with the use of research infra-structure of the National Synchrotron Radiation Centre SOLARIS" under Contract 1/SOL/2021/2. T.R.T. acknowledges SOLARIS Centre for the access to the ASTRA beamline and DEMETER/STXM beamline where the measurements were performed.

Streszczenie

Transmisyjna mikroskopia elektronowa z komórką cieczową (LC-TEM) jest jedną z najbardziej zaawansowanych technik obrazowania i analizy nanostruktur. Umożliwia rejestrowanie w czasie rzeczywistym wzrostu oraz ewolucji materiałów we wnętrzu miniaturowego reaktora. Kluczowym wyzwaniem w badaniach LC-TEM jest radioliza wody, proces, w którym wiązka elektronowa generuje rodniki mogące prowadzić do niezamierzonych przemian chemicznych.

Niniejsza rozprawa doktorska przedstawia dogłębne badanie nanochemicznych procesów indukowanych przez wiązkę elektronową na konkretnym nanomateriale – nanocząstkach tlenku ceru (Ce_xO_y NPs). Skupia się na analizie wpływu wiązki na rozpuszczanie, stabilność i mechanizmy syntezy nanocząstek jak również jej wpływu na zastosowanie katalityczne nanocząstek po dekoracji nanocząstkami złota (Au). Poprzez badanie tych interakcji, praca ta ma na celu udoskonalić metodologie stosowane w mikroskopii elektronowej *in-situ* oraz dostarczyć wgląd w reakcje chemiczne zachodzące w nanoskali w czasie rzeczywistym. Dzięki systematycznej analizie efektów działania wiązki elektronowej, udało mi się opisać wpływ takich czynników jak doza elektronowa, pH roztworu oraz dynamika przepływu cieczy. Opisana analiza dostarcza nowych wskazówek, pomocnych w usprawnianiu badań LC-TEM.

Jednym z kluczowych eksperymentów przeprowadzonych w ramach badań była synteza nanocząstek tlenku ceru z roztworu prekursora w środowisku LC-TEM. Wyniki pokazały, że wiązka elektronowa może pełnić rolę czynnika redukującego w procesie formowania nanocząstek, wpływając na ich rozmiar, morfologię i krystaliczność. Ponadto, zbadane zostały efekty związane z różnymi przepływami cieczy. Wykazałem, że dostosowując przepływ można kontrolować kinetykę rozpuszczania się nanocząstek, co stanowi kolejną ciekawą strategię dla obrazowania w czasie rzeczywistym.

Istotnym elementem badań było dekorowanie nanocząstek tlenku ceru nanocząstkami złota (Au NPs) w warunkach dynamicznych (przy ciągłym przepływie roztworu) i statycznych (bez przepływu). W pierwszym, Au NPs wykazywały większą tendencję do agregacji, tworząc duże skupiska na powierzchni ceru. Z drugiej strony, w warunkach statycznych obserwowałem głównie mniejsze i bardziej równomiernie rozmieszczone nanocząstki złota.

W ramach testów aktywności katalitycznej nanosystemu przeprowadziłem reakcję utleniania etanolu (EOR). Dekorowane złotem nanoagregaty wykazały wyższą wydajność niż katalizator z czystego złota, co sugeruje, że zachodzi efekt synergii pomiędzy podłożem z tlenku ceru, a złotem. Dodatkowo, zmiany stanu utlenienia ceru w nanokatalizatorze zostały zbadane i omówione. Wysoka jakość nanokatalizatora została również potwierdzona trzygodzinnym eksperymentem z użyciem cyklicznej woltamperometrii oraz spektroskopii absorpcji w podczerwieni *in-situ.* Badania wykazały, że analizowany system skutecznie utlenia etanol, prowadząc do intensywnej generacji CO_2.

Rozprawa ta poszerza wiedzę na temat procesów nanochemicznych indukowanych przez wiązkę elektronową w środowisku ciekłym, ze szczególnym uwzględnieniem układów katalitycznych opartych na tlenku ceru. Prezentuje nowe metody eksperymentalne i sposoby, co stanowi wartościowy wkład dla dziedziny LC-TEM. Opracowane strategie mogą pozwolić na większą kontrolę procesów nanochemicznych i bardziej wiarygodną interpretację danych, co pomoże w dalszej optymalizacji technik mikroskopii elektronowej *in-situ*.

Abstract

Liquid cell transmission electron microscopy (LC-TEM) is one of the most advanced techniques for imaging and analysing nanostructures. It allows to conduct chemical reactions in a tiny reactor and register in real time the growth and evolution of the materials inside it. A key challenge in LC-TEM studies is the radiolysis of water, a process wherein the electron beam generates reactive radical species that can drive unintended chemical transformations.

This dissertation presents an in-depth investigation of electron beam-induced nanochemical processes on a specific nanomaterial: cerium oxide nanoparticles (Ce_xO_y NPs). I focused on understanding how electron irradiation influences the dissolution, stability, and synthesis mechanisms of nanoparticles and their catalytic applications, when decorated with gold (Au) nanoparticles. By exploring these interactions, the study aims to refine the methodologies used in *in-situ* electron microscopy and provide insights into real-time chemical reactions at nanoscale. By systematical analysis of the beam-induced effects, I describe the influence of such factors like electron dose rate, solution pH and liquid flow dynamics. With this analysis, I provide new insights, which can be helpful in improving the LC-TEM methodology and the accuracy of *in-situ* experiments.

One of the central experiments of the research involves synthesis of cerium oxide nanoparticles from a precursor solution within the LC-TEM environment. The results demonstrate that electron beam irradiation can serve as a reducing agent for nanoparticle formation, influencing their size, morphology and crystallinity. Furthermore, the effects of different liquid flowing conditions in LC-TEM were investigated. It has been shown, that by adjusting the flow rate, the dissolution kinetics of ceria can be controlled, which is another interesting strategy for real-time imaging.

A crucial aspect of the research is the decoration of cerium oxide nanoparticles with gold nanoparticles (Au NPs) using both static and dynamic conditions in LC-TEM. In dynamic conditions, with continuous solution flow, Au NPs tend to aggregate more, forming larger clusters on the ceria surface. On the other hand, under static conditions, we observed mostly smaller and more uniformly dispersed Au nanoparticles.

For the analysis of catalytic activity of the examined nanosystem, the ethanol oxidation reaction was performed. The ceria nanoaggregates decorated with Au NPs exhibited higher efficiency, than pure Au catalyst, which suggests that there is a synergetic effect between ceria support and Au NPs. Furthermore, the evolution of the oxidation state in the nanocatalyst was investigated and discussed. High quality of the nanocatalyst was proved also by 3-hours long experiment using cyclic voltammetry and in-situ infrared reflective absorption spectroscopy. It showed that the studied system efficiently conducts full ethanol oxidation, leading to high CO2 generation.

Presented research advances the understanding of electron beam-induced nanochemical processes in liquid environments, with a particular focus on cerium oxide-based catalytic systems. It shows new experimental methods, which is a valuable contribution to the LC-TEM field. The presented strategies can be helpful in controlling nanochemical processes and data interpretation, which will be valuable for further optimization of *in-situ* TEM.

Table of contents

List of abbreviations

ATR – attenuated total reflection

BF – bright field

CE – counter electrode

CV – cyclic voltammetry

DFT – density functional theory

ECSA – electrochemically active surface area

EDS – X-ray energy dispersive spectroscopy

EOR – ethanol oxidation reaction

EXAFS – extended X-ray absorption fine structure

GCE – glassy carbon electrode

HAADF – high-angular annular dark field

HR-TEM – high resolution transmission electron microscopy

IRRAS – infrared reflective absorption spectroscopy

LC – liquid cell

LC-TEM – liquid cell transmission electron microscopy

NAs – nanoaggregates

NPs – nanoparticles

RE – reference electrode

SEM – scanning electron microscope

STEM – scanning transmission electron microscope

STXM – scanning transmission X-ray microscope

TEM – transmission electron microscope

WE – working electrode

XANES – X-ray absorption near edge structure

XAS – X-ray absorption spectroscopy

Motivation

The advancement of nanotechnology relies on the ability to observe and understand processes occurring at the nanoscale in real time and under realistic conditions. Among the most powerful techniques that allow such investigations is **transmission electron microscopy (TEM),** which provides excellent insight into nanostructures morphology and crystallinity. Using the electron beam as a scanning beam, with the accelerating voltage of 200 000 or even 300 000 V results in image resolution down to several picometres (10^{-12} m), which is a remarkable opportunity for analyzing nanomaterials. However, the electron microscope requires keeping a high vacuum environment inside the apparatus, which makes it unable to observe chemical reactions of nanomaterials in liquid in real time. This is a strong limitation for the development and understanding on nanochemical processes. In order to overcome that limitation, scientists developed a technique, which employs a tiny reactor (only few microliters of volume) that can be equipped with an electron-transparent membrane and installed inside the microscope. In such reactor it is possible to perform reactions and record the images in real time. This novel technique is called liquid cell transmission electron microscopy **(LC-TEM)**. It provides unprecedented insights into the nanoparticle synthesis and evolution in liquid environments. Functional nanomaterials get more and more interest both in research and in industry, but further advances in this field are not possible without precise characterization methods. For this reason, LC-TEM seems to be very valuable technique that will provide completely new insights into nanotechnology. It enables direct visualization of chemical reactions and interactions between nanoparticles in the liquid phase in real time.

Among different applications, electrocatalysis is one of the most desired fields, in which nanosystems can be employed. Modern, cost-effective nanocatalysts can play a crucial role in many branches of industry, supporting the environmental remediation, development of alternative fuel cells and sustainable fuel production. The ability to design catalysts with enhanced activity, stability and selectivity towards ethanol oxidation reaction (EOR) is a key challenge in modern chemistry and materials science. The best results are obtained with catalysts based on noble metals, such as gold (Au), platinum (Pt), and palladium (Pd), but such solutions are highly expensive. Therefore, researchers work on alternative catalysts – by combining the noble metal with a support made of some cheaper material. This approach reduces the amount of expensive material in the resulting catalyst, but more importantly – some metal oxides are reported to induce catalytic activity of the catalysts. Cerium oxide (Ce_xO_y or ceria) is one of such materials. Ceria-based catalysts have gained significant attention due to their ability to enhance the performance of noble metal catalysts. The incorporation of CeO_2 into catalytic systems offers several key advantages: lower cost, improved stability, unique redox properties, increased oxygen storage capacity and enhanced catalytic activity. Ceria is able to switch between Ce(III) and Ce(IV) oxidation states, releasing oxygen in the electrochemical reaction. It supports significantly the oxygen mobility in the catalyst crystal lattice and provides active sites for catalytic process. Overall, the interaction between ceria and noble metals enhances catalytic activity and this makes ceria a promising candidate for energy-related applications, such as hydrogen production and fuel cells technology. And for better understanding of the synthesis dynamics of the ceria nanostructures, LC-TEM should be the perfect candidate.

In this dissertation I used a variety of advanced characterization techniques, but the crucial experiments were performed *via* **LC-TEM** being the central method. It is used to observe Ce_xO_y nanoparticle synthesis, growth, and degradation in real time within a liquid environment of both precursor solutions and water, enabling direct visualization of reaction mechanisms. **X-ray Absorption Spectroscopy (XAS)** provides global insights into the oxidation state and local electronic structure of cerium and gold in the nanocatalysts, revealing phase structure of the ceria and its changes induced by reaction conditions. **Scanning Transmission X-ray Microscopy (STXM)** was used to study the spatial distribution of elements and their crystalline phases locally for a single nanoparticle, providing information complementary to LC-TEM observations. ***Post-mortem*** **Electron Microscopy (HR-TEM, HAADF-STEM, and EDS mapping)** was applied to analyze the structural and compositional changes in nanoparticles after in-situ experiments, validating real-time observations. Furthermore, I used it to compare the nanostructures fabricated *in-situ* with the nanoparticles obtained *ex-situ*. **Electrochemical Analysis (Cyclic Voltammetry)** was used to study the catalytic properties of ceria-based nanostructures, providing information on their catalytic efficiency in ethanol oxidation reaction. Finally, *in-situ* **infrared reflective absorption spectroscopy** was used to analyze the products of the ethanol oxidation reaction. I performed the EOR during the IRRAS scanning in order to analyze the concentration of different oxidation products in real time during a 3-hours experiment.

This dissertation contains four main sections. In **Chapter 1**, a comprehensive introduction to the field of LC-TEM, functional nanomaterials and nanocatalysts is provided, outlining the motivation for studying ceria-based catalysts for EOR and the importance of *in-situ* characterization techniques. A detailed discussion on the obstacles emerging from LC-TEM experiments is included. Furthermore, advantages of ceria in catalysis and the challenges associated with its application in noble metal-supporting systems are also presented. **Chapter 2** presents the **experimental methods** used throughout the study, providing an overview of LC-TEM, XAS, STXM, cyclic voltammetry, *in-situ* IRRAS, and *post-mortem* electron microscopy techniques. The methodology for sample preparation, liquid cell assembly and data acquisition is described, ensuring reproducibility of the presented results. It also describes technical details of the devices. Finally, it describes the chemical compounds and their origin, used in this dissertation. In **Chapter 3**, the main **experimental results are presented and discussed**. The real-time observations of ceria nanoparticle transformations, gold deposition and electron beam-induced effects are analyzed in detail. The influence of pH variations, radiolysis effects and solution flow dynamics on nanoparticle behavior is explored, providing new insights into LC-TEM imaging artifacts and methods for their mitigation. **Chapter 4 summarizes** the key findings of the study, highlighting their implications for the field of nanocatalysis and *in-situ* electron microscopy. Future research directions are proposed, emphasizing the need of complex, systematic studies on flow rate, electron dose rate and exposure time during LC-TEM experiments. **Chapter 5** presents all of the literature positions used for this dissertation and results analysis, including scientific papers, theses and books.

1. Literature overview

1.1. Nanomaterials

It is generally acknowledged, that modern nanotechnology began when Richard Feynman gave his famous lecture: *There's plenty of room at the bottom* (Feynman, 1960). In this talk, he was discussing subjects like 'can we write the Encyclopaedia Brittanica on the head of a pin?' and how can we make a mechanism that would be small enough to swallow it and keep it permanently inside our body, so it could assist our organism. He was inspired by biological structures and mechanisms, and postulated, that the laws of physics do not forbid to build functional structures and devices on atomic scale. His statement was, that if physics and chemistry would cooperate, then physicists will be able to synthesize any chemical substances, they just have to 'put the atoms down where the chemist says'. He believed that such atomic-scale machines and devices could revolutionize medicine and computing sciences. One of the main problems, which suppressed such revolution was electron microscopy – scientists needed an ability to see what they are doing.

Parallelly, tiny microscopic machines started to appear in futurology and science fiction literature, and one of the earliest pioneers in that field was Stanisław Lem (*Eden* (1958) and 'the cloud' in *The Invincible* (1963), or molecular machines in *Summa technologiae* (1964)).

The word 'nanos' (derived from the Greek word for 'dwarf') refers to the order of magnitude 10^{-9}, indicating a scale of nanometers. It is worth noting, that the size of carbon atom is nearly 0.1 nm (or 1 Å). Consequently, materials described as *nanomaterials* or *nanoparticles* (NPs) are typically expected to have dimensions on the nanometer scale. While the size limit for a nanomaterial is commonly considered to be 100 nm (at least for one of its dimensions), this threshold is not universally agreed upon (Jeevanandam et al., 2018; Khan et al., 2019). The term 'nano-technology', however, did not exist until Norio Taniguchi used to describe some surface processes on semiconductors with micrometric or nanometric precision in 1974. His definition was as follows: "Nano-technology mainly consists of the process of separation, consolidation, and deformation of materials by one atom or one molecule" (Taniguchi, 1974). But it was not until the 80s when nanotechnology actually started to develop. Eric Drexler described a variety of tiny machines, built atom by atom, which could be used for medicine, data storage, environment protection and many more and he published it in the book *Engines of Creation: The Coming Era of Nanotechnology* (Drexler, 1986). Moreover, the discovery of fullerenes (Kroto *et al.*, 1985) and carbon nanotubes (Iijima, 1991) was a real proof, that structures in atomic scale are possible to fabricate and that they can offer remarkable electronical or mechanical properties.

1.1.1. What are nanomaterials?

Nanomaterials can exist in multiple forms, which are generally categorized as 0D, 1D, 2D and 3D (Alagarasi, 2013), according to how many dimensions has the nanomaterial, Figure 1. 0D stands for spherical nanoparticles, like fullerenes and quantum dots – one of the smallest structures that can be fabricated. 1D describes fibers, wires, tubes and rods. They may have a length of a fraction of millimeter, but the diameter of several nanometers and thus, they will appear as extremely long tubules. Carbon nanotubes belong to this category. Nanostructures can also have a form of flat plates, or vast layers with a single-atom thickness like graphene – those would be 2D nanomaterials. Also, nanoparticles can be deposited in as thin films (or coating) with several/several hundreds of nanometer thickness. Finally, 3D structures are used to describe the whole variety of complex or multi-walled nanoparticles, such as tetrahedra, cubes, pyramids, bipyramids, octahedra, dendrites, flowers and many more.

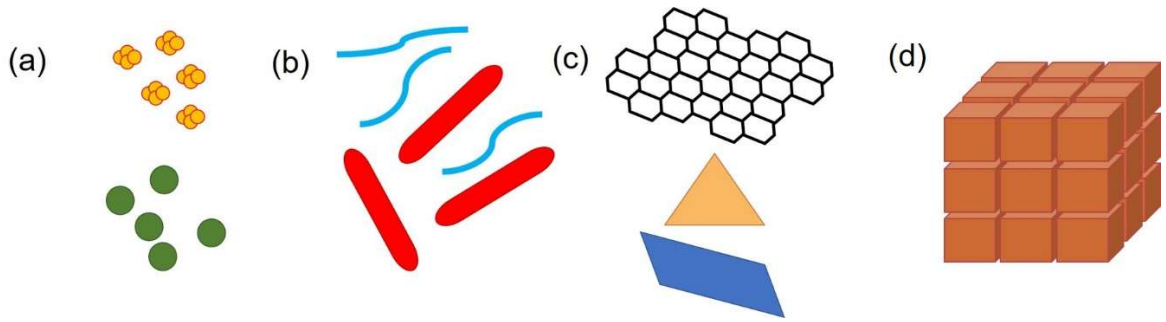

Figure 1 Classification of nanomaterials. Based on Alagarasi, 2013.

As mentioned before, nanomaterials are gaining significant attention due to their unique properties, which arise directly from their nanoscale dimensions. The 100 nm limit is not absolutely restricted – it is the size effects that matter. Unlike bulk materials, where properties are largely size-independent, nanoscale materials exhibit behaviors fundamentally shaped by size effects. These size effects, categorized as internal and external, as well as classical and quantum, play a critical role in defining the physical, chemical, and mechanical characteristics of nanomaterials (Pokropivny et al., 2007). Internal effects involve intrinsic property changes, such as variations in lattice parameters, melting points, hardness, band gaps and chemical activity, which occur independently of external interactions. External effects emerge during interactions between nanoscale building blocks and physical fields, when their dimensions approach critical lengths, such as the free paths of electrons or phonons. Classical effects result in altered hardness, plasticity or thermal conductivity, while quantum effects lead to phenomena like the quantum confinement effect, low-dimensional quantum states, and the quantization of conductivity (Sharma and Bhargava, 2013; Findik, 2021). These unique effects bestow nanomaterials with remarkable properties. Different types of nanomaterials demonstrate superior thermal stability, exceptional mechanical properties, optical properties or outstanding electrical performance (Sharma and Bhargava, 2013; Findik, 2021).

Furthermore, nanomaterials, due to their sizes, possess an exceptionally high surface area-to-volume ratio, which means, that most atoms in their lattice are located near the surface. It

results in stronger bonds in the structure, elevated surface energy and stronger chemical adsorption. These characteristics enhance extremely their reactivity and cost-effectiveness compared to larger counterparts, which makes metallic and metal oxide nanomaterials particularly advantageous for catalytic applications (Gawande et al., 2016). However, this effect is not absolute, smaller size does not increase the efficiency in every case, because the electronic structure and faceting of nanoparticles evolve as dimensions changes, and they are also vital parameters in catalytic activity (Gamler et al., 2018).

Summarizing, the unusual behaviors/properties of nanomaterials at nanoscale open up a spectrum of innovative applications, fundamentally redefining capabilities in science, engineering, and technology.

1.1.2. Synthesis of metallic and metal oxide nanoparticles

Methods for fabricating nanoparticles can be categorized in 2 main groups: bottom-up (chemical) and top-down (physical). In the top-down approach, scientists use powders or bulk materials and reduce their size into nanomaterials *via* chemical etching, sputtering, vapor deposition, laser ablation or grinding. However, those methods have lack of control on the precise morphology of resulting structures. Alternatively, in bottom-up approach nanomaterials are synthesized by chemical reactions. With variation of such parameters, like reagents concentration, time of reaction, temperature and pH, they allow to obtain a variety of shapes and sizes. These methods include: electrodeposition, sol-gel, microemulsion, microwave- or laser-assisted synthesis, solvothermal reaction and chemical reduction.

In any form, nanoparticles synthesis generally relies on a precursor – a chemical compound that supplies the necessary atoms for forming nanoparticles. For metallic and metal oxide nanoparticles, this precursor is typically a metal salt. The salt is being dissolved in a solvent with some additional reagents, depending on the reaction type. Those reagents may include surfactants, capping agents and reducing agents. Surfactants are introduced to inhibit the mutual aggregation of growing particles and separate them by mutual repulsion. Moreover, the surfactants may strongly influence the shape of the nanoparticles, due to steric interactions between surfactant and the surface of nanoparticles (Puntes et al., 2002; Vollmer and Janiak, 2011). Capping agents are used to modify the order of free energies for different crystallographic planes and suppress growth along some of them, blocking new atoms addition, allowing the growth along the others. At the same time, it can induce different reactions on the surface, e.g. oxidation, or atoms migration which also modify the structure evolution (Xia et al., 2009; Narayanan and El-Sayed, 2004). Examples of the capping agents might be CO (Spendelow and Wieckowski, 2004), H_2 (Harris, 1986), PVP (Sun et al., 2003) and bromides (Xiong and Xia, 2007). As far as capping agents can be added intentionally, they may also appear as some impurities or by-products (Xia et al., 2009). Finally, the reducing agent is an electron donor, which provides electrons to the reaction. It is the most important factor, which reduces metal cations back into atoms, allowing for the nucleation and growth of a nanoparticle (Reverberi et al., 2016).

Overall, it is acknowledged that certain metals and certain materials have a ‘habit’ of forming seeds and crystals in a characteristic shape (although it can be modified by the above-

mentioned additives) (Hulliger, 1994). But this habit can be influenced and triggered. If the rapidly growing edges align with the corners of a truncated cube, the resulting crystal shape will be a cube with its slower-growing planes forming the facets. Conversely, if the fast-growing edges correspond to the faces of a truncated cube, the final crystal will take the shape of an octahedron, with the slower-growing planes as its facets. This process allows for the selective expansion of certain crystallographic facets at the expense of others, by adding specific reagents, enabling the formation of new nanocrystal shapes (Xia et al., 2009).

Regardless of the method, we can differentiate nanoparticle synthesis into three main stages. In the first stage, **nucleation**, the precursor dissolves in water, breaking its chemical bonds and releasing metal ions. These ions must be reduced to zero-valent atoms, which then form nuclei (Xia et al., 2009). The nucleation process can vary depending on the pathway, such as the decomposition route, which follows the mechanism proposed by LaMer in the 1950s during their study on sulphur colloids (LaMer and Dinegar, 1950). Here, the concentration of metal atoms rises as the precursor decomposes (via heat or sonication), until it reaches supersaturation, at which point atoms cluster into nuclei. Alternatively, some researchers suggest, that precursor compounds can be directly converted into nuclei without going through the zero-valent atomic state (Xia et al., 2009). Despite significant efforts, studying and controlling nucleation remains challenging, partly due to limited experimental tools for capturing and analyzing nuclei (Oxtoby, 2000).

Once nuclei form, they collide and merge into clusters, increasing rapidly as metal atoms from precursor decomposition feed the process. This process continues until equilibrium is achieved between atoms in the solution and those on the surface. In addition to growth through atomic addition, nuclei can coalesce directly via agglomeration (Watzky and Finke, 1997). As clusters surpass a critical size, structural fluctuations diminish, stabilizing the cluster into a specific structure and marking the **seed formation** stage. Seed morphology is crucial, as it determines the final nanoparticle shape, and seeds' shape distribution depends on factors like thermodynamic stability. We can distinguish the following types of seeds: single-crystal, singly twinned, multiply twinned and plates. Typically, the most stable seeds dominate in the population, as predicted by Wulff's theorem, which seeks to minimize total interfacial free energy at a given volume. This interfacial free energy γ is determined by the surface area A and free energy per unit area G (Xia et al., 2009).

$$\gamma = \left(\frac{\partial G}{\partial A}\right)_{n_i,T,P} \tag{1}$$

In a face-centered cubic (fcc) structure with a lattice constant a, the surface energies of common low-index crystallographic facets can be approximated as follows: $\gamma_{[100]} = 4(\varepsilon/a^2)$, $\gamma_{[110]} = 4.24(\varepsilon/a^2)$ and $\gamma_{[111]} = 3.36(\varepsilon/a^2)$, resulting in the order of surface energy: $\gamma_{[111]} < \gamma_{[100]} < \gamma_{[110]}$ (Xia et al., 2009). This hierarchy suggests that single-crystal seeds will adopt octahedral or tetrahedral shapes to maximize the {111} facets and minimize surface energy (see: Figure 2).

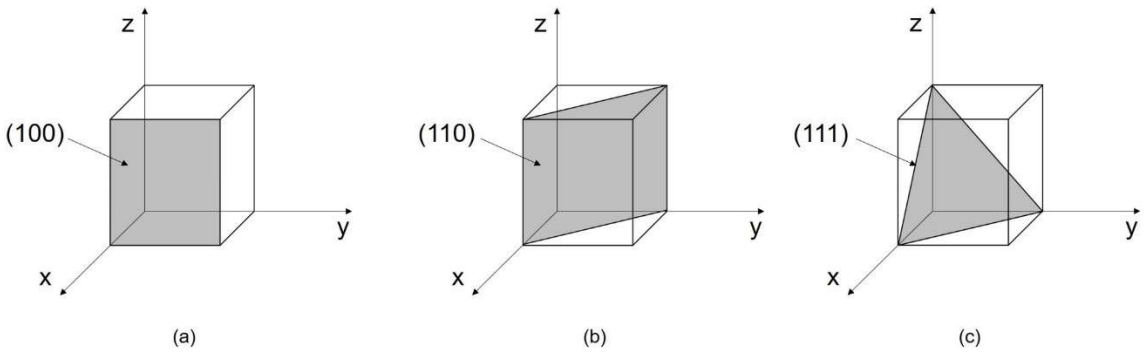

Figure 2 Miller indices for various lattice planes of the cubic crystal lattice. Based on Kinoshita, 2013.

However, due to their larger surface areas compared to cubes of equivalent volume, such seeds typically form truncated octahedrons (Wulff polyhedrons) enclosed by both {111} and {100} facets. These shapes are nearly spherical, minimizing the total interfacial free energy, and have been observed in numerous metal nanocrystal syntheses (Xia et al., 2009). The variety of nanocrystals' shape is presented in Figure 3. Depending on the growth rate along a specific axis, multiple structures can be obtained.

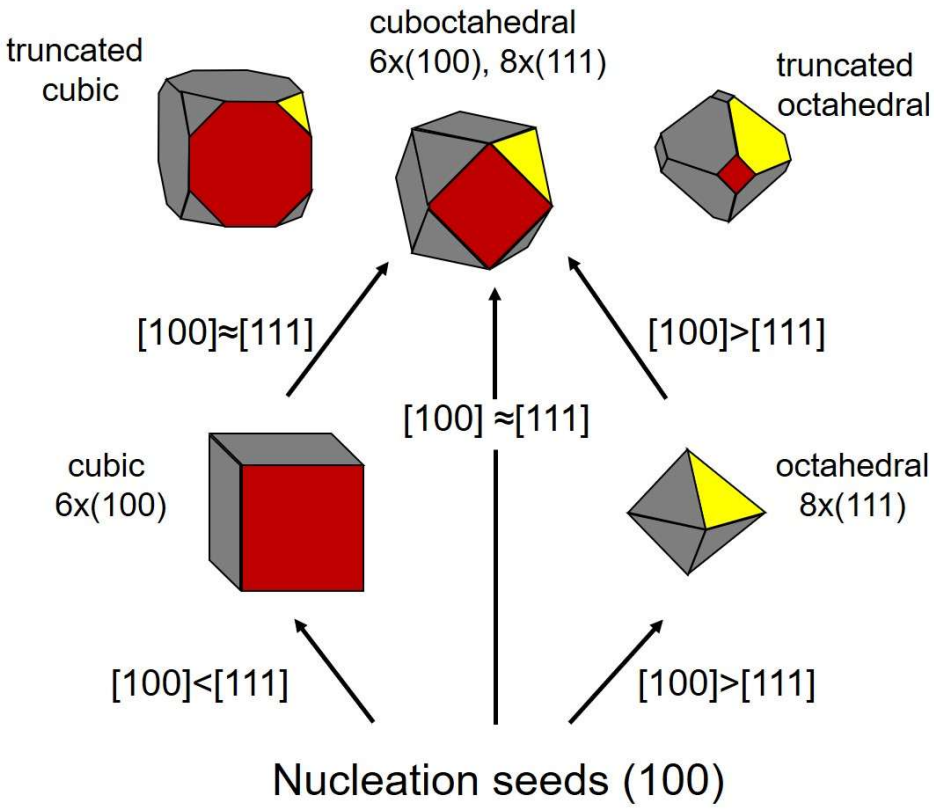

Figure 3 Schematic diagram of the shape evolution of a nanocrystal at different relative growth rates along the [100] and [111] directions. Based on Radi et al., 2010.

For multiply twinned seeds, the strain energy introduced by twinning can initially be offset by maximizing the {111} surface coverage, minimizing the total free energy when the seeds are small. If these seeds grow too quickly, however, the surface energy reduction from {111} facets can no longer counterbalance the strain energy, leading to their transformation into single crystals (Cleveland and Landman, 1991; Baletto et al., 2001). Thus, to maintain small multiply twinned seeds, the rates of atomic generation or addition must be carefully controlled. Slow metal atom generation promotes multiply twinned seeds over single-crystal ones, as their small size can be sustained longer. Singly twinned seeds may also appear, but in lower quantities due to the higher energy of their {100} facets. By adjusting the reduction or decomposition rates of the precursor, the population of seeds with different twin defects can be effectively controlled, which is the basis of kinetic control (Xia et al., 2009).

Unlike polyhedral seeds, plate-like seeds feature {111} facets on their top and bottom surfaces, with stacking faults or twin defects along the vertical axis. These seeds have a significantly higher total free energy due to their large surface area and defect-induced lattice strain, making them thermodynamically unfavorable. Producing plate-like seeds requires a departure from thermodynamic control during nucleation and growth. This can be achieved by strategies such as: 1) significantly slowing precursor decomposition or reduction (Ho and Chi, 2004), 2) employing a weak reducing agent (Washio et al., 2006) (exact role of a reducing agent will be further described below), 3) coupling reduction with oxidation (Xiong et al., 2005), or 4) utilizing Ostwald ripening (Sun and Xia, 2003). Regardless the strategy, concentration of metal atoms in the solution should be maintain an extremely low level. This helps to suppress autocatalytic growth into polyhedral shapes. Instead, atoms add to the edges of planar clusters, forming plate-like seeds. During metal nanocrystals formation, we also need to consider oxygen influence. Unless the reaction is performed in strictly controlled conditions without air exposure, O_2 may react with seeds and oxidize them back into metal ions – this effect is called oxidative etching (Wiley et al., 2004). Notably, single crystal seeds are more resistant to this effect than the twinned ones, since they do not have surface defects. The defect regions in twinned seeds have significantly higher energy compared to the single-crystal areas, making them particularly reactive towards the etching agent and thus, more vulnerable in oxidative conditions. Additionally, a ligand is needed to bond the released metal ion. By modifying the reaction solution with O_2 exposure and different ligands, we can manipulate the population of seeds, decreasing or increasing the concentration of single-twinned or multiply twinned ones (Wiley et al., 2004; Wiley et al., 2006a). On the other hand, we can provide a capping agent that will protect the seeds from surface oxidation (thus, etching) (Xiong et al., 2007), or provide an oxygen scavenger that will be more reactive towards O_2, eliminating the etching effects (Xiong et al., 2007; Tao et al., 2006).

As the specified seeds are formed and stabilized, the **growth of a nanocrystal** stage begins. It is a process of achieving a balance between bulk energy and surface energy. As the size increases, its surface energy also increases, which induces dissolution, hence crystals stop growing. On the other hand, bulk energy decreases, while adding new atoms to the crystal lattice, so it drives seeds to grow and minimize the energy of the system. Those are two main driving forces at this stage. Depending on the structure of a seed, they will induce them to grow in a specific way, as it was described above, eventually creating nanoparticles. In case of fcc metal crystals, for single-crystal seeds, growth along the {111} and {100} directions determines

whether octahedrons, cuboctahedrons or cubes are formed (Wang, 2000). If uniaxial growth occurs, cuboctahedral and cubic seeds can transform into octagonal rods and rectangular bars, respectively (Xiong and Xia, 2007). Singly twinned seeds typically develop into right bipyramids enclosed by {100} facets, resembling two right tetrahedrons joined base-to-base (Wiley et al., 2006b; Xiong et al., 2007). Under uniaxial growth conditions, these seeds may further evolve into nanobeams (Wiley et al., 2006a). Multiply twinned seeds yield structures such as icosahedrons, decahedrons and pentagonal nanorods or nanowires, depending on the stabilization of {100} planes on their side surfaces (Wiley et al., 2005; Murphy and Jana, 2002; Xiong and Xia, 2007; Sun et al., 2007). Seeds containing stacking faults, in contrast, grow into thin plates with {111} facets on their top and bottom surfaces and a mix of {100} and {111} facets enclosing their sides (Kirkland et al., 1993; Ho and Chi, 2004; Washio et al., 2008; Xiong et al., 2005; Sun and Xia, 2003).

There are also strategies to use pre-synthesized seeds or nanocrystals to trigger nucleation of a new metal on top of the previous one. When the added metal atoms adopt the same crystal structure as the introduced seed, the process is referred to as epitaxial growth. This typically occurs, when the seeds and growth atoms share the same chemical identity, although the final shape of the nanocrystal still may differ from the initial seed due to factors discussed before. Such approach frequently employed for growing Au nanorods from Au seeds (Jana et al., 2001), or nanostars from nanospheres (Becerril-Castro et al., 2022). Epitaxial growth can also occur between chemically distinct seeds and added atoms, a process more precisely termed heteroepitaxial growth (Xia et al., 2009). A critical requirement for heteroepitaxial growth is a close lattice match between the seed and the deposited atoms; for instance, Pd and Pt exhibit a lattice mismatch of only 0.77%. This method can yield bimetallic core–shell nanocrystals, where the core is formed by the initial seed (Habas et al., 2007). However, when the lattice mismatch is substantial (e.g., 4.08% for Au and Pt), heteroepitaxial growth becomes less favorable due to high strain energy, often resulting in non-conformal growth and unexpected nanocrystal shapes. Bimetallic nanostructures, like core-shell or decorated nanoparticles are highly desired, they mark the first step to create complex, functional nanosystems that could be used for multiple applications, from catalysis to medicine.

By adjusting the synthesis parameters described above, we can control the size and shape of the nanoparticles. On the other hand, in chemical methods there are many additional factors, such as pH, method of mixing, rate of oxidation, all of them also may influence the synthesis and they are complicated to control. Over the years, several strategies of synthesising nanoparticles were developed, using different reactions and different reducing agents – sometimes it can be simply a chemical reagent, but alternative strategies also exist. In the following section, we will discuss several selected synthesis methods.

Sol-gel – the precursor is dissolved either in an alcohol or in water. When water is used as the reaction medium, the process is referred to as the aqueous sol–gel method, whereas the use of an organic solvent classifies it as a nonaqueous sol–gel route. Hydrolysis of the precursors is facilitated by the addition of an acid or a base alongside the solvent. Initially, the solution undergoes hydrolysis, resulting in a mixture of hydroxides and forming a ‘sol.’ This is followed by condensation, during which molecules combine, solvents are removed, and metal atoms oxidize. Hydroxyl and oxygen bridges are established between metal atoms, leading to the

formation of a polymeric network that grows to colloidal dimensions. As condensation progresses, the viscosity of the solvent increases, producing a porous structure containing a liquid phase, referred to as a 'gel.' During the aging process, the gel thickens and pore size decreases. The next step involves drying to remove the solvents (water or organic), leaving behind the gel structure. However, this step may disrupt the gel's integrity, necessitating specific drying techniques such as supercritical drying, thermal drying, or freeze-drying, each of which impacts the structure differently. Despite these challenges, the desired gel structure can be preserved. The final step is calcination, which removes any remaining water or residues. This method offers excellent control over the material's texture and surface properties, making it highly suitable for fabricating metal oxide nanoparticles (Parashar et al., 2020). However, its multistep nature adds complexity, which is a drawback.

Microwave-assisted synthesis – here microwaves are used to induce the nucleation of nanoparticles. During the reaction, they interact with polar molecules, leading to the rotation and vibrational motion of these molecules and finally – generating heat within the material. In conventional processes, the heat transfer occurs from surface to bulk. This radiation causes rapid local overheating of the reaction mixture and ultra-fast synthesis of monodispersed nanoparticles. This approach can be used for fabricating various types of nanostructures, including tubes, platelets, films etc. The method is very fast and gives strong control over the resulting morphology. It also does not require using organic solvents, which is desired from ecological viewpoint. However, there are some strong problems with it as well: many authors do not describe precisely enough their equipment and set parameters, such as the type of microwave reactor, or temperature. Such lack of transparency and accuracy is highly problematic for reproducibility and understanding of the mechanism (Zhu and Chen, 2014).

Laser ablation synthesis in solution – method for producing nanoparticles through the condensation of a plasma plume generated by laser ablation of a bulk metal plate submerged in a liquid medium. It is generally recognized as a top-down physical approach, but it is also considered as a complementary strategy for bottom-up chemical synthesis. Key parameters influencing the process include the duration, wavelength and fluence of the laser pulses. Lasers with femtosecond (fs), picosecond (ps) or nanosecond (ns) pulses at visible or near-infrared wavelengths have been used for laser ablation, with fluences ranging from a few to thousands of J cm^{-2}. This versatile technique enables the synthesis of nanoparticles from various metals, including gold, silver, platinum and copper, in a single step, either in water or organic solvents. Additionally, nanoparticles with or without surface coatings can be produced using laser ablation. One notable advantage of this method is that it can produce nanoparticles that are stable in water or organic solvents without requiring stabilizing molecules or ligands. Despite its simplicity, the underlying physics and chemistry of the process remain complex. A significant challenge of this method is achieving precise control over the size and size distribution of nanoparticles, particularly in this ligand-free approach. However, size control can be also achieved through laser irradiation by leveraging plasmon absorption or interband transitions, eliminating the need for chemical reagents (Amendola and Meneghetti, 2009).

Electrodeposition – this is a unique synthesis method, which does not actually require any additional chemical compounds, apart from the precursor, because it employs electrical current for reducing metal ions. It is used for depositing metallic, metal oxide, or conductive polymer materials onto a surface by applying an electric field. The resulting structure can either be a continuous thin film or a film composed of nanoparticles. It does not require additional consolidation steps, making it an efficient and cost-effective process. In this approach nanoparticles are fabricated on the surface of an electrode, immersed in the precursor solution (i.e. electrolyte). One of the primary advantages of this method is that it offers a versatility of the morphologies through the tuning of electrochemical parameters such as current density and applied potential, which can significantly influence the characteristics of the final deposit. The composition of the electrolyte bath is another key factor, as it determines the properties of the deposited material. By incorporating various inorganic or organic additives into the electrolyte, one can further modify both the composition and morphology of the film. These additives can be used to achieve specific structural and functional properties in the deposit, such as enhanced mechanical strength, altered surface roughness, or improved catalytic activity. This level of control allows for the customization of materials to suit a broad range of applications. its high repeatability and the ease with which the deposition parameters can be precisely controlled. Furthermore, varying the concentration and chemical reactivity of the electrolyte solution can result in a wide range of deposition outcomes.

The electrolyte used in electrodeposition is typically a solution containing a salt of the desired material. The choice of salt plays a critical role, as different salts exhibit distinct chemical properties that influence the morphology of the resulting deposit. In cases where the salt concentration or conductivity of the solution is insufficient, an auxiliary salt may be added. The ions of the auxiliary salt do not participate in the deposition process directly but serve to enhance the overall conductivity of the solution, facilitating charge migration throughout the system. Usually a 3-electrode system is used for electrodeposition: working (WE), counter (CE) and reference (RE) and those 3 electrodes are connected to an external potentiostat. When voltage is applied, metal ions are forced to reduce on the WE surface. Depending on the material and precursor, we can use constant voltage to synthesise the nanostructure (metals do have their characteristic reduction potential). If we want to create an alloyed nanostructure of several different metals, we can use cyclic voltammetry – in this technique the potential is varied in a certain range that covers the reduction potentials of every metal used in the reaction. The process of electrochemical deposition involves two critical stages: first, the formation of a large number of nuclei, and second, the regulated growth of these nuclei (Natter and Hempelmann, 1996). These steps rely heavily on careful optimization of chemical and physical parameters. A key factor in this process is the overpotential – in electrochemical terms, it represents the voltage difference between a theoretical reduction potential and the actual potential observed during a redox reaction. Its level significantly influences the size and density of the nuclei. Higher overpotential leads to smaller nuclei and increased current density, which in turn accelerates the rate of nuclei formation (Jayakrishnan, 2012). The electrodeposition method is particularly convenient, because it requires minimal initial investment, supports rapid production, and is adaptable to a wide range of shapes and sizes (Palumbo et al., 1991; Bakonyi et al., 1993). However, it creates a film of nanoparticles that are strongly adhered to the

electrode surface. It is perfect for some applications (like electrocatalysis), but is highly problematic, if we want to recover the nanoparticles for further reactions or experiments.

Chemical reduction – here the reducing agent is the crucial reagent. This is an extremely common approach, which allows to fabricate nanoparticles of multiple elements, sizes and shapes. In many cases the reactions are very simple and quick, can be conducted in room temperature and they do not require sophisticated or expensive chemicals. The precursor can be dissolved both in aqueous or organic solvent, the choice of reductants is very wide, similarly like the surfactants. The reactions can be performed in ambient atmosphere, unless we definitely demand to obtain metallic nanoparticles (without oxide phases). For the reducer, such compounds like sodium borohydrate ($NaBH_4$), hydroxylamine, ethylene glycol, hydroquinone, gallic acid, citrates, aldehydes, secondary alcohols, monosaccharides, ascorbic acid and many more (LaMer and Dinegar, 1950; Henglein, 1989; Schmid, 1992; Mitchell, 1997; Watzky and Finke, 1997; Wang, 2000). The choice of a reducing agent for specific reaction depends on the operating conditions, desired nanostructure and the precursor itself (Din and Rehan, 2017; de Souza et al., 2019). It was reported, that e.g. by changing the precursor salt we obtain nanoparticles of completely different sizes, which is determined by the ability of precursor ligands to stabilize the particles. Due to the ability to create stable complexes with metal ions, some precursors lead to better control over the particle nucleation and protect them from agglomeration, keeping their low sizes. As for the solvent, the same team reported that using different solvents with the same precursor salt resulted in different morphology of nanoparticles: from spheres to multifaceted crystals (Niederberger et al., 2006). Moreover, for the surfactant there is also a wide variety of possible chemicals, again depending on the desired geometry of nanoparticles (Hofmeister et., 2002). Non-ionic surfactants, such as ethoxylated alcohols, ethoxylated amines, amine oxides and thiols, lack dissociable groups in their hydrophilic regions. This characteristic makes them less sensitive to electrolytes, allowing their use at high salt concentrations. Ionic surfactants, on the other hand, are categorized as anionic or cationic based on the charge of their hydrophilic regions. Common examples include alkyl sulfates (anionic) and alkyl-ammonium salts (cationic), which are frequently employed in metal nanoparticle synthesis. The hydrophilicity of these surfactants can be adjusted by modifying the length of their alkyl chains (Reverberi et al., 2016).

Thermal methods – for this reaction precursor is being dissolved in an organic solvent and next it is heated to high temperatures (usually above 100°C and under inert atmosphere to avoid oxidation of the synthesized nanoparticles (Watt et al., 2013)). As a solvent, toluene, benzene derivatives, or ethylene glycol may be used. Sometimes a surfactant is also added to the reaction solution. Notable advantages of the thermal synthesis methods are a narrow size range of the fabricated nanoparticles, which is favorable in most applications of nanotechnology. Additionally, thermal methods do not require using the reducing agent, because the solvent itself serves as the reducer and the high temperature triggers the reaction. This fabrication technique is simple, allows a satisfactory size and shape tuning and proved to be very efficient for noble metal zerovalent nanoparticles, such as Au, Ag, Pt etc. However, such reducer-free approach can be problematic for different metals and result in creating a mix of metallic and metal oxide phases in the nanoparticle (Reverberi et al., 2016).

1.1.3. Functional nanomaterials

During last few decades, nanotechnology developed widely, and nowadays nanoparticles are fabricated in enormous variety of shapes and structures, such as spheres, tubes, cages, dendrimers or films. Due to their nanoscale sizes, materials offer new properties, unavailable at the macro-scale, which justifies this great interest around them. Silicon and iron oxides or carbon nanostructures proved to be useful in electronics, titanium oxide nanoparticles are widely used in cosmetics and silver nanoparticles are commonly used for their antibiotic properties. Noble metal nanoparticles, like Pt or Au are commonly used for catalytic reactions in oxidation, fuel cells, CO_2 removal, water-gas-shift and many more.

However, we can fabricate much more complex nanosystems – we can modify the nanoparticles and tune their overall properties, so they can be used for some desired application. This is how we create **functional nanomaterials** – they are specially and intentionally designed for performing a specific function. Such adaptation may include modification of the surface with chemical ligands, biomolecules. Moreover, we can modify NPs with different metal oxides or different metals, creating bi- and multimetallic or multicomponent nanostructures, such as core-shell particles, Janus particles, decorated nanoparticles, or alloyed nanoparticles. All of those combined structures will be referred to as **nanosystems**. Various integration strategies have been developed to provide a variety of functionalities. Since each integration method has its own capabilities, appropriate selection of methods is necessary to obtain multifunctional NP agents with desired properties. Suitable structure and integration method should be chosen prior to the synthesis of multifunctional NPs, depending on the functions needed and types of basal materials. The selection of structure is critical because several properties of NPs, such as surface plasmon resonance and drug loading capacity, are affected by the size and shape of the NPs (Kim et al., 2018).

Chemical functionalization – this surface modification can be used to modify the reactivity of nanoparticles in certain reactions or tune their properties. For example, gold nanoparticles can be functionalized with carboxylic acid first and then with luminol. Luminol can undergo an oxidation and emit visible light. The Au-based nanosystem proved to be very efficient and the light emission was 9 times brighter than from pure luminol molecule. But the modification with acid was also needed, to enable stronger conjugation between nanoparticles and luminol (Roux et al., 2005). Similarly magnetic nanoparticles were investigated for fluorescent probes, by modifying them with fluorescent components (You et al., 2007). Moreover, nanoparticles can be modified with polymers. It provides them strong steric or electrostatic repulsion, preventing from aggregation, but can also help in various applications: polymer coatings can make nanoparticles more hydrophobic, less hydrophobic, more biocompatible etc. Polymers can also incorporate some functional molecules like drugs, dyes, or antibiotics/toxins, in order to release them in specific conditions. Polymers can be thermoresponsive or pH-responsive, again – for realizing some incorporated reagents (Kim et al., 2018). Another important example of chemical modification is carbon functionalization. Catalytic nanoparticles are commonly supported on carbon material like carbon black, nanotubes or fullerenes. They form a medium in which nanoparticles are deposited and

interconnected, which improves conductivity between them and the electrode. But this carbon support requires functionalization, e.g. to induce its solubility.

Multicomponent nanoparticles – as previously discussed, several strategies exist for fabricating nanoparticles with unique complex structures. The simplest approach involves synthesizing two distinct sets of nanoparticles, each composed of different materials, and subsequently mixing them. This method typically results in the decoration of larger nanoparticles with smaller ones, leading to structures often referred to as core-satellite nanoparticles or just – decorated nanoparticles. This technique offers considerable flexibility in the selection of nanoparticle combinations, as it does not require the formation of a direct interface between the two types of nanoparticles. The lack of strict interfacial requirements makes this method particularly versatile and accessible.

An alternative and more sophisticated strategy is heterogeneous nucleation, wherein one material nucleates and grows directly on the surface of another nanoparticle, forming a defined interface. This process is analogous to the heteroepitaxy previously discussed. Heterogeneous nucleation can yield core-satellite structures, but may also result in core-shell configurations. In core-shell nanoparticles, the core is entirely encapsulated by a shell of a different material, typically a metal or metal oxide. The nature of the resulting structure – whether core-satellite or core-shell–is largely determined by the interface energy between the two materials.

When the lattice mismatch between the core and shell materials is minimal, the interface energy is low, favoring the formation of a dense, uniform shell. This core-shell structure is one of the most widely studied and applied architectures in nanotechnology due to its stability and tunable properties. However, when the lattice mismatch is significant, it becomes energetically favorable to minimize the interface area, leading to the formation of satellite structures rather than a continuous shell (Kwon et al., 2015). In this case, we have a single nanoparticle core surrounded by multiple smaller nanoparticles, that do not cover the surface entirely. This unique morphology, also referred to as decorated nanoparticles, allows for further functionalization of the core surface and offers combined properties between the core and the satellites or between the satellites themselves.

Despite these challenges, it is possible to manipulate the process to overcome high lattice mismatches. Surface treatment of the core nanoparticles can suppress independent nucleation of the shell precursor, increasing the likelihood of achieving a uniform shell even under less favorable conditions (Ghosh Chaudhuri and Paria, 2012). This method exemplifies the adaptability of nanostructure fabrication techniques to overcome inherent material incompatibilities.

Another approach involves blending different elements to form an alloyed nanoparticle. Such alloy can take the form of a single-phase solid solution, in which various atom types are distributed randomly within the lattice structure, creating a random alloy. Alternatively, it may consist of a mixture of two or more metallic phases or intermetallic compounds with specific stoichiometric ratios and well-defined crystal structures (Gamler et al., 2018). The main reason that alloyed nanoparticles are interesting is because some metals are not able to mix at bulk scale – this effect is called phase miscibility – but they can form alloy structures in nanoscale. Such nanoparticles demonstrate improved functionalities compared to their individual components due to the synergistic effects of element mixing. As a result, metal alloy systems

are highly sought after for applications in plasmonics (e.g., Au–Ag) and electrochemical catalysis (e.g., Pt–Pd). They can be synthesized by a variety of methods, such as chemical reduction, electrodeposition (similarly like other multimetallic nanosystems) or galvanic replacement. For the chemical reduction, the main 'trick' to form an alloy with a mixed distribution of different elements is to reduce every metal from the reaction solution in a very similar rate, using one reducing agent. This can be achieved, if the metals have similar reduction potentials, but we can also tune their co-reduction potentials by adjusting the molar ratios or the type of precursor. It is worth noting, that not only nanoparticles can be created with such method but also different structures like nanowires, nanorods and more. Galvanic replacement is an alternative technique that allows to fabricate bimetallic nanostructures. Pre-synthesized monometallic nanoparticles with a defined composition and morphology are utilized as templates here. Subsequently, a metal precursor with a higher reduction potential will be introduced to these templates, partially replacing the original metal atoms and resulting in the formation of bimetallic nanoparticles. By adjusting parameters such as the morphology of the templates and the concentration of the metal precursors, bimetallic nanoparticles with complex structures, including hollow nanocubes and nanoshells, can be achieved. This approach offers a solution to the challenges inherent in achieving precise shape control during the direct synthesis of bimetallic nanoparticles. (Thota et al., 2018).

All of the above-mentioned methods to create multimetallic nanosystems have been successfully employed to create a wide variety of structures involving numerous elements and materials. Researchers have reported diverse configurations using these methods, highlighting their versatility and potential for tailoring nanoparticle properties for specific applications (Yu et al., 2005; Xu et al., 2007; Choi et al., 2008; Wang et al., 2009). These advancements continue to expand the frontiers of nanotechnology, offering innovative solutions for material science and engineering challenges.

1.1.4. Nanocatalysts

One of the most frequently discussed application of nanotechnology is catalysis. This may include energy conversion and storage, chemical manufacturing, biological applications and environmental technology (Laurent et al., 2008; Gawande et al., 2011). Studies prove that various nanomaterials can be employed in this field, such as nanocarbon, metallic nanoparticles, metal oxide nanoparticles and many more. This high popularity is determined by few factors. Firstly, nanocatalysts can be prepared using inexpensive, easily accessible metals, which makes them a valuable alternative for noble-metal catalysts that are conventionally indispensable and essential, e.g. copper oxides. Secondly, as discussed before, nanomaterials exhibit superior catalytic activity over the corresponding bulk materials, which is determined by their distinctive quantum properties (Gawande et al., 2016). However, this activity is not always directly determined by the size of nanoparticles. For instance, platinum (Pt) nanoparticles used in fuel cells for oxygen reduction reactions (ORR) demonstrate diminished catalytic efficiency, when their size falls below 2.5 nm. This drop in performance is linked to the stronger binding of oxygen molecules at the edge and vertex sites, which become more prominent in smaller particles (Shao et al., 2011). Additionally, nanoparticles smaller than 3 nm may experience

increased adsorption of hydroxyl groups, which block active sites and hinders catalytic activity (Mayrhofer et al., 2005).

Shape also plays a critical role in nanoparticle performance. Specific crystalline facets influence catalytic activity and selectivity. For example, Pt icosahedra enclosed by {111} facets exhibit approximately three times higher catalytic activity for ORR than Pt nanocubes bound by {100} facets. This improvement is attributed to the unique adsorption properties of low-index Pt surfaces and the surface strain induced by twin defects (Zhou et al., 2013). However, despite their superior initial performance, shape-controlled Pt nanocrystals face a major challenge: their structural instability under operational conditions. Over time, potential cycling can cause these nanostructures to shift into more stable, but less catalytically active morphologies, limiting their long-term effectiveness as ORR catalysts (Shao et al., 2016).

Although activity of non-noble nanoparticles works fine in some fields, there are also applications, in which the nanocatalyst still must be fabricated of Pt, Pd or Au. This includes catalysts for fuel cells. However, we keep using noble-metal nanoparticles as catalysts, but combined with different, cheaper material in a multicomponent nanosystem. By adding a co-catalyst based on a low-cost material to a noble metal, the overall performance could be maintained at the same level or even improved, while the costs would be strongly reduced. In this approach, we combine different functions of different materials in order to create a multi-functional catalytic system. For example, in 2009 Kowal and co-workers reported (Kowal et al., 2009) that combining Pt with Rh and SnO_2 gives very good results in fuel cells for ethanol oxidation, because Rh helps to break the C-C bond and SnO_2 effectively provides oxygen species for the oxidation (Idriss, 2004). Their system was one of the first multimetallic catalysts, that effectively completes the ethanol oxidation reaction to CO_2 in room temperature (Marinkovic et al., 2020). Similar strategies were discussed and investigated further by other researchers.

Alloyed nanocatalysts – the catalytic efficiency of alloys is attributed to two main phenomena: geometric (ensemble) effects and electronic (ligand) effects. Geometric effects arise from modifications in the spatial arrangement of surface atoms, which influence how reactants bind and dictate potential reaction pathways. Introducing a secondary metal into the surface alters the coordination environment of active sites, which can significantly affect how adsorbates interact with the catalyst. For instance, clustered active sites might encourage adsorbates to bind in bridge or hollow configurations, whereas isolated active sites limit adsorption to on-top positions, altering reaction dynamics accordingly (Liu and Nørskov, 2001). Additionally, the lattice mismatch between the alloy components plays a crucial role. When the deposited metal has a smaller lattice constant than the substrate, reduced orbital overlap strengthens adsorbate binding. Conversely, a smaller substrate lattice enhances orbital overlap, weakening the surface-adsorbate interaction (Sneed et al., 2015). Beyond performance, alloying improves electrocatalyst stability. For example, Pt-based alloys demonstrate greater resistance to CO poisoning and enhanced fuel cell activity compared to pure Pt. In some cases, alloying has been shown to improve durability and prevent oxidation of the metal surface during catalytic reaction. It also reduced the overpotential required for the reaction, making the process more efficient (Xu et al., 2012). However, challenges such as dealloying and dissolution of non-noble metals in acidic environments and under varying potentials raise concerns (Jia et al.,

2015; Jia et al. 2016). Strategies to mitigate these issues include optimizing particle size, enhancing porosity and maintaining the initial Pt mass (Gan et al., 2013).

Core-shell nanocatalysts – this kind of nanostructures is among the most effective nanocatalysts, offering high activity in various heterogeneous catalytic reactions. These structures rely on their shell to maintain the catalyst's stability, preventing the metallic core (e.g., Au, Ag, Pt, Ni) from aggregation or sintering into larger particles. By adjusting the shell's porosity and surface chemistry, molecular diffusion of reagents can be precisely controlled, enhancing solubility, biocompatibility, or adding unique physical and chemical properties (Caruso et al., 2001; Reiss et al., 2009; Schärtl, 2010).

Beyond single-core designs, multi-core nanocatalysts have emerged as promising alternatives. For instance, Song et al. encapsulated multiple palladium nanoparticles within mesoporous silica shells, achieving an impressive 99.5% yield within 3 minutes for Suzuki cross-coupling reactions (Chen et al., 2010; Chen et al., 2012). Similarly, gold nanoparticles trapped inside polymeric shells have shown remarkable performance in aerobic alcohol oxidation, achieving reaction completion within 30–120 minutes and turnover frequencies (TOFs) between 100 and 400 h^{-1}.

Other studies have demonstrated innovative synthesis methods and applications of core-shell structures. Tan and colleagues developed a silica core-shell nanocatalyst containing a confined gold nanoparticle, achieving efficient reduction of 2-nitroaniline to phenylenediamine by tuning the Au particle size through precursor concentration (Tan et al., 2010). Yang's research group encapsulated solid acid cores (polystyrene sulfonic acid resins) within silica nanospheres, producing hybrid catalysts with high activity and selectivity in acid-catalyzed reactions, suitable for sustainable chemical processes (Zhang et al., 2014a; Zhang et al., 2014b).

Moreover, Bao's team encapsulated iron nanoparticles within carbon nanotubes resembling pea pods, which effectively shielded the metal from harsh environments such as acidic media or contaminants like sulphur and oxygen. This configuration preserved high catalytic performance and long-term stability in oxygen reduction reactions (ORR), even under SO_2 exposure (Deng et al., 2013).

The flexibility of core-shell nanostructures lies in their ability to be tailored and functionalized for unique properties. However, the surface of the shell must have some level of porosity, enough for the reagents to reach and react with the core. Despite significant progress, the field of hollow core-shell nanostructures remains in its early stages. To address real-world demands, further advancements in designing more intricate structures and incorporating diverse core and shell materials are essential (Sun et al., 2015).

Satellite-core nanocatalysts – they are an alternative approach to enhancing catalytic performance. It involves supporting catalytic nanoparticles on the surface of larger nanoparticles or nanostructures, rather than enclosing them within porous shells. This strategy offers significant advantages, as it protects catalytic nanoparticles from aggregation without requiring protective coatings or shells that might block active surface sites or alter catalytic activity. Supported nanoparticles maintain high surface areas and provide multiple active sites for chemical reactions, ensuring high catalytic functionality (Huang et al., 2016). Notably, the spaces between satellite nanoparticles and the interfaces between these satellites and the core

nanoparticle surface act as "hotspots" with enhanced electromagnetic fields, leading to heightened localized surface plasmon resonance (LSPR) sensitivity (Höller et al., 2016). By tailoring the size, shape and distribution of the satellite nanoparticles and the core structure, these plasmonic effects–and consequently their properties–can be precisely controlled.

Decorating nanoparticles with catalytic satellites, has been explored for various catalytic reactions using diverse morphologies. Core nanoparticles can adopt shapes such as spheres, cubes, wires, rods or stars, while satellites may also take multiple forms (Gu et al., 2022). Interestingly, even monometallic core-satellite systems have been demonstrated, including systems where both the core and satellites are composed of the same material and they exhibited high catalytic activity. For example, Au core nanoparticles (50 nm) decorated with smaller Au satellites (13 nm) were utilized as nanocatalysts for oxygen reduction reactions (Noh et al., 2017). Studies showed that adjusting the distances between satellites enhanced plasmon coupling, resulting in increased catalytic efficiency. Additionally, these decorated systems exhibited significantly greater surface roughness compared to unmodified nanoparticles, further amplifying the active surface area and catalytic activity. Similar effects were observed and reported before (Yoon et al., 2012).

Heterogeneous systems, where satellites and cores are composed of different materials, have also demonstrated superior performance. Gold nanoparticles supported on cellulose nanofibers were shown to be highly effective for the catalytic reduction of 4-nitrophenol (4-NP) (Lam et al., 2012). Similarly, cellulose nanocrystals decorated with Au nanoparticles exhibited faster and more efficient catalytic reactions, while resisting aggregation–a key factor limiting the activity of pure Au nanoparticles (Wu et al., 2014). Another innovative system involved coating cellulose nanocrystals with polydopamine (PDA) before decorating them with Ag nanoparticles. The porous PDA structure enhanced Ag nanoparticle stability and dispersibility, significantly improving catalytic efficiency, compared to systems lacking PDA modification (Tang et al., 2015).

The influence of core morphology on catalytic activity has been also extensively studied. For example, Au nanoparticles with spherical, rod-like and star-shaped morphologies, decorated with ultrasmall Pt nanospheres, were evaluated for CO_2 reduction reactions. These studies confirmed the crucial role of surface area in determining catalytic performance (Kumar et al., 2017). Another notable example is a system combining magnetic core nanoparticles with a chitosan coating, upon which Au satellite nanoparticles were deposited. Notably, deposited Au nanoparticles were actually seeds – after deposition, authors provided fresh gold precursor and a reducing agent to grow the Au spheres bigger. The chitosan enhanced hydrophilicity, improved Au dispersibility, and facilitated the immobilization of Au nanoparticles. This design exhibited high stability and efficiency in reducing various organic contaminants (Hu et al., 2014).

A hybrid approach that merges core-satellite and core-shell concepts has also been proposed. In one study, large Ag nanoparticles (~50 nm) were encapsulated within a silica shell and subsequently decorated with tiny Ag nanoparticles (less than 5 nm). The porous silica shell enabled chemical molecules to access both the large Ag core and the tiny satellite nanoparticles, broadening the system's catalytic applications. This design demonstrated exceptional catalytic activity for rhodamine B (RhB) degradation, with rapid reaction rates and excellent recyclability (Mao et al., 2016).

These advancements underscore the versatility and potential of core-satellite nanoparticle systems for catalysis, demonstrating the critical role of structural and morphological tuning in enhancing catalytic efficiency and providing platforms for innovative applications in various chemical reactions.

1.1.5. Cerium oxide nanoparticles as a support for catalytic NPs

Cerium is a lanthanide metal, which has a fluorite crystal structure in its oxide form (see Figure 4(a)). Nanoparticles of cerium oxide (ceria), also retain this structure, which is the reason why it attracted such wide attention. In fact, this fluorite structure determines some unique catalytic and redox properties that are also observable at the nanoscale.

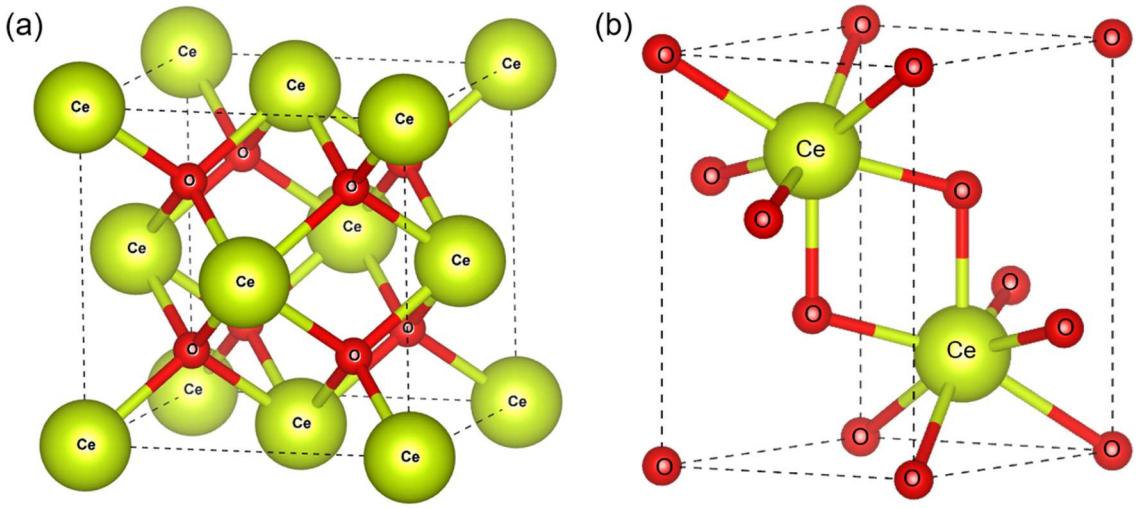

Figure 4 Cubic fluorite crystal structure of ceria.

Cerium oxide nanoparticles are characterized by oxygen deficiencies that create vacancies essential for redox reactions. The arrangement of surface planes in the fluorite structure – (100), (110), and (111) – plays a crucial role in determining catalytic performance, with each exposing distinct ion configurations (Nyoka et al., 2020). Specifically, the (111) and the (100) facets possess the o-terminal endings, while the (110) arrangement is characterized by the Ce center and the O ions (Huang and Gao, 2014; Yao et al., 2014). These structural properties make ceria nanoparticles valuable for industrial applications such as gas storage and catalysis. Their physical and chemical properties have been studied since the mid-20th century for a variety of industrial applications, such as the removal of carbon monoxide, hydrocarbons, and nitric oxide from exhaust gases (Kim et al., 2024).

Additionally, the appeal of ceria as an industrial catalyst lies in its abundance and economic competitiveness compared to noble metals. Cerium is relatively plentiful in the Earth's crust, its availability is similar to 3d transition metals such as Ni, Ti, Cr, Cu or Zn (Reed et al., 2014; Lawrence et al., 2011). This makes ceria an attractive material for catalysis – either as an alternative to noble metals or as a supportive component in catalytic nanocomposites, like the

nanosystems described above (Montini et al., 2016; Song et al., 2015). The insights gained from industrial research into ceria have significantly informed its application in research on catalysis and fuel cells. The catalytic activity and oxygen storage capacity of ceria nanoparticles are closely tied to their structural and redox characteristics. According to the Ce-O phase diagram (Okamoto, 2008), a 100% pure CeO_2 phase does not really exist under ambient atmosphere, due to a low oxygen vacancy formation energy (0.39 eV) (Huang et al., 2014). Ceria nanoparticles maintain a dynamic cycle of oxygen vacancy formation and re-oxidation, wherein two Ce^{4+} ions are reduced to Ce^{3+}, creating oxygen vacancies, and *vice versa* (Dutta et al., 2006). This process is influenced by particle size: smaller nanoparticles have a higher surface-to-volume ratio, which determines higher fraction of low-coordination surface atoms and weaker interatomic bonding. Hence, they exhibit more extended lattice structure. Ion diameter of Ce^{3+} is ca. 14% larger than Ce^{4+} (Shannon, 1976), and given the described lattice structure, it is more probable (more energetically favorable) for larger ions to be incorporated into smaller nanoparticles, resulting in higher Ce^{3+} / Ce^{4+} ratio in smaller nanoparticles. At the same time, incorporating more Ce^{3+} creates more oxygen vacancies (Deshpande et al., 2005). These defects, including Ce^{3+} and oxygen vacancy distribution, reportedly are correlated with the catalytic activity of ceria nanoparticles (Lawrence et al., 2011; Esch et al., 2005).

It is acknowledged that ceria has an excellent ability for redox reactions and it co-exists as a mixture of fluorite CeO_2 phase and hexagonal Ce_2O_3 phase (see Figure 4(b)). and that it can undergo spontaneous and dynamic phase transformations between cerium(III) cerium(IV) oxide (Ce_2O_3 → CeO_2). Surface Ce atoms with missing oxygen bonds facilitate the adsorption of oxygen species, stabilized further by nearby oxygen vacancies. This interaction enables oxygen vacancy filling and surface re-oxidation, which is a common mechanism observed with oxygen-deficient metal oxides (Kim et al., 2017; Pushkarev et al., 2004). The reaction equations are described as follows:

$$4Ce^{3+} \rightarrow 4Ce^{4+} + 4e^{-} \quad (2)$$

$$O_2 + 4e^{-} \rightarrow 2O^{2-} \quad (3)$$

Since stochiometric CeO_2 is thermodynamically unstable and tends to lose oxygen, those processes may continue according to the formula:

$$2O^{2-} \rightarrow O_2 + 4e^{-} \quad (4)$$

$$4Ce^{4+} + 4e^{-} \rightarrow 4Ce^{3+} \quad (5)$$

This will result in oxygen generation and Ce reduction back to Ce^{3+} and this system could work in cycles, but in reality, there are other species involved, such as O_2 or H_2O, which affect the system. Thus, reactions become more complex and harder to understand or model (Fronzi et al., 2009). There are, however, numerous models which, suggest that reaction temperature also has a significant impact on ceria's phase characteristics. Some researchers report that unstable C-type Ce_2O_3 forms at 800–900°C, while stable hexagonal Ce_2O_3 emerges at higher temperatures (>1000°C) (Perrichon et al., 1994). Temperature-programmed reduction

experiments have corroborated the following sequence: formation of oxygen vacancies at the surface, reduction of Ce(IV) into Ce(III) and diffusion of the vacancies into bulk material, shedding light on the dynamic phase transformation between CeO_2 and Ce_2O_3. But those models are not useful to explain redox mechanisms at low temperatures (Wang et al., 2009). And it is worth noting, that ceria gained a significant interest as catalytic materials partially for their high activity in low temperatures (Fu et al., 2001).

As mentioned, ceria's tendency to its unique surface properties and ability to spontaneous reoxidation, although still discussed by theoretical researchers, is very suitable for applications in oxygen storage and catalytic oxidation reactions. In fact, oxidation of CO using ceria has been investigated for a long time (Breysse et al., 1972). Such usages depend on its ease of releasing oxygen in a low oxygen environment, with simultaneous reduction of some Ce(IV) to Ce(III) on the surface and it is generally agreed, that those processes involve the participation of oxygen vacancies too. It can be found in multiple reports, that doping ceria with transition metals enhances its catalytic properties. Other studies focus on ceria-based catalysts interactions with noble metals, such as Au, Pd or Pt (Liu and Flytzani-Stephanopoulos, 1995a; Lai et al., 2006). And it was proved, that metal-modified ceria gives very good results in that field – the reducibility of a combined multimetallic catalyst is increased, as well as its oxygen storage capacity.

Gold nanoparticles supported on ceria are one of the systems that draws significant interest, mainly for its high activity towards CO oxidation and methane oxidation (Liu and Stephanopoulos, 1995a; Liu and Stephanopoulos, 1995b), high stability and low costs of ceria itself. Other applications of this catalyst include water-gas-shift reaction (Fu et al., 2001), hydrogenation reactions (Claus, 2005), hydrogen peroxide generation (Landon et al., 2002) and ethanol oxidation (Mullen et al., 2018).

Ethanol oxidation is a reaction involved in direct ethanol fuel cells (DEFC). It generates electrons *via* electrochemical oxidation of ethyl alcohol into CO_2. This reaction, however, is not favorable from kinetic point of view, and multiple by-products can be generated as well – those include acetic acid, acetic aldehyde or CO. Catalysts, such as gold supported ceria ($Au@Ce_xO_y/C$) are required to tune the reaction towards complete oxidation into CO_2 (which generates the highest number of electrons, and is therefore energetically the most desired outcome). There are several models explaining how exactly ceria can increase the oxidation efficiency, one of them being Mars – van Krevelen mechanism (Ross, 2018), which focuses on the CO conversion into CO_2. According to this theory, carbon monoxide adsorbs onto the catalyst surface as the catalyst reduces itself. The monoxide reacts with lattice oxygen and forms CO_2, creating oxygen vacancies. After that, O_2 molecules re-oxidate the catalyst and the process may be repeated. The reaction efficiency should depend on the carbon monoxide adsorption and the catalyst ability to form oxygen vacancies. As the literature says, the gold atoms can affect oxygen migration in the lattice, increasing the reducibility of ceria, which improves the efficiency of the Mars – van Krevelen mechanism. However, the implications of the ceria's phase transition on the catalytic activity of supported metal nanoparticles remain underexplored due to the instability of partially reduced ceria in oxygen-rich environments. Therefore, catalytic properties of ceria decorated with gold compositions and their metal-support interactions in ethanol oxidation reaction are being widely analyzed (Chen et al., 2008). In one report (regarding catalytic oxidation of an alcohol other than ethanol), the authors

proposed that the increased catalytic activity in Au@Ce_xO_y/C nanosystem was due to the generation of Ce^{3+} and Au^{+} sites on the catalyst's surface. These active sites facilitated the reaction's rate-limiting step, specifically the transfer of a hydride from the reactive intermediate (an alkoxide) to the catalyst surface (Abad et al., 2005).

Size of the ceria nanoparticles is one of the discussed parameters. Studies show, that nanocrystalline ceria support is far more active in oxidation reactions than microcrystalline ceria (Carrettin et al., 2004). Other scientists focus on the oxygen vacancy sites influence (Rodriguez et al., 2007). And multiple reports (including the above mentioned) show, that by modifying the nanostructure, we can manipulate the reducibility of ceria, which strongly influences the activity of the whole nanosystem. Overall, it is agreed, that multicomponent catalyst – ceria-supported Au – is one of the most active nanosystem in CO oxidation (Mullen et al., 2018).

These structural and redox properties highlight ceria support nanoparticles as versatile materials for industrial applications, offering a combination of economic feasibility, catalytic efficiency, and adaptability to various reaction conditions. Continued research into the interplay between oxygen vacancies, noble metal additives, Ce^{3+} distribution, and phase transformations promises to unlock new potentials for ceria-based nanomaterials in diverse fields. Such insight can be provided with utilizing microscopy techniques of *in-situ* imaging in real time.

1.2. *In-situ* liquid cell imaging techniques

1.2.1. Transmission electron microscopy and liquid phase electron microscopy

As it was mentioned, materials are commonly defined as nanostructures, if at least one of their dimensions is below 100 nm. The resolution of an optical microscope is limited to 200 nm, so in order to analyze nanomaterials, more a sophisticated technique is needed. The resolution of a microscope depends on the diffraction limit which was defined by Ernst Abbe in the XIX century (Abbe, 1882). The diffraction limit d is determined by the wavelength λ used for imaging and the numerical aperture NA and is expressed as:

$$d = \lambda/2NA \tag{6}$$

In order to reduce the diffraction limit, smaller wavelength should be used. Visible light wavelength is between 380 and 780 nm, but instead of light, a different kind of radiation may be used as well.

Electron microscopy uses high voltage and magnetic lenses to accelerate electrons and form them into a focused beam. From de Broglie equation, the wavelength of an electron will be defined as:

$$\lambda = \frac{h}{2meV^{1/2}} \tag{7}$$

where: h – Planck constant, m – electron mass, e – elementary charge, V – accelerating voltage (Fujiwara, 1961). Assuming V = 300 kV, a wavelength of 2.24 pm can be theoretically obtained.

Electron microscopy was developed by Ernst Ruska and Max Knoll, who captured first images in 1931 (Knoll and Ruska, 1932). Surprisingly, Ruska said that he did not know about de Broglie equation and wave nature of electrons, while working on his first electron microscope. Nevertheless, he and Knoll have proved that electrons can be used as an imaging beam and his achievement was honored with a Nobel Prize in 1986. Researchers have worked on developing this technology ever since, to increase the accelerating voltage and maximize its resolution. In 1937 British company Metropolitan-Vickers launched the first commercial electron microscope, EM1, but its image resolution was so poor, that the device was not really successful. In 1954 Siemens launched its Elmiskop 1, which was notably first high resolution commercially available electron microscope. With an accelerating voltage of 100 kV, it guaranteed the resolution of 1 nm (Ruska, 1956). Today, Transmission Electron Microscopes (TEM) use voltages up to 300 kV, which allows to achieve resolution of 2 pm, so imaging atomic structures became possible (Daigle, 2019). As such it remains one of the most advanced imaging techniques for nanomaterials studies.

Usually in TEM we use one of two modes of imaging: bright field and dark field. Bright field means, that the electron beam is focused into a very small spot, which is scanning over the entire sample, meanwhile the detector (which is located axially under the electron gun) registers the electrons reflected at small angles. In result, we receive a dark image in a background bright field (BF). Alternatively, electrons diffracted in the sample at high angles are registered by a circular detector, resulting in a bright image in a dark field and this mode is named high angle annular dark field (HAADF). Level of brightness in this mode (i.e. contrast) is proportional to the square of the atomic number Z^2. That way, areas with different chemical composition give different contrast and can be distinguished in this method.

Liquid cell transmission electron microscopy

Despite its unique advances, TEM has also its limitations. The analyzed samples must be thin enough to be electron transparent. Therefore, the sample thickness will be different for various materials, but usually should be below 1 μm (Carter and Williams, 2016). The other limit is that samples need to be imaged in vacuum, since electrons would scatter in air and that would damage the resolution. Hence, it is not possible, in a standard instrument, to observe chemical reactions inside the microscope. That was a huge problem for material scientists, biochemists and nanotechnologists. Numerous reports suggested, that more information about crystallization, degradation and particles interaction were needed for modelling reaction kinetics and understanding their dynamics (Yang et al., 2017; Chee et al., 2015; Zhu et al., 2014). This lack of knowledge on certain mechanisms in materials inspired scientists to develop a special device for this kind of observations.

In order to look into those processes, the TEM sample was placed inside a chamber, or rather a cell. If the cell could be fluxed with a solution, then imaging chemical reactions in TEM would become possible. However, there is still a problem of electron transparency. Actually, two things have to be considered: (1) transparency of the cell itself, (2) transparency of the liquid inside it. To achieve optimal resolution, it is essential to manage electron scattering caused by liquids effectively. The liquid layer within the cell must strike a balance: it should be

thick enough to allow the electrolyte to flow, yet sufficiently thin to enable the electron beam to pass through with minimal scattering. Additionally, the cell's windows on either side must possess enough strength to endure the external vacuum's pressure differential, while ensuring minimal interaction with the electron beam as it traverses.

One of the early ideas, was an open environmental chamber, which was developed by Ruska himself in the 40s (Ruska, 1942). He was using an open chamber, that was installed in the sample region and with a specially designed valve system, he managed to observe silver chloride synthesis in the gas phase. This system is nowadays used in SEM, where differential pumping is being used to keep low pressure on the sample and create a wet environment (Parsons, 1974;). However, it did not prove to be useful in TEM, because the thickness of the liquid layer in such open chamber was impossible to control and that was highly problematic.

A new approach was proposed by Abrams and McBain (1944) They prepared a closed 'sandwiched' cell, composed of two platinum circular discs, ca. 3 mm in diameter. Liquid was dropped on a bottom disc and then the cell was closed by the top disc and sealed with wax. Although they did not achieve high resolution, the idea was inspiring and during the next decades, researchers were developing this concept, searching for new materials that would be suitable for such 'liquid cell' construction. Today there are commercially available systems based on two silicon chips with a silicon nitride, electron transparent membrane approx. 30-50 nm thin. Such liquid cell is installed in a special holder, which allows to attach a syringe, providing constant solution flux. This is what we call now liquid cell transmission electron microscopy (LC-TEM). Alternatively, materials, such as graphene membranes, have also been investigated for their potential to create thinner, more electron-permeable windows. While these materials offer improved transparency to electrons, they come with the trade-off of increased fragility.

In a cross-section of a typical liquid cell is presented. Two E-chips with electron transparent membrane are visible and outside the cell there is vacuum. The membrane is made of silicon nitride (SiN_x) and its thickness is usually ca. 50 nm. One of the chips is equipped with spacers, that determine the thickness of the cell, typically from 1 μm down to 50 nm (de Jonge and Ross, 2011). Between the chips there is a liquid layer, which might be the precursor solution. Moreover, some LC-TEM holders are equipped with 2 inlet channels, which allows to use 2 different solutions simultaneously and mix them inside the cell – those can be a precursor and a reducing agent. In that case, it should be possible to capture the nucleation and growth of nanocrystals under the beam. Similarly, we can fabricate multicomponent nanoparticles inside the LC-TEM by one of the procedures: (1) deposition of pre-synthesized nanoparticles on the membrane and filling the cell with a precursor for the other component; (2) synthesizing nanoparticles of one component first and next filling the cell with a precursor for the other one; (3) synthesizing both components simultaneously inside the cell. The third approach can be used e.g. in electrodeposition. In this approach, the nanoparticles will crystallize on the chip surface and the ones that grew on the membrane will be possible to image by the microscope. There are also special types of E-chips, equipped with 3 electrodes (WE, CE and RE) with the WE located on top of the silicon nitride window. In such setup, it is possible to image the nanoparticles growing on the edge electrode. By connecting the LC holder to a potentiostat, we can apply voltage to the electrodes and perform experiments on the electrodes inside TEM: those include electrochemical measurements and electrodeposition. Overall, LC-TEM allows

to fabricate a variety of monometallic and multicomponent nanostructures (core-shell, core-satellite or alloys) and image their formation in real time.

Alternatively, the previously prepared nanoparticles can be deposited on the membrane (as it was performed by Abrams and McBain) and with a flowing liquid some chemical processes will be imaged, like corrosion, dissolution, migration, catalysis etc. In any case, the liquid cell allows to image the processes in real time, which is a huge advantage in nanotechnology field and provides valuable information (Radisic et al., 2006a; Radisic et al., 2006b). Overall, spatial resolution in LC-TEM is mostly determined by the electron interactions with the window and by electron scattering in the liquid. Therefore, many attempts have been made to minimize that effect. Reportedly, Zheng et al. (2009) were analyzing platinum nanocrystal synthesis in liquid cell and acquired resolution of 1 nm, using a system with 25 nm thin membrane and 100 nm high spacers. But reducing the thickness of the membrane obviously makes it more fragile. Additionally, lower spacers reduce the liquid volume, and as far as it is beneficial for the imaging quality, it may not accurately reflect actual reaction conditions of macroscale processes, especially when it comes to industrial catalytic reactions.

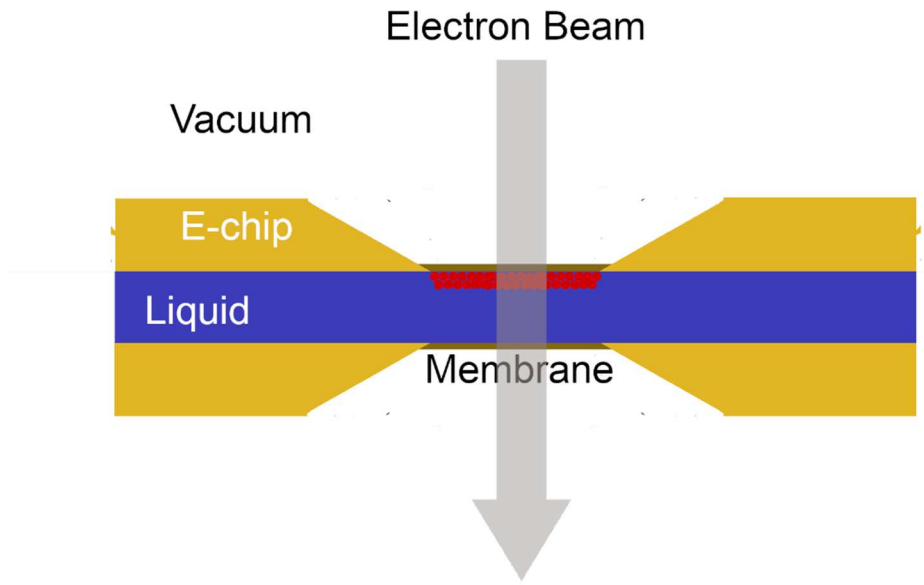

Figure 5 Cross-section of a liquid cell for TEM imaging (based on de Jonge and Ross (2011)).

Moreover, these imaging techniques also offer significant advantages by enabling the tracking of particle migration, aggregation and diffusion. Such observations enhance our understanding of reaction dynamics and refine theoretical models of synthesis, especially concerning the influence of electrochemical conditions and particle orientation (Radisic et al., 2006; Milazzo et al., 2017; Zheng et al., 2009; Oja et al., 2015).

Unfortunately, scattering effects are not the only challenge that must be taken into account. Experiments in LC-TEM present further obstacles connected to electron beam-induced water radiolysis. It can generate bubbles, alter the pH, disrupt nanoparticle growth, or even degrade materials (Jiang, 2017; Woehl and Abellan, 2017; Su et al., 2019).

A crucial parameter in LC-TEM is the electron dose rate, which indicates how many electrons from the beam illuminate a specific area per second, and it depends on beam current

and size of the imaging area. It is especially important during *in-situ* measurements. Electrons may cause water radiolysis and as a result, new agents are created, which are called here radical species. Among them, we can distinguish hydrated electrons e_h^-, H_2O_2, H_3O^+, H_2 and few more (this will be elaborated in further parts of this thesis). Those radical agents may directly damage the sample, modify the pH or increase the temperature. All of those effects will influence the processes and materials examined in LC-TEM (Cauzax, 1995; Garrett et al., 2004; Gao et al., 2018). The scale of that effect depends directly on the electron dose rate. There is a significant work of Schneider and co-workers, in which they were investigating correlations between the dose rate, radiolysis, pH and particle diffusion. As a result, they established complex theoretical models of electron-water interactions in liquid (Schneider et al., 2014). Notable statement that can be found in this paper is that resulting pH inside LC-TEM is influenced by dose rate and the solution's initial pH. At low electron doses, pH remains stable regardless of its initial level. At higher doses, however, behavior depends on whether the radiation-induced H_3O^+ concentration exceeds the initial H_3O^+ level. If so, the pH decreases as H_3O^+ concentration rises. For an initial pH of 3 or lower, pH remains stable even at high doses, but higher initial pH levels approach 3 as the electron dose increases. Hence, we have another trade-off here – reducing the current and electron dose rate would surely reduce the damaging effects of the beam, but it would limit the imaging resolution as well.

On the other hand, if the radiolytic effects are fully understood, they can be controlled and utilized for beam-induced synthesis. Several research teams have demonstrated the potential to use generated electrons as reducing agents to drive electrodeposition processes. In this method, hydrated electrons reduce metal cations to metal atoms, which subsequently cluster to form larger structures (Schneider et al., 2014). Such approach was also used to study hematite nanoparticles. Authors employed an electron beam with adjusted current to alter nanostructures by dissolving hematite nanoparticles. This process reduced their size, allowing researchers to manipulate their properties through controlled size modifications (Abellan et al., 2014). Similarly, hydrated electrons can serve as a reducing agent for simple chemical reduction. With increasing the electron dose rate (just by modifying the size of imaged area), it is possible to fabricate bi-metallic dendritic nanostructures with controllable rate. Reportedly, authors did not use any other chemical reducers (Weiner et al., 2016).

The final impact of an electron beam on a sample is determined by factors such as the material properties, the liquid environment (including parameters like pH), and the operating conditions of the microscope, such as magnification and beam current. This influence can either damage the structure, promote growth, or alter its morphology. The most effective approach to studying these effects would be conducting a series of *in-situ* experiments under a broad range of parameters. However, this method is time-consuming, technically challenging, and highly expensive. An alternative is to perform complementary *ex-situ* experiments that focus on specific reaction parameters. These experiments can yield valuable data and help validate mechanisms or hypotheses developed during *in-situ* studies, an approach adopted by some researchers (Gao et al., 2018).

Despite all the challenges, monitoring the formation of metallic nanostructures is highly valuable, especially in electrochemical research, due to the widespread application of metal and metal oxide nanoparticles in electronics and catalysis. Their unique physical and chemical properties support the development of nanoscale devices such as sensors, transistors, batteries,

fuel cells, and solar cells (Kleijn et al., 2014). For the last few years, scientists presented multiple reports on the nanoparticle's behavior in liquid. Many research teams managed to manipulate the growth of nanostructures using electron dose rate (Jungjohann et al., 2013; Gao et al., 2018). Several teams performed experiments that confirmed Schneider's model (Eskelsen et al., 2018). Nanoparticles evolution was investigated in LC-TEM to understand how temperature, precursor concentration or surface oxidation (Krans et al., 2019) influence the processes, presenting a deep analysis and vital results that would be very hard to draw without real-time imaging. Furthermore, degradation of nanostructures was investigated deeply, with capturing on which sites dissolution initiates and how it progresses (Wu et al., 2021; van Omme et al., 2020). By capturing such nanoscale insights into particle growth, aggregation, degradation and structural evolution during chemical processes, liquid cell imaging significantly advances the stability, efficiency, and overall performance of these technologies (de Jonge and Ross, 2011; White et al., 2012; Loh et al., 2017). Furthermore, combining *post-mortem* characterization (conducted *ex-situ*, both before and after the catalytic reaction) with LC-TEM analysis can corroborate findings by offering higher-resolution images of the structures involved.

In order to overcome described problems and difficulties, other techniques of real-time imaging are being developed and utilized in nanotechnology. Such combined tandem approach could help to fill the gaps in the research work.

1.2.2. Scanning transmission X-ray microscope

For chemical analysis of materials, X-ray absorption spectroscopy (XAS) is valuable and powerful analytical technique that investigates materials by scanning them with X-rays. When X-rays are absorbed by an atom, they excite core electrons (typically from the K, L, or M energy levels) into higher unoccupied states, resulting in an absorption spectrum that provides both electronic and chemical insights. This spectral information is centered around the absorption edge, which corresponds to the energy threshold required for these core-level excitations. The position of this edge is element-specific, scaling approximately with Z^2 (atomic number squared), making XAS particularly effective for studying multicomponent systems and identifying their elements (Timoshenko and Roldan Cuenya, 2020; Yang et al., 2023).

Typically, X-rays are categorized into ranges, depending on their energy, and their energy determines their penetration depth. Soft X-rays (200 to 2400 eV) penetrate only nanometers, while hard X-rays (>2400 eV) can reach micrometer depths. This property is dictated by Lambert-Beer's law, where the absorption coefficient (μ) depends on incident photon energy E, as well as material-specific factors like density ρ, atomic number Z, and relative atomic mass A. This is expressed by the formula:

$$\mu = \frac{\rho Z^4}{AE^3} \tag{8}$$

XAS measurements are often conducted at synchrotron facilities, which provide intense and highly collimated photon beams, enabling high signal-to-noise ratios unattainable with

conventional X-ray sources. The technique yields detailed structural information through its fine structures and the measurements can be separated into 2 types of complementary spectra: X-ray absorption near-edge structure (XANES) focuses on the range close to the specific absorption edge, from approximately 50 eV below it to 100 eV above the edge and it offers insights into the oxidation states and coordination environments due to the dependence of electron excitation on an atom's electronic configuration. It can be further divided into pre-edge region and the main edge or 3d transition metals, the pre-edge region corresponds to the quadrupole transition of an electron from the 1s orbital (K-shell) to a 3d orbital (M-shell). This transition is influenced by local and non-local mixing between the metal's orbitals and those of surrounding ligands, making the pre-edge a sensitive probe for electronic structure and coordination chemistry, particularly in catalysis (Timoshenko and Roldan Cuenya, 2020; Yang et al., 2023; Zimmerman et al., 2020).

The main edge of the XANES spectrum involves the dipole transition from the 1s → 4p orbital and transitions into the continuum for photon energies beyond the ionization energy. This region is crucial for elemental identification – spectra from known reference materials are compared to the experimental spectra, to identify unknown systems. Additionally, the position of the absorption edge provides insight into the oxidation state of the sample, as shifts in edge position correlate with changes in the oxidation state. Oxidation states are often determined by locating the maximum in the first derivative of the XANES spectrum, a common practice in analyzing chemical changes and redox processes (Timoshenko and Roldan Cuenya, 2020).

Extended X-ray absorption fine structure (EXAFS), observed several hundreds of eV above the edge, reveals spatial arrangements of neighboring atoms through oscillatory absorption patterns caused by photoelectron scattering. This allows quantitative analysis of parameters such as bond lengths, coordination numbers, and lattice structures, highlighting XAS as an invaluable tool in materials science and chemistry.

By utilizing an X-ray beam in microscopy, it is possible to correlate imaging with XAS spectra. In such a setup, the sample is scanned with a focused X-ray beam, a method known as Scanning Transmission X-ray Microscopy (STXM). This technique combines local X-ray absorption data (with energy resolution down to 0.1 eV (de Groot et al., 2010), although this value may vary between different absorption edges) with direct transmission imaging of the nanostructure (with spatial resolution of tens of nanometers). It provides spectral images containing both morphological and crystallographic information. This enables to determine atomic coordinates, electronic structure and crystal symmetry (Xu et al., 2024). By analyzing the obtained XAS spectra, we can identify the oxidation states in heterogeneous materials. Notably, XAS spectra of specific nanoparticles can be acquired individually, and multiple spectra from different locations within a single sample can be examined with this method. However, achieving high spatial resolution often requires prolonged acquisition times, typically ranging from minutes to hours, necessitating a trade-off between spatial and spectral resolution. Common approaches include obtaining a limited number of point spectra at selected regions of interest or imaging at a single wavelength, such as the material's white line.

Due to the minimal interaction between appropriately tuned X-ray beams and samples, XAS causes significantly less material damage compared to LC-TEM techniques. This advantage allows STXM to be used for real-time imaging in liquid environments. The technique, first conceptualized by Kirz and Rarback in 1985, has since evolved into a powerful

tool for analyzing thin samples, akin to TEM, to reduce beam scattering. Its application in *in-situ* studies began with the work of Drake et al. (2004), who used glass wafers to create an *in-situ* cell for studying the reduction and oxidation of a silica-supported Cu catalyst in a gas environment. Subsequent innovations, particularly by Adam Hitchcock's group, introduced electrochemical experiments using silicon chips with Si_3N_4 windows and integrated electrodes (Guay et al., 2005), achieving spatial resolutions of approximately 50 nm and sub-second temporal resolutions. Further advancements were made by Bozzini's team, who extensively utilized STXM for chemical and electrochemical studies (Bozzini et al., 2008; Bozzini et al., 2009).

Today, researchers frequently use STXM with the same liquid cell setups as those employed in TEM, facilitating cost efficiency and enabling data comparisons across methods. This unified approach minimizes experimental variations and enhances the robustness of conclusions. Modern STXM instruments, equipped with Fresnel zone plates, achieve focused beam spots as small as 10–100 nm, energy resolutions of approximately 0.1 eV at the carbon K edge and 0.3 eV at the copper L edge, and time resolutions of 1 ms per pixel. Operating primarily in the soft X-ray energy range (200–2400 eV), STXM systems are typically installed at synchrotron facilities, such as the National Synchrotron Radiation Centre SOLARIS in Kraków, Poland (DEMETER beamline). But to improve accessibility, laboratory-based X-ray sources like mini-synchrotrons are also being developed.

In-situ STXM excels at investigating electrochemical systems, including catalytic processes and electrodeposition reactions. It enables the study of reactive intermediates and the chemical evolution of nanostructures while delivering high-quality imaging. When combined with LC-TEM, STXM provides complementary insights into both the morphology and chemistry of observed processes, offering a more comprehensive understanding of physical and chemical transformations in nanostructures.

2. Materials and methods

All of the nanomaterials examined in this work were synthesized by the author. For the LC-TEM experiments the Poseidon holder was used, which is at the Department for Functional Nanomaterials. However, the TEM instrument was not available in IFJ PAN, therefore all the LC-TEM experiments were performed outside IFJ PAN. The author gained the necessary experience in operating the TEM during his STER internship at the Fritz Haber Institute in Berlin.

2.1. Reagents and chemical synthesis

As ceria and gold precursors, following reagents were used: cerium(III) nitrate hexahydrate $Ce(NO_3)_2 \cdot 6H_2O$, tetrachloroauric(III) acid $HAuCl_4$ x $3H_2O$. As a reducing agent, ethylene glycol was used. For cleaning and washing the nanoparticles, ethanol was used. As a carbon support for the nanocatalysts, Vulcan XC-72R was used, functionalized with nitric acid.

Ethylene glycol and nitric acid were purchased from Chempur (Piekary Śląskie, Poland). Ethanol was purchased from Poch S.A. (Gliwice, Poland). $Ce(NO_3)_2$ x $6H_2O$ was purchased from Alfa Aesar GmbH (Ward Hill, MA, USA). Vulcan carbon was purchased from Fuel Cell Store (Bryan, TX, USA). The rest of reagents were purchased from Sigma Aldrich (Burlington, MA, USA).

2.2. Experimental methods

Ceria nanoaggregates were synthesized by solvothermal reaction, in the absence of templates and surfactants. For this reaction, 60 mg of cerium nitrate hexahydrate was dissolved in 340 µl of deionized water and 8 ml of ethylene glycol was added. The resulting solution was sonicated for 30 min and then transferred into a Teflon-lined autoclave with capacity of 25 ml and heated for 16 h at 180°C. Finally, the liquid product was collected from the autoclave, centrifuged and washed with ethanol 3 times and dried at room temperature.

For Au NPs synthesis, 100 ml of 1 mM aqueous $HAuCl_4$ solution was added to a flask and heated until boiling. Then, 15 ml of a 1% trisodium citrate solution was introduced into the mixture, and the reaction proceeded for 15 minutes, during which the solution's color changed to dark red. The resulting NPs were purified by centrifuging three times in fresh distilled water at 15,000 rpm for 20 minutes.

For decoration of ceria with gold, both series of nanoparticles were dispersed separately in ethanol and sonicated for 30 min. Next, gold NPs solution was added dropwise into the ceria NPs solution while stirring on a magnetic stirrer. The resulting solution was then stirred for another 3 h in ambient atmosphere. Finally, $Au@Ce_xO_y$ powder was collected by centrifuging.

For catalysts fabrication, carbon black XC 72R was first functionalized with nitric acid in order to form functional groups on its surface. For this purpose, a beaker was filled with 0.7 M water solution of nitric acid and then, carbon black powder was added. The solution was stirred using a magnetic stirrer for 30 min in room temperature. Next, the product was washed in deionized water, until it reached a neutral pH (tested using pH indicator paper). After that, it was dried for 10 h at 100°C. Next step was supporting the nanocatalysts on carbon. The functionalized carbon powder was dispersed in water and the NPs solution was added dropwise during magnetic stirring. For 10 mg of carbon black powder, 10 mg of NPs was added. The resulting solution was stirred at room temperature for 12 h. Next, it was centrifuged and washed 2 times in ethanol, 2 times in water and finally, dried at 80°C for 10 h. After that, $Au@Ce_xO_y/C$ catalyst powder was collected.

For preparation of the catalyst inks, 2 mg of dried catalyst powder were dispersed in 120 µl of isopropyl alcohol, with 370 µl of ultrapure water and 10 µl of 5 wt % Nafion. Next, the ink was ultrasonically mixed for 30 seconds. After that, 10 µl of the resulting ink suspension was applied to a polished glassy carbon electrode (GCE), forming a thin, uniform catalyst layer after the solvent naturally evaporated in ambient atmosphere.

For characterization and analysis of the structure, morphology, composition and properties of the fabricated nanostructures, several methods were utilized. All of them are described in this chapter. Some of those techniques were also used for *post-mortem* imaging.

2.2.1. Scanning Electron Microscopy

After synthesis, scanning electron microscopy (SEM) was employed for imaging of the ceria nanoaggregates. It was important to investigate their morphology, size, surface structure and distribution on carbon. The instrument is located in Institute of Nuclear Physics and SEM imaging is generally quicker than TEM, so it was reasonable to image nanoaggregates here before any further experiments. For this purpose, Tescan Vega 3, equipped with tungsten filament operating at 30 kV with a maximum resolution 3 nm, was used. It is equipped with a secondary electrons detector and a scanning transmission electron detector, the latter one enabling imaging in bright field and dark field. Furthermore, energy dispersive spectroscopy maps were obtained at 10 kV for identifying local chemical composition.

2.2.2. Transmission Electron Microscopy

Both TEM mode and STEM mode were utilized and the samples were imaged in dark field and bright field. TEM images included in this thesis were obtained using a Cs aberration-corrected FEI Titan electron microscope operating at 300 kV equipped with a FEG cathode, which is located at the Materials Research Laboratory of the Silesian University of Technology in Gliwice, Poland. For chemical analysis, energy dispersive spectroscopy (EDS) maps were obtained using a Talos F200 FEI instrument operating at 200 kV equipped with a FEG cathode and the Super-X-in-column EDS detector, located at the University of Warsaw Biological and Chemical Research Centre. With those maps, gold distribution on ceria and ceria distribution on carbon support were precisely analyzed with high resolution. Samples for TEM were prepared by dropping a few microliters of nanoaggregates dispersed in ethanol on a Cu continuous carbon film coated TEM grid (300 mesh, purchased from Agar Scientific).

Images obtained in TEM mode and high-resolution STEM (HR-STEM) with the HAADF detector were used to investigate the morphology, crystallinity and size distribution of the obtained nanostructures. Distribution of the materials (gold on ceria and ceria on carbon) was also investigated.

For the *in-situ* TEM experiments, two sample holders were used. Experiments with ceria were performed using a Poseidon holder (Protochips, NC, USA) with two E-chips equipped with small 50-nm-thin silicon nitride window. Two E-chips sandwiched together create a small liquid cell (LC), which thickness is determined by the size of the spacers on the bottom chip. Two chips are assembled in the holder, along with an o-ring seal and protected by a top metal plate, see Figure 6.

Figure 6 Poseidon Select system for liquid cells consisting of: bottom plate of the holder, seal (the O-ring), bottom chip of the liquid cell (with 2 yellow spacers), top chip, and top plate of the holder. On the bottom plate of the holder 3 golden contact electrodes for electrochemical experiments are located. Reproduced from Tarnawski and Parlińska-Wojtan, 2024. Copyright 2023 Protochips.

Ceria NAs synthesis – for the first LC-TEM experiment, the liquid cell was filled with ceria precursor. Chips with 150-nanometres spacers were used. Poseidon holder was installed in the TEM and the scanning beam was employed as a reducing agent for ceria NAs fabrication.

Ceria NAs with ceria precursor – for the second experiment, pre-synthesized ceria nanoaggregates were dropped on the top chip, which was subsequently dried, and then the LC was assembled with ceria precursor, to check, if the nucleation will continue on the surface of the nanoaggregates.

Ceria NAs with water – chip with pre-synthesized ceria was used, but this time the LC was filled only with pure water, to investigate the dissolution effects induced by the beam. The LC was installed in the TEM and scanned with high electron dose rate of 9 $e^-/Å^2s$. Water flow was varied from 0.8 µl/s to 0.5 µl/s.

Ceria NAs decoration with Au NPs – pre-synthesized ceria NPs were deposited onto the SiN_x window, followed by the addition of 2 µl of a 100 mM $HAuCl_4$ solution. Next, the top and bottom chips were assembled in the TEM holder. Two variants of this experiment were performed.

For the **static** variant, $HAuCl_4$ solution was filled into the liquid channels of the holder without flow and the holder was placed inside the TEM. Once the microscope valves were opened and the sample illuminated, the reaction of Au deposition initiated. Note, that the sample was not moved during the imaging and there was no flow of the $HAuCl_4$ solution. The electron dose rate was set to 0.04 $e^-/Å^2s$.

For the **dynamic** variant, during imaging a 100 mM $HAuCl_4$ solution continuously flowed through the LC with a flow rate 1 µl/s, The electron dose rate was 0.04 $e^-/Å^2s$.

Ceria NAs decoration with Au NPs – the decoration was performed using constant flow of 0.1 mM $HAuCl_4$ solution, with the flow rate of 0.05 µl/s. The electron dose rate was 11 $e^-/Å^2s$. The rest of the procedures were the same as above.

All the LC-TEM experiments with ceria alone were performed in FEI Titan in Gliwice. The LC-TEM experiments with Au decoration of ceria NAs were performed in FEI Talos in Warsaw.

A study on the electrodeposition of a porous PtNi film was also performed and the results were published in *Nano Letters* (Parlińska-Wojtan et al., 2024), see the Appendix. For the electrodeposition, an electrochemical E-chip (EEC) was used, equipped with 3 Pt printed electrodes, which serve as WE, CE and RE. The WE is covered with a glassy carbon layer to induce the conductivity. For this kind of experiments, two types of LC holders were used – Poseidon and Hummingbird (Hummingbird Scientific, USA). The architecture of the electrodes is different in Hummingbird system than in the Poseidon system, but the general rule remains the same – both types of E-chips are equipped with 3 Pt electrodes, covered with glassy carbon. The holders were connected to the external potentiostat. Both systems were used for platinum-nickel nanofilm electrodeposition; experiments with Poseidon were conducted in FEI Titan (Gliwice). Additional experiments were performed with Hummingbird Scientific holder in the Interface Science Department at the Fritz Haber Institute of the Max Planck Society (Berlin, Germany) in collaboration with dr. See Wee Chee group. This collaboration was established by STER internship program from NAWA.

2.2.3. Energy dispersive X-ray spectroscopy (EDS)

This technique is used to analyze and quantify chemical composition of the sample. It can be performed either in TEM or in STEM mode. In the first case, it gives global information from the entire sample area illuminated by the parallel electron beam. In STEM mode, the beam is focused and gives local information from a point area of the sample. The physical basics of this measurement is the characteristic X-ray radiation, produced by the interaction of the electrons with the sample. When a high-energy electron beam hits the atoms, it knocks out electrons from the orbit, creating a free electron state. Electrons from higher orbit immediately occupy this free state and emit the energy difference as a characteristic X-ray wave. Those signals are registered by the EDS detector and are specific for each chemical element, according to the Moseley's law:

$$v = A(Z - b)^2 \tag{9}$$

where v – frequency of the observed X-ray emission line, A and b – constants determined by the type of line (K, L etc.), Z – atomic number (Moseley, 1914).

With the EDS maps, it was confirmed that gold nanoparticles decorated the ceria nanoaggregates and the distribution of ceria in Vulcan carbon was easily and clearly visualized. The maps were taken in the above-mentioned TEM Talos F200X FEI equipped with an integrated 4 silicon drift detectors (SDD) system for superior sensitivity (Super EDS).

2.2.4. X-ray Absorption Spectroscopy (XAS)

X-ray absorption spectroscopy is a well-established technique for analysis of the oxidation state. It uses a monochromatic X-ray beam for scanning the sample. The radiation energy is being absorbed by the atoms, inducing the electrons to jump from a core-level to an empty orbital. For the oxidation state analysis of the fabricated nanostructures, several XAS techniques were utilized. For measuring the oxidation state of the synthesized ceria globally, X-ray absorption near edge spectroscopy (XANES) measurements were performed. XANES covers energy range from 50 eV below to 100 eV above the main absorption edge (Zimmermann et al., 2020). In order to identify the oxidation state in the sample, a reference samples with clearly chemical compositions and oxidation states should also be analyzed and both XANES spectra need to be subsequently compared. Any change of the oxidation state (oxidation or reduction) will be visible as a shift of the X-ray absorption edge. The majority of XAS experiments are conducted at large-scale synchrotron facilities, which serve as highly brilliant photon sources, offering low divergence, high monochromaticity, and adjustable photon energy with intense output.

Using XANES, the concentration of Ce(III) phase and Ce(IV) phase in the synthesized nanoaggregates was quantified. Ceria precursor powder and commercially available CeO_2 nanoparticles (Biomus, Lublin, Poland) were used as reference samples. XANES spectra at the Ce L_3-edge were collected at the ASTRA beamline of the National Synchrotron Radiation Centre SOLARIS (Krakow, Poland) in transmission mode using a Ge(220) double crystal monochromator. To produce a monochromatized beam, slits were employed, and the beam size was adjusted to 7 x 1 mm. The ionization chambers and sample chamber were maintained at a pressure of 20 torr of argon. A thin layer of finely ground ceria powders was deposited on specially chosen Kapton tape. The Athena software was utilized for data processing and analysis.

For measuring the oxidation state locally, on specific nanospheres, X-ray absorption spectroscopy measurements were performed in the scanning transmission X-ray microscope (STXM) at one of the DEMETER beamline end-station, also at SOLARIS center. STXM microscopes usually cover energy range between 200 and 2000 eV (soft XAS) so it can be used to measure M edge of Ce and identify its oxidation state by the method of subsequent comparison. The samples in STXM are positioned at the focus of the Fresnel Zone Plate (FZP) are moved using a precise XY piezo scanner. To maintain the required positioning accuracy relative to the FZP, a two-channel interferometric system with differential sensor heads was employed. A photomultiplier tube (PMT) with a P-43 scintillator was used to detect the X-ray intensity passing through the sample. The resolution of the STXM images is ca. 30 nm. The transmission signal gathered in STXM was converted into optical density (OD), which reflects the sample's density or thickness, as well as its chemical composition of interest.

For XAS measurements, several samples were analyzed: (1) pre-synthesized ceria nanoaggregates, (2) ceria nanoaggregates decorated with gold, (3) catalyst supported on the carbon collected after the electrochemical experiments. The aim of those measurements was to investigate the evolution of ceria crystallinity through different processes.

2.2.5. Density Functional Theory

Simulations were performed to obtain the theoretical ceria XANES spectrum. Quantum Espresso (QE) software was used to relax the unit cell models of CeO_2 and Ce_2O_3 (Giannozzi et al., 2009; Giannozzi et al., 2017; Giannozzi et al., 2020). The DFT calculations began with atomic modeling of the cubic CeO_2 unit cell with space group $Fm\bar{3}m$ and the trigonal Ce_2O_3 unit cell with space group $P\bar{3}m1$. Then the models were relaxed by minimizing the energy of the system and calculating the self-consistent field (SCF), which was the last step before calculating the XAS spectra. The Perdew-Burke-Ernzerhof (PBE) of the generalized gradient approximation was used as the exchange and interaction potentials. The Van der Waals (vdW) correction is used to describe the long-range vdW interactions, and the dipole-dipole interaction is used in the case of an asymmetric species arrangement. The cut-off energy of the electronic wave function was 500 eV, and the k-space integration is performed according to the Monkhorst-Park scheme fitted to the reciprocal space size of the crystal structure of the models. The geometry optimization of the model is terminated when the force on each ion is not stronger than 0.05 eV. The pseudopotentials Ce.pbe-mt_fhi.UPF, O.pbe-mt_fhi.UPF, C.pbe-mt_fhi.UPF, and H.pbe-mt_fhi.UPF from official website of quantum espresso were used (Quantum ESPRESSO 2022; Giannozzi et al., 2009; Giannozzi et al., 2017).

In addition, jfeff10 software (Rehr et al., 2010; Kas et al., 2021) was used to calculate the XAFS and XANES spectra of CeO_2 and Ce_2O_3 phases. The unit cells of the above phases which were relaxed using QE were used in jfeff10 for XAS calculations. For the calculation of Ce L3-edge, the parameters, RPATH: 5, SCF: 12, Exchange: Dirac-Hara+HL and FMS: 50 were used. These parameters were adjusted until the best correlation between the calculated and the measured spectra was achieved.

2.2.6. Electrochemistry

For measuring the catalytic activity of ethanol oxidation reaction, cyclic voltammetry was applied and three-electrode cell with a BIO-LOGIC SP-200 potentiostat were used. Cyclic voltammetry is one of the most common techniques for electrochemical analysis. In principle, linearly varying potential is applied to the working electrode, covered with a catalyst layer (WE) from *E1* value to *E2* value, then from *E2* to *E1*. The potential on the WE determines, what current is flowing between working electrode and counter electrode (CE) and that value is being constantly registered by the potentiostat. The resulting current-voltage cyclic curve is called the cyclic voltammogram (CV) or voltammetric curve, in which we can distinguish the forward and reverse sweep.

In this work, the catalyst ink was deposited on a cylindric glassy carbon electrode, diameter of 5 mm, which served as WE. Platinum spiral wire was used as CE and a 4 M KCl silver chloride electrode (Ag/AgCl) served as the reference electrode (RE), so the potentials were constantly measured between WE and RE. The CV were measured without ethanol, in 1 M NaOH deoxygenated solution (it was bubbled with Ar for 20 min *prior* to every measurement). Next, for the EOR experiment, 1 M NaOH with 0.5 M C_2H_5OH solution served as the

electrolyte. As a reference sample, pure Au nanoparticles supported on Vulcan carbon black were measured.

Typically, in Pt-based catalysts, hydrogen desorption and adsorption peaks can be identified on the CV curves in the range 0 – 0.3 V. By integrating the area of desorption peak, the electrochemical active surface area (ECSA) of the catalytic material can be calculated. According to the equation:

$$ECSA\ [cm^2] = \frac{Q_H[\mu C]}{210\ [\mu C \cdot cm^{-2}]} \tag{10}$$

where: Q_H is the hydrogen desorption charge calculated from the integral of hydrogen desorption peaks in CVs and 210 μC/cm^2 (for Au) is a constant representing the adsorption of hydrogen monolayer on the catalyst. The *ECSA* value can be used to calculate the specific surface area (SSA), which represents the mass of catalytically active material (here: Au) on the WE surface (m_{Au}):

$$SSA\left[\frac{cm^2}{mg_{Au}}\right] = \frac{ECSA_{Au}[cm^2]}{m_{Au}[mg]} \tag{11}$$

The EOR results were normalized by *ECSA* and mass of Au. Furthermore, the onset potentials were characterized, as the intersection of the tangent of the fast-rising curve of current density and the tangent of the baseline. It represents the potential at which an increase in current density occurs, indicating the onset of the ethanol oxidation reaction.

The CV curves in this work were measured from -0.9 V (E_1) to 1.6 V (E_2) with a scan rate 20 mV/s, usually for 5 cycles. The resulting data were processed and analyzed with EC-Lab software and OriginLab software.

2.2.7. Infrared reflection absorption spectroscopy (IRRAS)

For identifying the products of EOR, *in-situ* infrared reflection absorption spectroscopy (IRRAS) was utilized. It uses infrared incident light beam, which is reflected from the sample surface and collected by the detector. The intensity of the reflected beam is analyzed and hence the reflection absorption spectrum is calculated. The shape of spectrum is determined by the molecule's vibrations in the sample, especially on the water surface. By comparing the spectrum with globally available reference spectra, the presence and concentration of specific molecules in waters can be verified and thus, the composition of the liquid sample can be identified. For this work, IRRAS was used to perform the EOR *in-situ* and analyze in real time the evolution of oxidation products concentration. Nicolet iS50 FT-IR spectrometer equipped with an MCT detector cooled with liquid N_2, an ATR accessory with ZnSe crystal and an electrochemical cell (Thermo Fisher Scientific, MA, USA). The electrodes were prepared with the same procedure as for the 2.2.2.1 paragraph. The spectra were obtained from 64 scans with a spectral resolution of 2 cm^{-1}, covering the IR range from 1200 to 3000 cm^{-1}. Before the experiment, spectrometer was purged with Ar gas for 1 h. The measurements were done using

two different ways. First, spectra were collected in several potentials: -0.5 V, 0.1 V, 0.3 V, 0.5 V and 0.9 V to show, which kind of EOR product prevails at a given voltage. On the other hand, long-term experiments (3 h) was done to show evolution of absorbances of peaks corresponding to CO_2, CO, CH_3CHO and CH_3COOH to show the dynamic of EOR products. The analyzed peaks were located at: 2341 cm^{-1} (CO_2), 2090 cm^{-1} (CO), 1620 cm^{-1} (CH_3CHO) and 1415 cm^{-1} (CH_3COOH) (Kowal et al., 2009; Liu et al., 2010; Head et al., 2017).

2.2.8. Electrodeposition

The experiment described in the Appendix was about electrodeposition of the PtNi nanoparticles film.

For this experiment, typical 3-electrodes system (RE, CE and WE) was used. The applied potential was varying from -0.8 V to 0.8 V by cyclic voltammetry. As a precursor, water solution of nickel(III) nitrate hexahydrate, M = 290.81 g/mol and chloroplatinic acid hydrate, M = 2.43 g/ml were used. Glassy carbon WE was immersed in 15 ml of the precursor solution, along with CE and RE. SP-200 potentiostat from BioLogic was used to apply potential. the scanning rate dE/dt was changed between 70 and 100 mV/s and the process was stopped after n = 5, 7, 10 or 15 potential cycles. Two Pt:Ni molar ratios were tested 25:75 and 35:65, respectively. Further methods and details of liquid cell experiments are described in the Appendix.

3. Results and discussion

3.1. Microstructural characterization and Au decoration of Ce_xO_y NAs

The synthesized ceria nanoaggregates displayed uniform size and morphology, with a spherical shape and a diameter of approximately 50 nm. SEM imaging showed their tendency to form large aggregates, see Figure 7(a-c), but STEM imaging revealed that each nanosphere was actually an agglomeration of tiny ~2 nm nanoparticles, which are self-assembled into spheres, see Figure 7(f-h). Following, their average size is 152 nm in diameter, their size distribution is presented in Figure 7(d). Their crystalline phases were investigated by the selected area electron diffraction (SAED, see Figure 7(e), and identified as CeO_2 fluorite cubic structure (JSPDS 01-071-4807, space group *Fm*-3m) and Ce_2O_3 hexagonal phase (JCPDS 00-023-1048, space group *P-3m1*). For CeO_2 following planes were indexed: (111), (200), (220), (311), (400) and (311). For Ce_2O_3 phase the following planes were indexed: (100), (002), (011), (012).

After the decoration with pre-synthesized Au NPs, HAADF STEM imaging and EDS chemical analysis was conducted. STEM HAADF images clearly showed the distribution of gold NPs, which appeared as bright spots, due to the higher Z-number of gold, providing greater contrast compared to ceria and carbon, see Figure 7(i-k). The Au NPs have ca. 5 nm in diameter and are randomly distributed on the surface of the ceria particles, leading to the classification of this structure as Au-decorated or core-satellite rather than a core-shell. This irregular distribution is likely influenced by the crystalline structure of ceria, as it has been noted (Liu et al., 2005) that Au atoms preferentially bind to oxygen vacancies on the ceria surface, which provide additional electrons. It is also clearly visible that cerium nanoaggregates are oxidized, Figure 7(k). Verifying their exact oxidation state, however, required further analysis. Ceria has a unique ability to alternate between (III) and (IV) oxidation states via spontaneous oxidation and reduction reactions, which means that CeO_2 and Ce_2O_3 coexist in varying ratios within the ceria nanoaggregates.

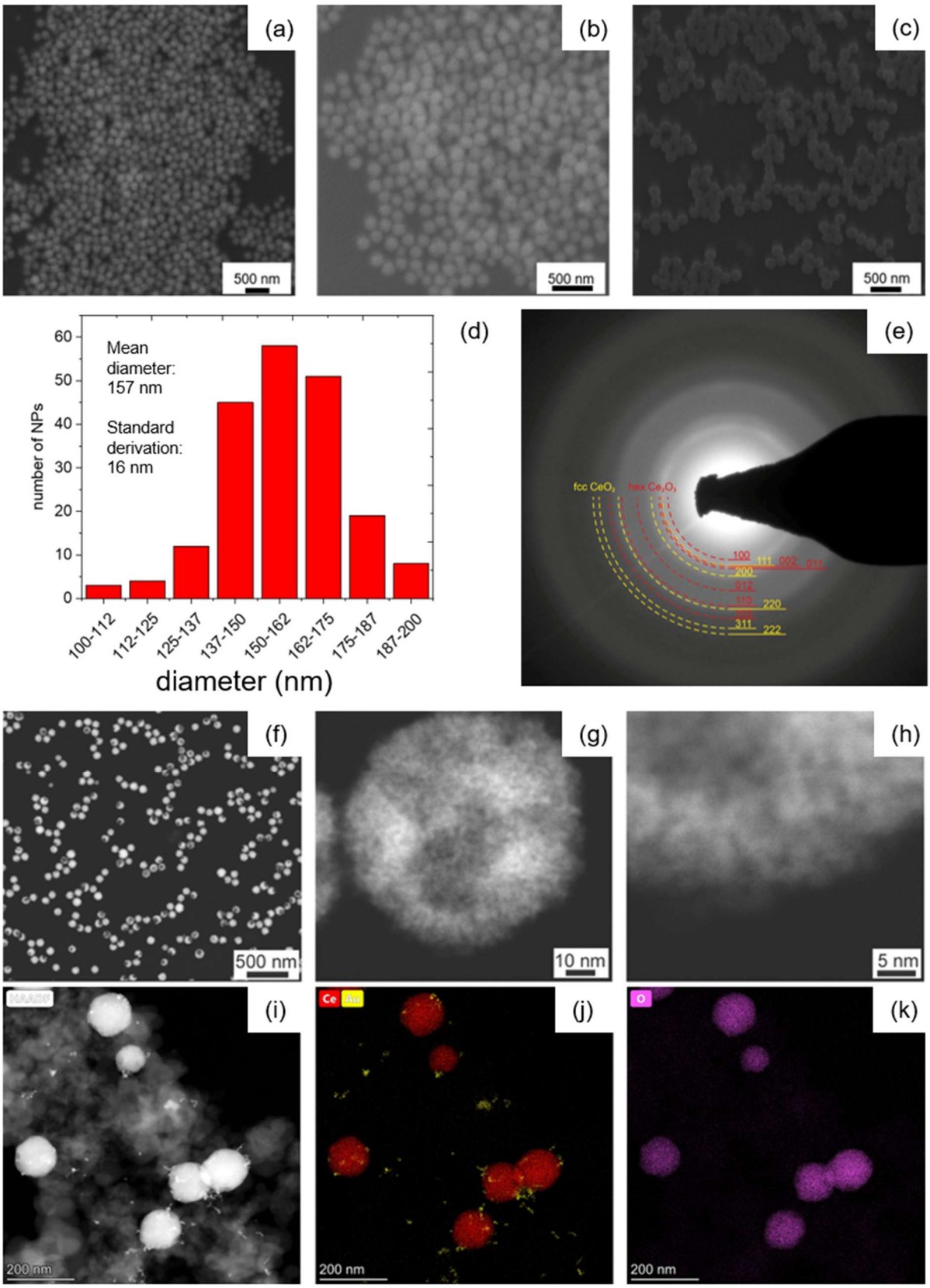

Figure 7 Ce_xO_y nanoaggregates synthesized ex-situ. (a-c) SEM images of the nanoaggregates; (d) Size distribution of the nanoaggregates, based on (c); (e) (SAED) pattern with indexed planes of CeO_2 and Ce_2O_3 phases; (f--h) STEM HAADF images; i) STEM HAADF image of ceria with Au supported on carbon black; j-k) EDS maps of ceria decorated with randomly distributed tiny Au NPs.

3.2. Catalytic activity of Au@Ce_xO_y/C system in EOR - cyclic voltammetry and IRRAS

This experiment was performed to measure the catalytic activity of the obtained ceria-based catalyst, but also, to investigate, if ceria nanoaggregates actually promote the activity of Au catalyst in EOR. The electrochemical analysis revealed high activity for the ceria-supported Au catalyst compared to pure Au nanoparticles on Vulcan carbon. This is confirmed by the voltammograms presented below. Figure 8(a) shows the scan for reaction in 0.1 M NaOH solution, while Figure 8(b) shows CV curves for reaction with 0.5 M ethanol, presenting the actual ethanol oxidation. Current density was noticeably higher for ceria-based catalyst in both cases, indicating higher catalytic activity. However, calculated ECSA parameters (see Table 1) show the opposite, since ECSA is higher for pure gold, which is an uncommon effect. The greater activity of the Au@Ce_xO_y/C catalyst could be connected to ceria's role as an oxygen provider and changes in electron distribution across the catalyst layer, which influenced current density and catalyst's resistance to poisoning effects (Silva et al., 2020). Additionally, small Au nanoparticles, despite high active area, may undergo aggregation and oxidation, limiting activity – an effect noted in several reports (Zheng et al., 2018).

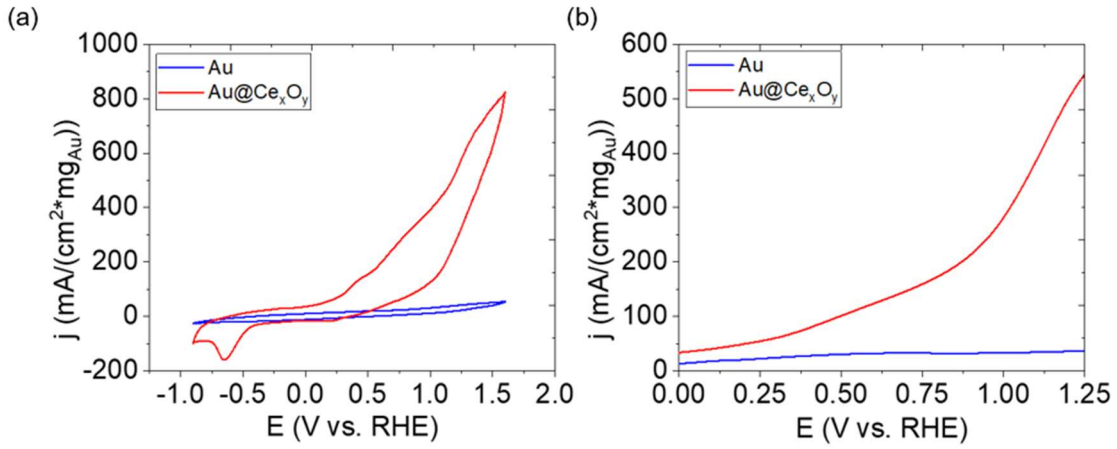

Figure 8 (a) CV curves for Au@Ce_xO_y/C and Au/C catalysts measured in 0.1 M NaOH; (b) EOR measured in 0.1M + 0.5M ethanol solution for Au@Ce_xO_y/C and Au/C catalysts.

Table 1 Calculated electrochemical parameters of the examined catalysts.

Parameter	Au@Ce_xO_y/C	Au/C
ECSA (cm^2/mg_{Au})	24.74	51.53
Onset potential (V)	0.03	0.30

In-situ infrared reflective absorption spectroscopy (*in-situ* IRRAS)

This technique allows to determine the selectivity of the analyzed catalysts for different ethanol oxidation reaction (EOR) byproducts. Characteristic absorbance peaks for CO_2, CO, CH_3CHO and CH_3COOH were identified and confirmed in the spectra presented in Figure 9. IRRAS spectra collected for $Au@Ce_xO_y/C$ showed, that at all potentials, the signal from CH_3CHO was almost stable, while for CH_3COOH, the signal increased with the increasing potential. Continuing, for the peak corresponding to CO, the absorption value was very small in all analyzed potentials, while the signal from CO_2 increased with increasing of potential values. Such analysis helps to determine the most effective potential for EOR. The intensity of the IRRAS signal determines the level of the product generation and depending on the generated product, different number of electrons is generated. For CH_3COOH or CH_3CHO it is only 4 or 2 electrons respectively, while for CO_2 it is 12 electrons. Therefore, from the application viewpoint, the most important and interesting is the CO_2 signal.

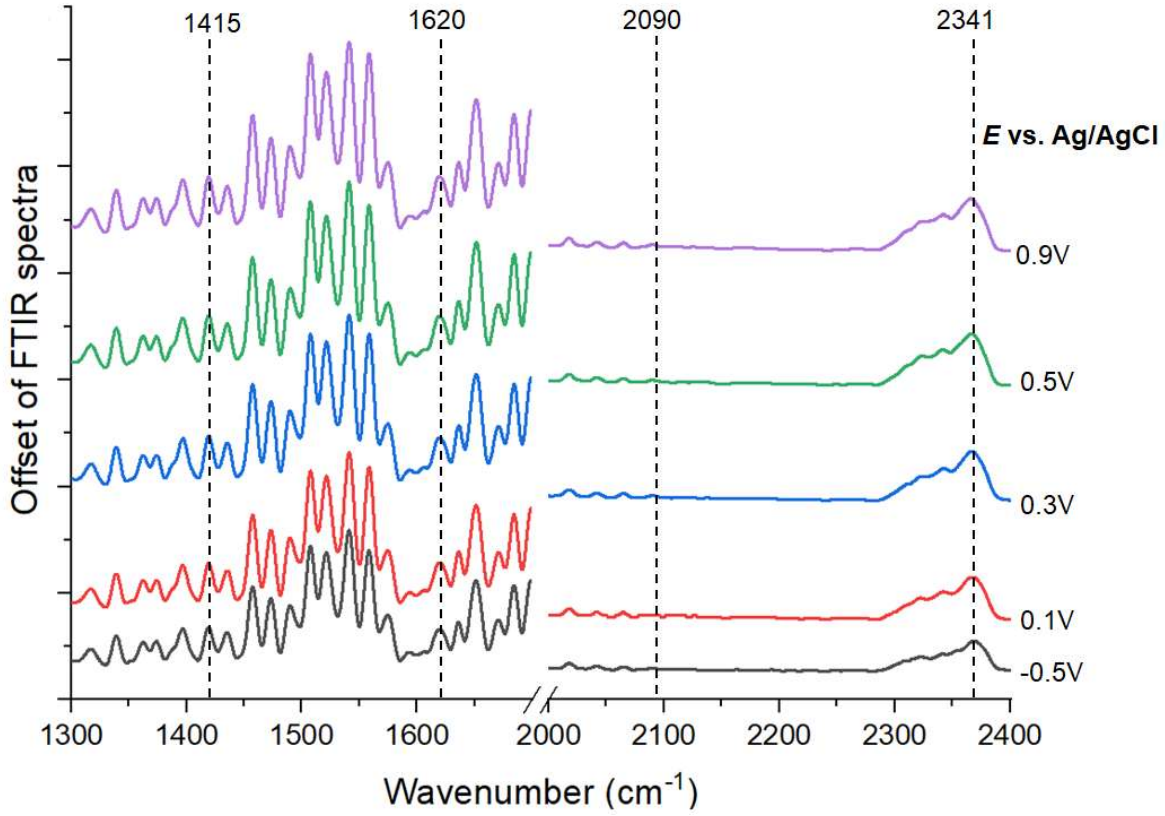

Figure 9 In-situ IRRAS spectra recorded during ethanol oxidation on $Au@Ce_xO_y/C$ catalysts in different potentials.

To evaluate the catalyst's long-term performance and changes in the concentration of EOR products, a continuous 3 h measurement was performed and the evolution of absorbance peaks was tracked, see Figure 10. In the case of CH_3COO and CH_3CO it was visible, that the values of their respective absorbance peaks were similar to each other during the entire experiment.

Moreover, it was noticed, that during the first 2h, the values of the absorbances of these two products were stable, and started to increase after 2h. In the case of the signal originating from CO vibrations, the absorbance was the smallest in comparison with CH_3COO, CH_3CO and CO_2 and it was stable during the entire experiment. Importantly, for the CO_2 EOR product, the value of absorbance increased after each 30 minutes, it was constantly increasing and was the highest in comparison with other examined EOR products during the entire measurement.

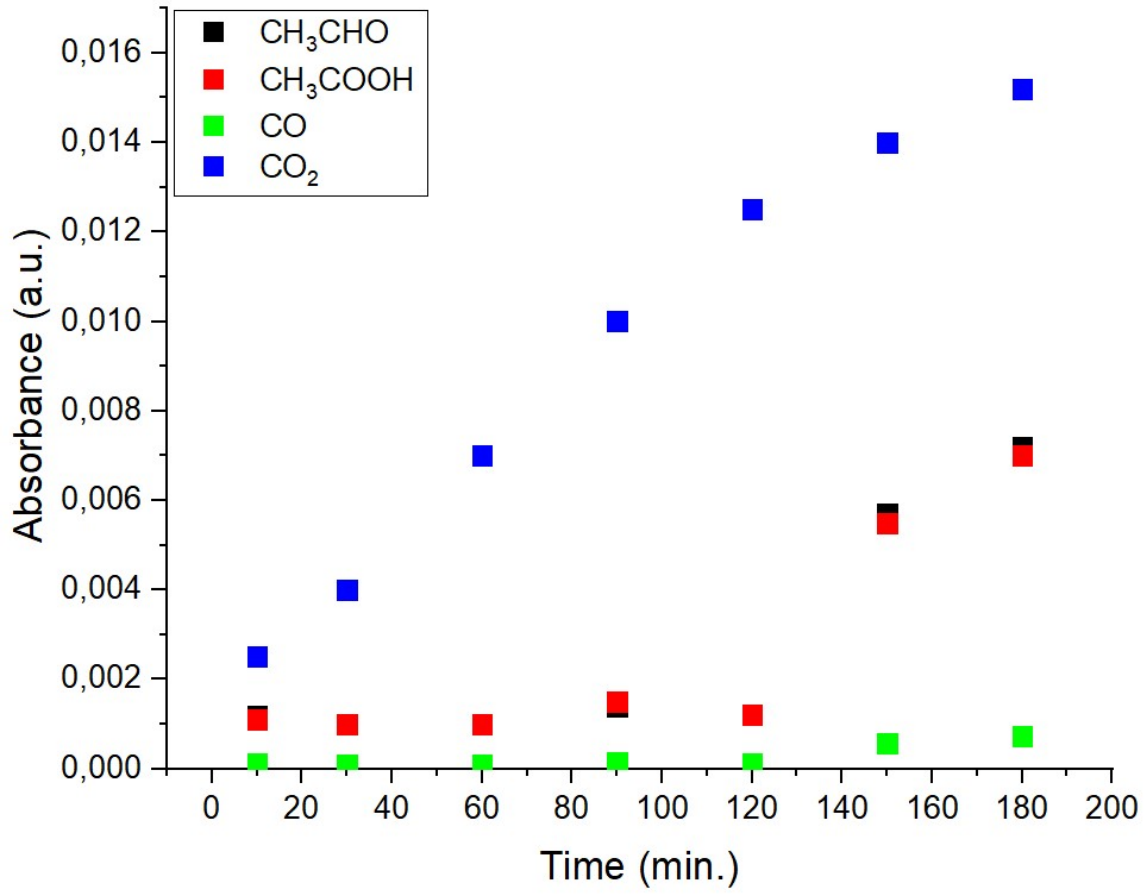

Figure 10 Kinetics of ethanol oxidation products generation observed during 3 h of EOR, showing increasing absorbance peaks in time, indicating that Au@Ce_xO_y/C breaks down the ethanol molecules successfully, producing high amount of CO_2.

These findings indicate that Au NPs supported on ceria NPs form a robust and highly efficient catalyst, characterized by a strong selectivity towards full oxidation of ethanol and CO_2 formation. This selectivity maximizes the energy output, providing the highest number of electrons in the EOR reaction, affirming the high efficiency, durability and effectiveness of the synthesized catalyst.

3.3. Evolution of the oxidation state of Ce_xO_y NAs supports resulting from EOR – XANES study – DFT modelling experiment

Using DFT methods separate XANES spectra for Ce_2O_3 and CeO_2 crystalline phases were calculated, see Figure 11. Those are pure ceria(III) and ceria(IV) oxides, which existence in nature is highly unlikely. The characteristic peaks for both phases are labelled in Figure 11.

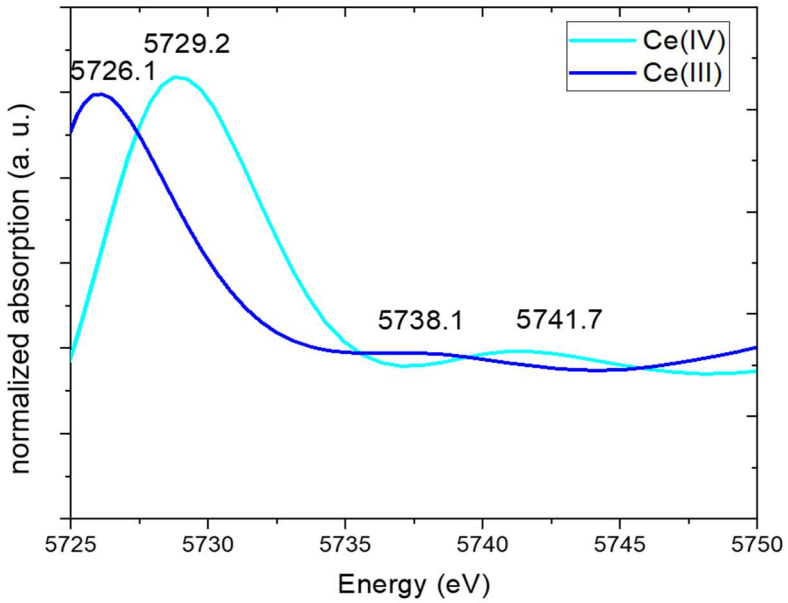

Figure 11 Simulated XANES spectra for Ce(III) phase and Ce(IV) phase.

It is worth noting, that there are two sets of characteristic peaks, and in both sets, peaks from two different phases are very close to each other. At the same time, the peak for ceria(III) is always located at lower energy than the one for ceria(IV). Therefore, in the XANES curve of actual ceria sample, in which Ce_2O_3 and CeO_2 coexist, peaks from these two phases may appear as one merged peak. The maximum value of the resulting peak is expected to be shifted towards lower or higher energy, depending on the ratio between ceria(III) and ceria(IV) in the mixture.

Evolution of the oxidation state of Ce_xO_y NAs

Taking into account, that ceria exists as a mixture of Ce_2O_3 and CeO_2 (see Chapter 1.1.5), XAS measurements were conducted at SOLARIS to determine the ratio of these phases in the synthesized material, using commercial CeO_2 powder as a reference. The XANES spectra of the reference sample and as-synthesized ceria nanoaggregates are provided below in Figure 12. The calculated peak positions from the simulated XANES spectra can be compared with local maxima positions from the measurement. Thus, first local maximum in commercial ceria is positioned at 5731.1 eV, which should resemble to the first set of peaks from Figure 11. In the synthesized ceria, however, this first maximum is positioned at 5726.9 eV. So for the commercial CeO_2 this peak is shifted towards higher energies, suggesting high concentration

of ceria(IV), but with some amount of ceria(III) as well. While in the studied sample, the local maximum is closer to the 5726.1 peak, suggesting something opposite. Similarly, the second local maximum was located at 5737.9 eV for commercial CeO_2 and 5737.5 eV for the experimental sample, confirming the same effect. As mentioned before, characteristic peaks are merged and appear as one with shifted positions.

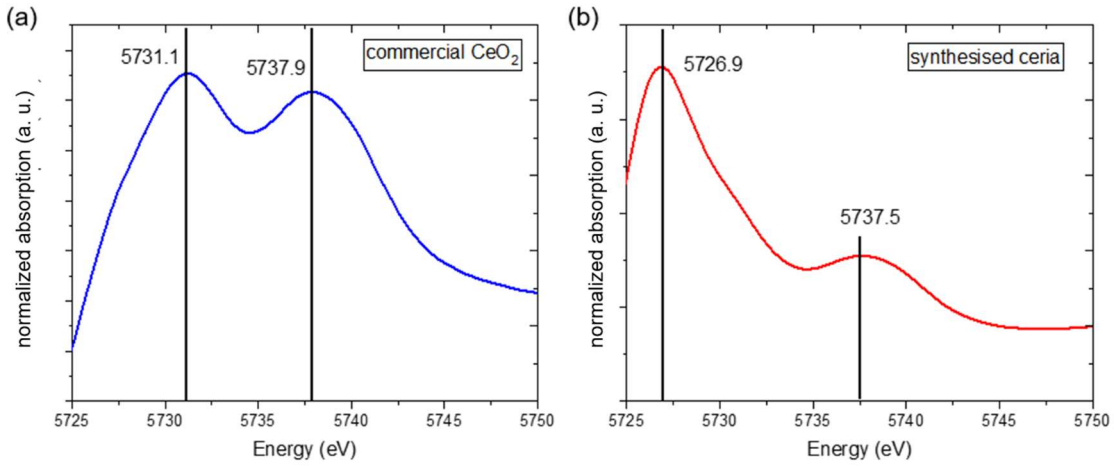

Figure 12 XANES spectra for commercial and synthesized ceria samples.

For a deeper investigation of the XANES spectra and quantifying the ratio between Ce(III) and Ce(IV), further analysis of peaks features was needed. Following the procedure reported by the teams of Bianconi and Phokha (Bianconi et al., 1987; Phokha et al., 2012; Phokha et al., 2015), the curve-fitting with an arctangent function for edge jumps and Gaussian functions for peak features was used. The energy threshold (E_0) was defined as the global maximum of the first derivative of the main absorption edge, while the center of the arctangent function was calculated based on the inflection point of the main edge. Following Phokha and co-workers, 4 characteristic peaks and their charge transitions were identified and labelled: 5737.9 eV (indexed as A) and 5731.3 eV (indexed as B) represented the Ce(IV) oxidation state (transitions $2p \rightarrow 4f^0 5d$ and $2p \rightarrow 4f^1 5d_t gL$, respectively), while the peak at 5726.8 eV (indexed as C) corresponded to Ce(III) (transition $2p \rightarrow 4f^1 5d_e gL$) (Phokha et al., 2012; Wu et al., 2016), see Figure 13. The second peak for Ce(III), which was visible in the DFT simulation was not considered in the cited works, therefore it was also not taken into account for this calculation. A pre-edge feature (peak D) was attributed to the $2p_{3/2} \rightarrow 4f$ transition due to 5d-4f hybridization, allowed by selection rules (Munoz, 2015).

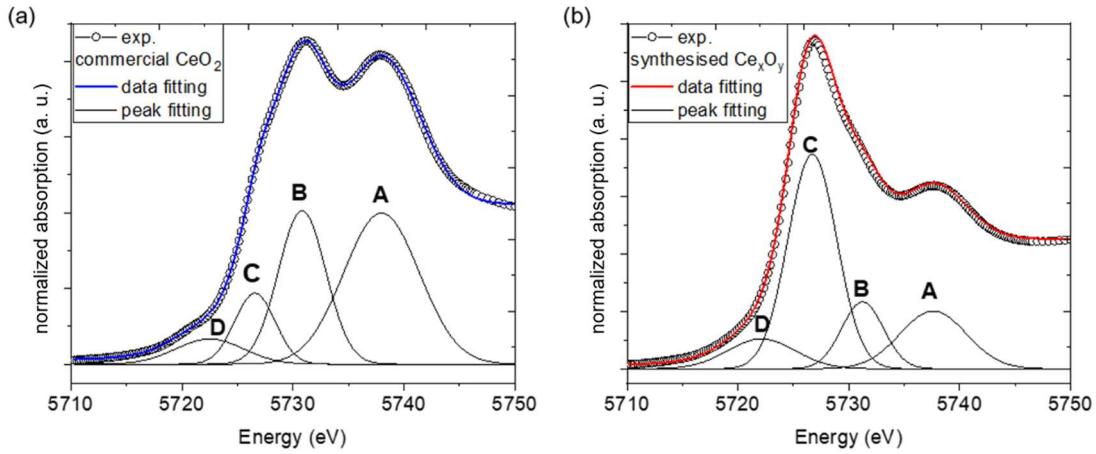

Figure 13 XANES results for (a) commercial cerium(IV) oxide and (b) synthesized ceria.

For quantification, the Ce^{3+} content was calculated using the areas under peaks A (5737.9 eV), B (5731.3 eV), and C (5726.8 eV) as follows:

$$[Ce^{3+}] = \frac{S(C)}{S(A)+S(B)+S(C)} \cdot 100\% \tag{12}$$

where *S(A)*, *S(B)*, and *S(C)* are the areas of the respective peaks. The results showed 61% Ce^{3+} and 39% Ce^{4+} in the synthesized Ce_xO_y NAs, compared to 13% Ce^{3+} and 87% Ce^{4+} in commercial CeO_2 powder, confirming ceria's ability to vary its oxidation state. The calculated values are presented below in Table 2.

Table 2 Calculation of the Ce(III) percentage in ceria samples.

Peak index	Commercial CeO_2		Synthesized Ce_xO_y	
	Peak area	Ce(III) [%]	Peak area	Ce(III) [%]
A	4.356	13.2	2.194	61.3
B	6.818		3.005	
C	1.706		8.230	

Ce^{4+}/Ce^{3+} ratio evolution has been extensively studied due to their role in catalytic reactions, including oxygen vacancies on ceria's surface, which improve catalytic performance when ceria supports noble metals like Pt (Bunluesin et al., 1997; Swartz et al., 2001). Further research has shown that Au atoms on ceria surfaces encourage oxygen vacancy formation, thus enhancing ceria's reducibility and catalytic activity, an effect observed with ceria modified with Zr (Yang et al., 2006).

With this knowledge, two more samples were examined with XANES: ceria NAs after the decoration with gold NPs and the catalyst ink after the EOR. The analysis of recorded spectra was made with the same procedure as before, with identifying the A, B, C and D peaks and calculating their area for Ce^{3+} quantification. The obtained spectra are presented in Figure 14. The results show, that its concentration was lower after decoration – 38% – and the lowest after

EOR – 16%, see Table 3. Those results seem to be against intuition, it could be expected that ceria will be more reduced after the reactions, because Au atoms induce it to release more oxygen. Here an opposite effect was observed, which only shows how strong is the redox mechanism in cerium oxide NAs. The atoms immediately utilize oxygen from environment to re-oxidize.

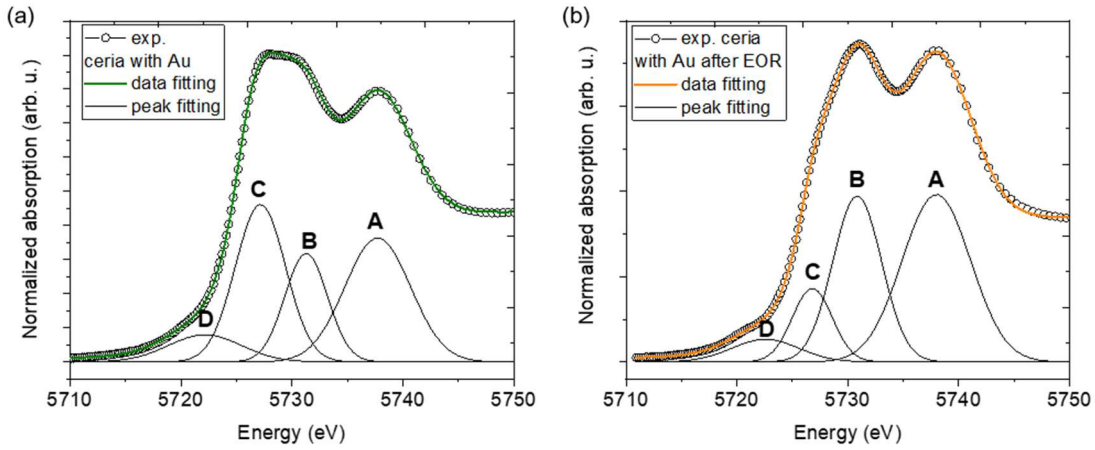

Figure 14 XANES results for A) Au@Ce_xO_y/C catalyst and B) Au@Ce_xO_y/C calyst after EOR.

Table 3 Calculation of Ce(III) percentage in ceria samples with Au NPs.

Peak index	Au@Ce_xO_y/C		Au@Ce_xO_y/C after EOR	
	Peak area	Ce(III) [%]	Peak area	Ce(III) [%]
A	3.065	38.3	5.439	16.4
B	5.398		7.715	
C	5.244		2.588	

3.4. STXM study of the oxidation state of individual Ce_xO_y NAs supports resulting from EOR

XANES measurements provided a global view of ceria's oxidation state, but STXM imaging allowed us to explore the phase distribution at nanoscale in the sample. With STXM imaging it was possible to examine, if different nanoaggregates have different oxidation states, or if both phases are present in one nanoaggregate. Characteristic peaks were identified in the spectra, including Ce^{3+} multiplets at 880.5 eV, 882.7 eV, 895.5 eV and 897.5 eV, and Ce^{4+} multiplets at 889 eV, 902.5 eV, and 906 eV. Again, 3 samples were measured: as-synthesized ceria (see Figure 15), ceria decorated with Au (see Figure 16) and catalyst after EOR (see Figure 17). All of them were compared, confirming that Ce^{3+} and Ce^{4+} coexist in a single nanoaggregate.

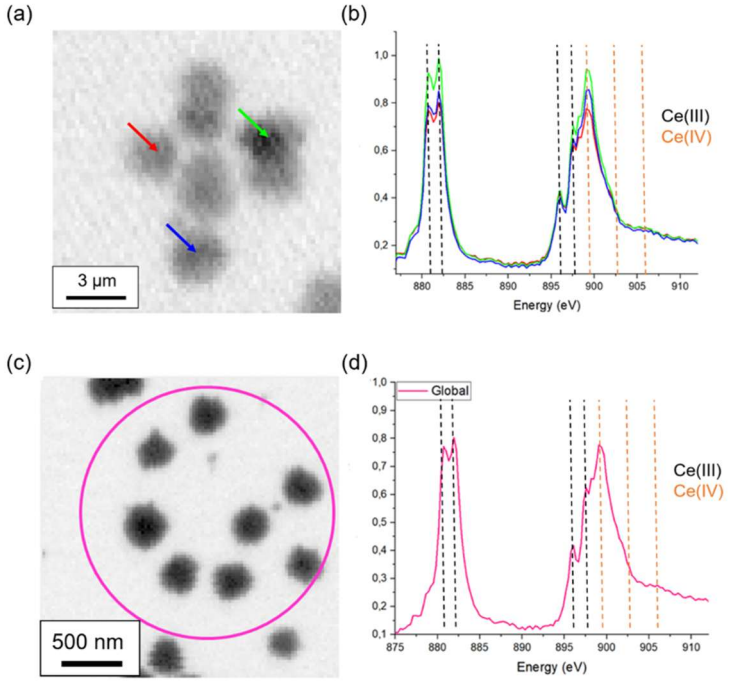

Figure 15 STXM images and XAS spectra for synthesized ceria NAs.

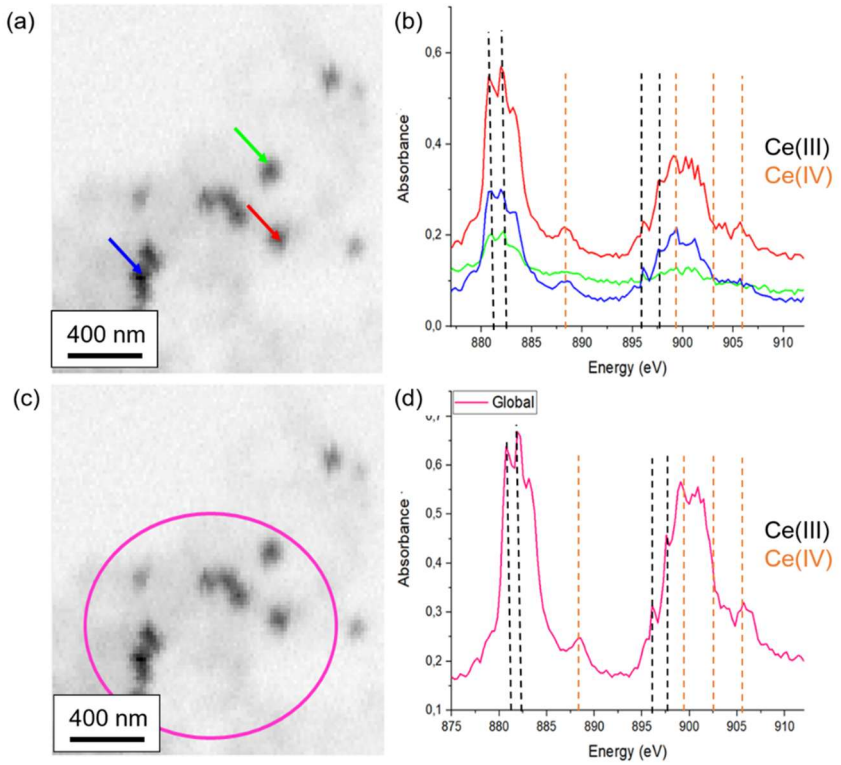

Figure 16 STXM images and XAS spectra for synthesized ceria NAs decorated with Au NPs.

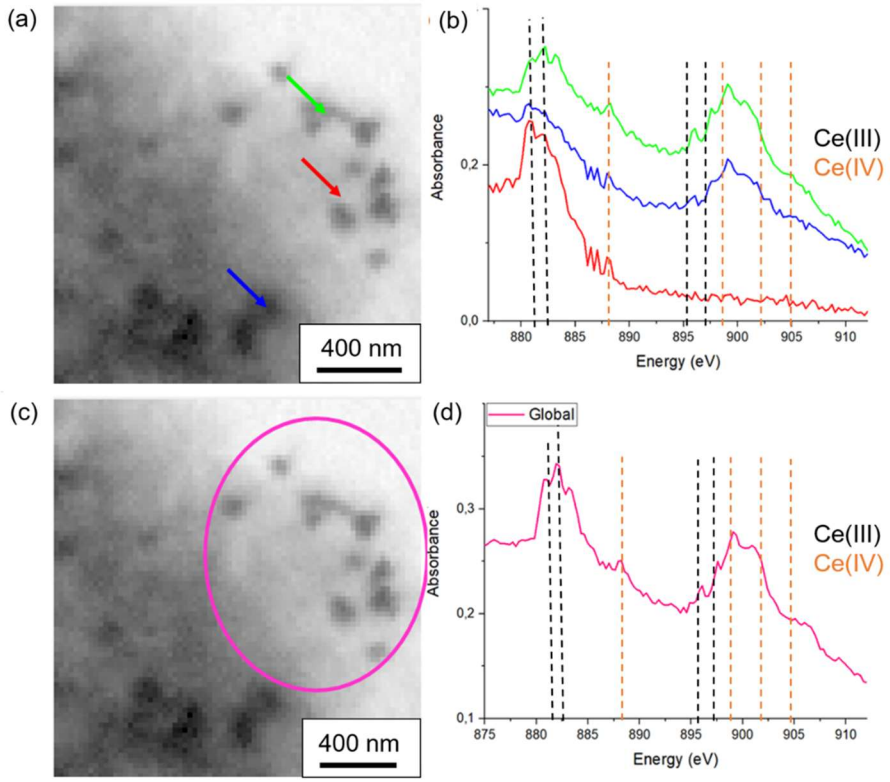

Figure 17 STXM images and XAS spectra for ceria-based catalyst after EOR.

These findings demonstrated that both Ce^{3+} and Ce^{4+} phases coexist within individual nanoaggregates, with a consistent Ce^{3+}/Ce^{4+} ratio across all particles analyzed, proving the uniformity of the synthesized nanoaggregates.

3.5. Liquid cell TEM experiments on ceria nanoaggregates

3.5.1. Synthesis of ceria nanoaggregates from liquid $Ce(NO_3)_2$ precursor

In-situ synthesis of ceria nanoaggregates

Although ceria synthesis typically requires specific temperature and pressure (in this case performed in a closed reactor), it has been explored in this work, if the electron beam alone could generate enough reducing agents to enable crystallization. For this experiment, only a water-based ceria precursor solution was pumped through the liquid cell. Under *ex-situ* conditions, ethylene glycol serves as the reducing agent, so in a water solution at room temperature, nucleation would normally not occur.

After 3 seconds of pumping and imaging, larger nanoaggregates became noticeable, and after 10 seconds, they formed a dense, interconnected structure growing on the silicon nitride window. The entire process was recorded and the time frames are presented in Figure 18(a). It is seen in the *post-mortem* imaging (Figure 18(b-e)), that this sponge-like vast agglomerate is actually composed of numerous tiny ~2 nm sized spheres, similarly like the nanoaggregates synthesized *ex-situ*.

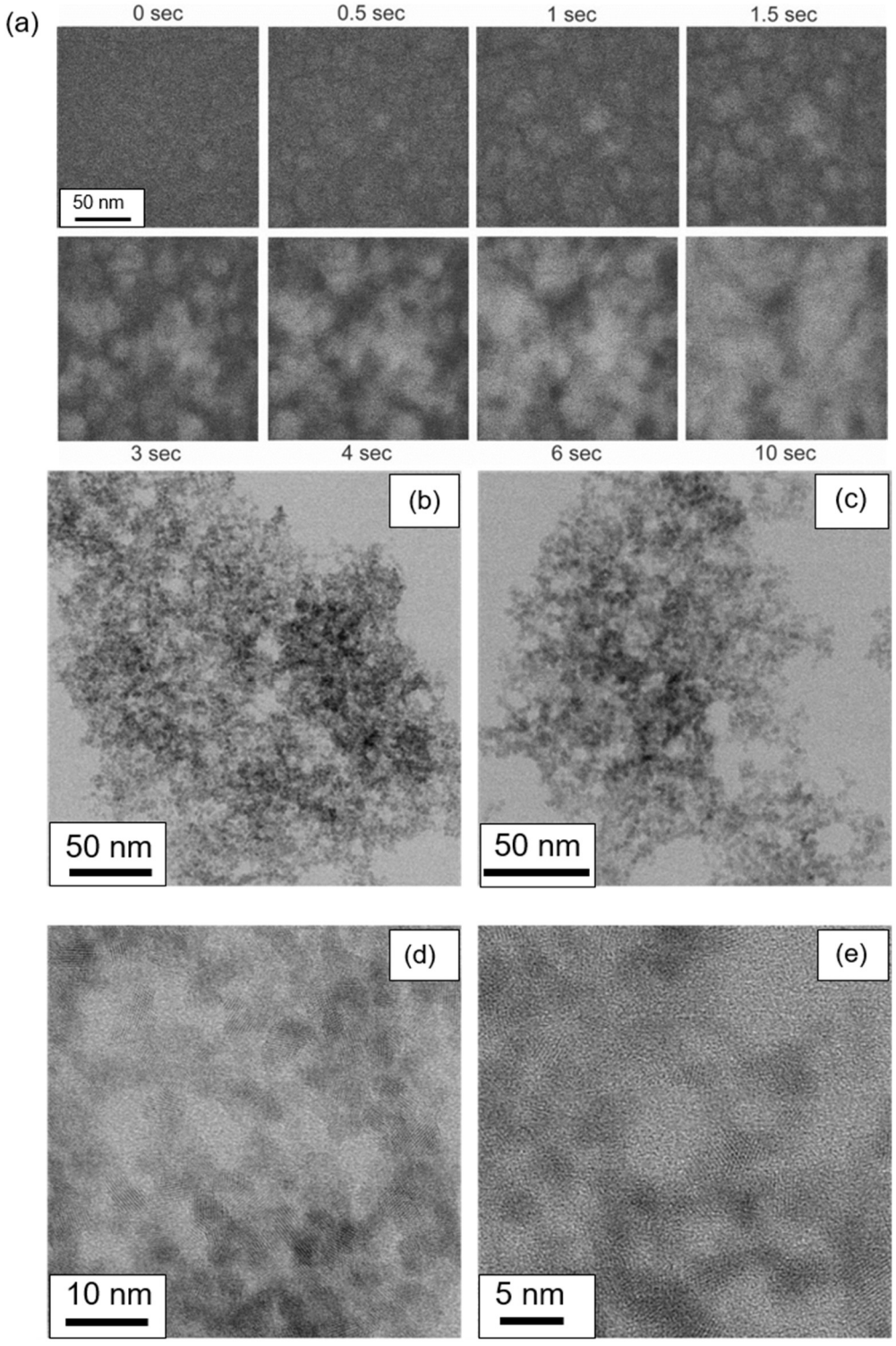

Figure 18 (a) Time frames from the electron beam induced synthesis of ceria NAs in LC-TEM, extracted from Movie 1; (b-e) Post-mortem imaging of the ceria NAs synthesized in LC-TEM.

In general, nanoaggregates synthesized in liquid, tend to migrate towards one of the windows. Researchers have examined various forces that might influence nanoparticle migration in an electrolyte, drawing them toward the window. Even outside the LC-TEM

context, migration may be affected by different mechanisms. Suzuki et al. (2011) highlighted five possible factors: (1) interactions between nanoparticles, (2) interactions between nanoparticles and the surface, (3) interactions between nanoparticles and the liquid, (4) interactions between the liquid and the surface, and (5) electrostatic interactions among ions in the liquid. Their findings suggest that electrostatic interactions, particularly from (4) and (5), are likely the most influential, although local liquid viscosity near the surface also plays a crucial role. According to their model, a surface charge distribution increases local viscosity, limiting nanoparticle diffusion near the surface, decreasing their migration, and leading to immobilization via electrostatic interactions. In the LC-TEM experiment, additional complexities arise from the electron beam's influence. The electron beam and resulting secondary electron formation can charge nanoparticles, causing repulsion from the beam. Additionally, the beam may raise the liquid temperature, creating thermal motion in the liquid and nanoparticles. The beam may also form water vapor bubbles within the liquid cell, which expand and potentially push the nanoparticles outwards (Ring and de Jonge, 2012). However, nanoparticle migration towards the silicon nitride window is also frequently observed in LC-TEM. Consistent with Suzuki et al., local viscosity, electrostatic interactions and van der Waals forces likely contribute to this effect (Ring and de Jonge, 2012). Later studies have corroborated these mechanisms, observing nanoparticle attachment to the silicon nitride window and attributing this behavior to a confinement effect from local viscosity, which enhances adhesion between the nanoparticles and the window (Woehl et al., 2014; He et al., 2020).

Post-mortem SEM and TEM imaging of the top chip showed large clusters formed from smaller spherical nanoparticles. Surprisingly, no such structures appeared on the bottom chip. TEM imaging of the bottom chip revealed significantly smaller nanoparticles, approximately 2 nm in size, which were more dispersed and less aggregated than those on the top chip. This unexpected finding suggests that the electron beam does not scatter uniformly inside the liquid cell. Instead, scattering occurs with a significant intensity reduction, as the beam travels through the liquid layer. In the 150 nm thick cell, electron distribution and energy vary between the top and bottom of the liquid layer. Consequently, while the beam's energy was sufficient to promote large clusters growth on the top, it only supported the nucleation of smaller particles at the bottom. Recent studies, such as Korpanty et al. (2022), have simulated this scattering effect to model energy dispersion in liquids accurately. Their work indicates that in water, the concentration of radical species like H_2O_2 and H_2 increases significantly over time during scanning, while e_h^- concentrations rise rapidly at first, but then decrease after several microseconds. This trend generally aligns with previous models (Schneider et al., 2014). However, Korpanty et al. further detailed that electrons lose energy as they pass through the liquid, owing to scattering, interactions, and radical generation. The spatial distribution of electron/liquid interactions inside liquid-cell TEM (LC-TEM) was also modelled and examined by the Browning and Mehdi's team (Lee et al., 2022). Their findings indicate that interactions are most intense in the beam-exposed zone, generating high concentrations of radical species around this zone, thereby creating a concentration gradient across the liquid layer that drives radical diffusion. Due to beam energy loss, the distribution of generated species is not homogeneous, forming a distinctive profile. They further suggested that radicals from the initial beam position may influence subsequent radiolytic effects in newly illuminated areas.

Thus, factors like beam size, illumination duration, dose rate, distance between illuminated pixels, beam movement rate and radical diffusion rate collectively impact the overall distribution of radicals in the liquid. During prolonged illumination, energy loss and decreasing concentrations should become apparent. The observed distribution of ceria nanoaggregates can likely be explained by this localized energy pattern: high-energy radicals are concentrated at the top, promoting dense cluster growth, while dispersed, lower-energy radicals at the bottom enable smaller and more widely distributed nanoparticle nucleation.

Interestingly, once the ceria NAs formed, they began to degrade rapidly. After 15 seconds of continuous illumination, the structures started to dissolve, disappearing completely in less than a minute, even though the precursor solution remained within the cell, see Figure 19(a). Notably, the dissolved region did not regenerate afterwards, and the damaged area was visible in *post-mortem* imaging, as it can be seen in Figure 19(b).

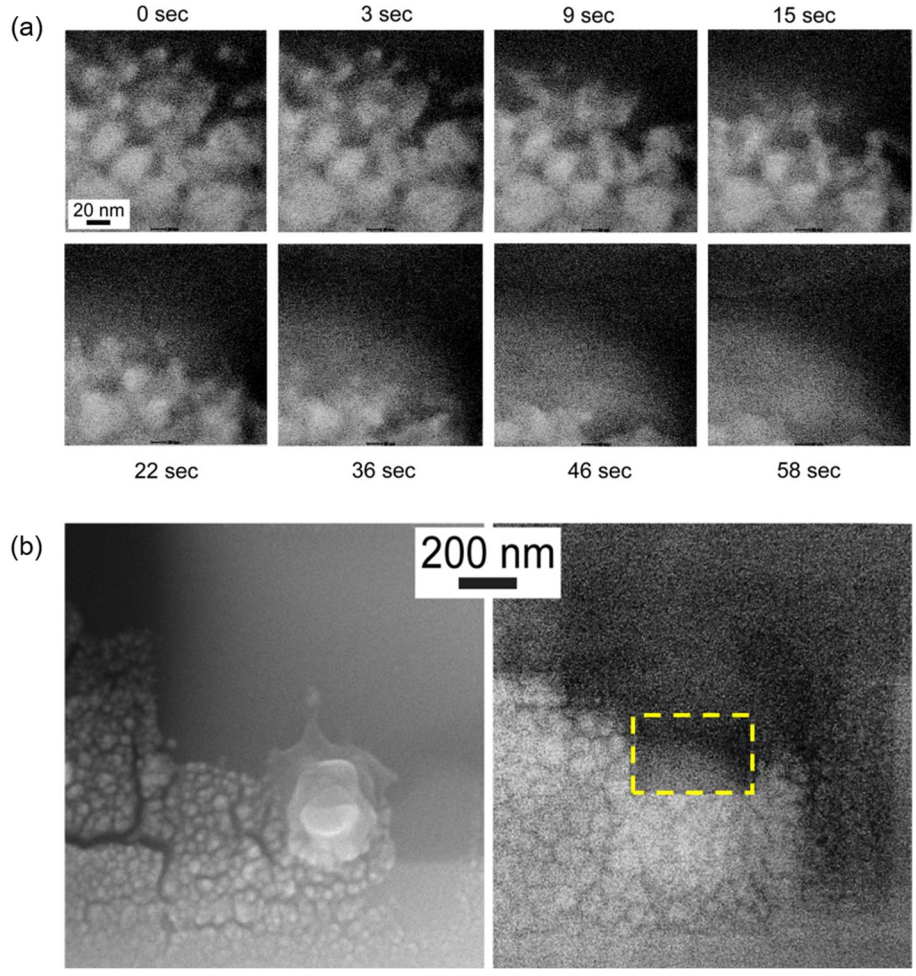

Figure 19 (a) HAADF STEM images of radiolytic dissolution process observed by LC-TEM of ceria NAs synthesized in LC-TEM. Extracted from Movie 2; (b) SEM images of bottom E-chip with the region observed during LC-TEM radiolitic dissolution experiment (yellow square).

Similar dissolution effects have been previously reported for other nanostructures, with one suggested cause being water radiolysis and pH fluctuations. The electron beam induces water radiolysis, producing various reactive species such as H_3O^+ ions (also acting as H^+), OH^-, H_2,

and hydrated electrons (e^-). Some of these species serve as reducing agents that drive nucleation and growth, while others act as oxidizing agents, promoting dissolution. Predicting whether oxidation or reduction will dominate in an LC-TEM experiment is challenging.

As it was discussed before, the fundamental study on water-electron interactions in LC-TEM by Schneider et al. (2014), suggests that the pH of water solutions becomes more acidic inside LC-TEM. This effect is significant, as pH is an important factor for ceria solubility. Studies show that CeO_2 NPs undergo reductive dissolution in acidic environments, as described by Plakhova et al. (2016):

$$CeO_2 + e^- + 4H^+ \leftrightarrows Ce^{3+} + 2H_2O \quad (13)$$

Other studies have also confirmed ceria's high solubility in acidic environments (Dahle et al., 2015; Asghar et al., 2017). While the electron beam continuously supplies electrons, it also generates H^+ ions, which, unlike electrons, diffuse extensively through the liquid, affecting pH over a larger area than the irradiated region. Initially, ions reduce and crystallization occurs, but as H^+ concentration increases and pH drops, NPs begin to dissolve, releasing Ce^{3+} ions and degrading the structure. Ce^{3+} remains stable in acidic pH, persisting in this form (Plakhova et al., 2016).

However, Abellan et al. (2017) proposed a different model. They acknowledge that pH decreases within the LC for pure water, but for their own simulation they used a solution containing cerium. And for this case, they reported that the effect is reversed. Their findings suggest that Ce^{4+} species undergo reduction first, as this is thermodynamically favorable, forming Ce^{3+} initially and eventually metallic Ce. They support their model by an experiment, in which they obtained $Ce(OH)_3$ structures in the LC-TEM, which thermodynamically should be stable only in alkaline media. From the Pourbaix diagram (Yu et al., 2006), metallic cerium is highly soluble in water, which leads to the re-formation of Ce^{3+} in a cyclic reaction, generating OH^- ions according to the following reaction:

$$Ce^{4+} + e^-_{aq} \leftrightarrows Ce^{3+} \quad (14)$$

$$Ce^{3+} + 3e^-_{aq} \leftrightarrows Ce^0 \quad (15)$$

$$Ce^0 + 3H_2O \longrightarrow Ce^{3+} + 3OH^- + \frac{3}{2}H_2 \quad (16)$$

As a result of this cyclic reaction, Abellan et al. suggest it would be expected to see not a decrease but an increase in pH due to the local production of OH^- species. According to their model, pH could shift from acidic towards neutral or even slightly alkaline levels. The evolution of pH is a critical parameter in LC-TEM, though it is challenging to control or analyze. Conflicting reports describe notable pH fluctuations, with disagreement on whether H^+ or OH^- predominates, leaving the issue unresolved. A recent study by Fritsch et al. (2023) emphasizes the complexity of this issue, noting that while studies support both trends, some overlooked factors may be at play. Fritsch and colleagues argue that focusing solely on H^+ or OH^- separately is insufficient; instead, they propose a comprehensive approach tracking the evolution of both

ions simultaneously to fully understand pH dynamics within the liquid cell. Their study describes 17 different species interconnected across 83 reactions that can be generated in water under electron beam irradiation, leading to a new model of pH dynamics in irradiated water. Surprisingly, they found that even supposedly inert ions, such as chloride, bromide and nitrate, might affect pH in electron-irradiated solutions.

In summary, determining the resulting pH within the liquid cell remains challenging. While Fritsch et al.'s model offers intriguing insights, they acknowledge that experimental work is needed to validate their hypotheses through specific marker reactions.

Asghar et al. (2017) further investigated factors affecting ceria NAs dissolution, performing series of experiments using LC-TEM. They used deliberately high-intensity electron-beam irradiation of nanoaggregates suspensions and recorded their evolution with nanometer resolution, to quantify their exact dissolution rates. Furthermore, they investigated several hypotheses to explain the surprisingly high dissolution rate of ceria. They concluded that this rate was not regulated by a single parameter, but rather by a synergistic combination, including nanoparticle size, solution pH, concentrations of radiolytic water products, particle microstructure, dynamic shifts in ceria surface oxidation states, electron dose rate and others.

In-situ synthesis of ceria nanoparticles on *ex-situ* synthesized ceria NAs

To analyze further the beam effects, an additional experiment in the liquid cell was conducted. Pre-synthesized ceria NAs were applied onto the chip, and the cell was filled with the ceria precursor solution. The goal was to induce new ceria synthesis and then assess, whether both freshly formed and pre-synthesized NAs would dissolve under radiolysis. Results showed that fresh ceria synthesis did occur, although at a slower rate, with initial nucleation observed after 4 seconds of illumination. Time-lapse imaging revealed fresh nanoparticles growing between and on top of the deposited spheres, forming a dense, sponge-like structure, similarly like in the previous LC-TEM experiment. After 100 seconds, this structure continued to grow – see the time frames in Figure 20(a). Observations in a separate region at lower magnification revealed a different outcome. This time, fresh ceria did not grow continuously; instead, after some initial nucleation, dissolution of the deposited ceria spheres began after around 9 seconds, and within 40 seconds, the entire illuminated area was cleared, as it is presented in Figure 20(b). This discrepancy appears to stem from the electron dose rate.

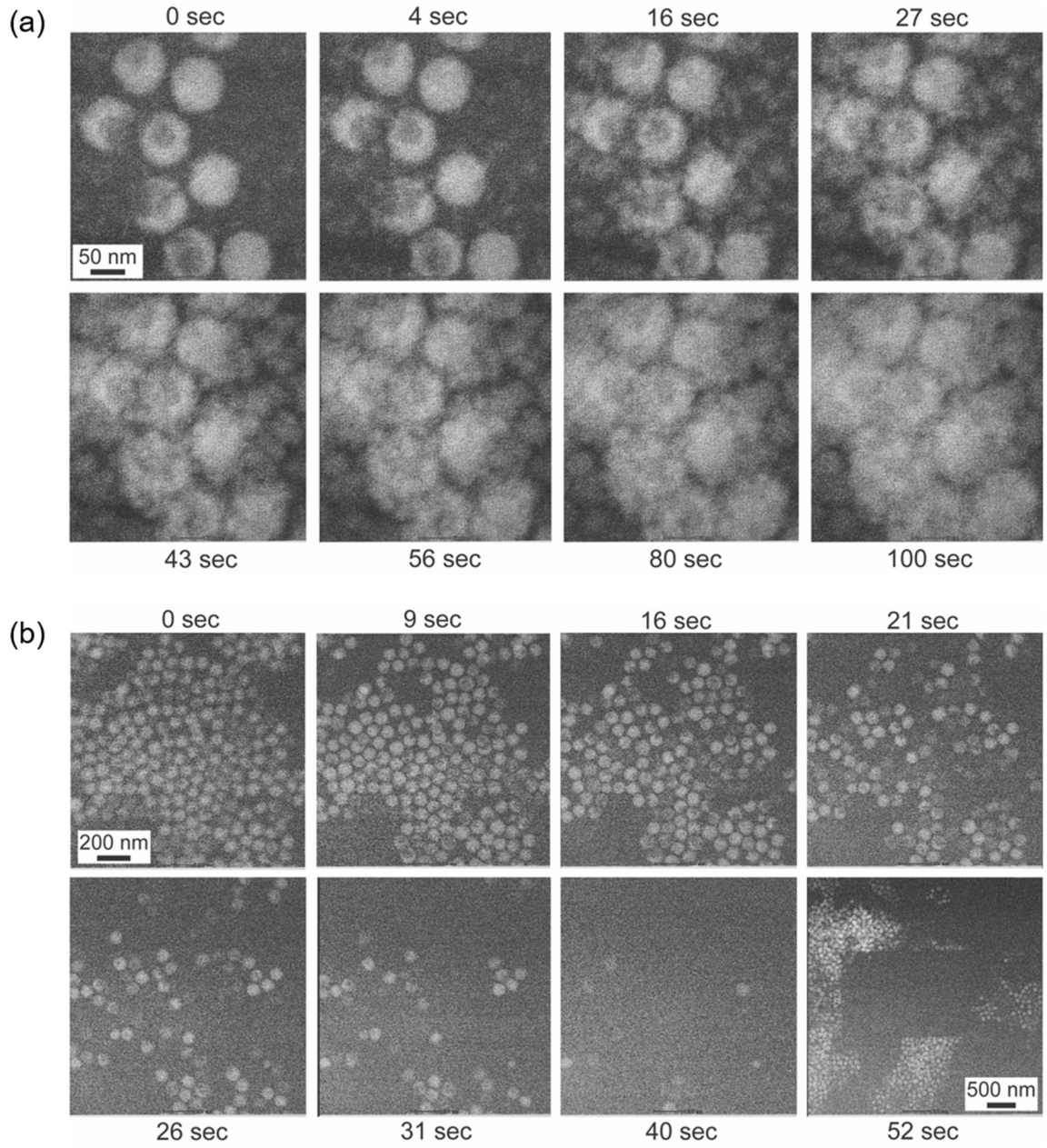

Figure 20 (a) STEM HAADF time frames from the in-situ *Movie 3 in the LC of formation of ceria NAs on Ce_xO_y NAs from $Ce(NO_3)_3{\cdot}6H_2O$ water solution; (b) STEM-HAADF time frames from the Movie 4 in the LC of dissolution of the laboratory synthesized Ce_xO_y NAs under the beam. The liquid cell is flushed with $Ce(NO_3)_3{\cdot}6H_2O$ water solution.*

When focusing the electron beam on the pre-synthesized ceria NAs at high magnification, the electron dose rate was high, tipping the balance toward synthesis over dissolution, this is the effect presented in Figure 20(a). At lower magnification, however, the electron dose was reduced, and nucleation was insufficient to sustain NA growth, as presented in Figure 20(b). Presented observations align with Schneider et al.'s theoretical model, which posits that ions require electrons for reduction and nucleation. Electron concentration in the irradiated region rises rapidly, but is readily scavenged by molecular oxygen, while H^+ ions, potentially responsible for dissolution, persist longer throughout the cell. Thus, in high-magnification

imaging, both radical H^+ ions and electrons are supplied to the sample, but the high dose rate drives nucleation. Under low magnification, electron availability is lower, limiting nucleation while H^+ ions can still form and promote nanoparticle dissolution. This supports Plakhova et al.'s model of reductive dissolution.

Dissolution of *ex-situ* synthesized ceria NAs in water

In Figure 21 effects of imaging ceria NAs in pure water are presented. No dissolution was observed, when the flow rate was faster than 0.8 µl/s, Figure 21(a). Only after reducing the flow rate to 0.5 µl/s etching of the spheres could have been noticed, Figure 21(b). This observation might again support the idea of reductive dissolution. In pure water there was probably a high concentration of H^+ and their reductive influence was dominant. But what is worth noting here, it was possible to suppress the dissolution effect by increasing the water flow rate. With higher flow rate, radical agents were flushed away from the imaging area too fast and apparently, they could not interact with the ceria structures.

However, this model does not fully explain, why dissolution occurred only in the *in-situ* synthesized ceria and not in the pre-synthesized NAs. Therefore, it is worth considering, that NA morphology is the critical factor. The pre-synthesized sample comprises spherical nanoparticles that, under beam exposure, form an additional ceria layer, creating a protective shell, that increases diffusion distance for radicals. As a result, radicals are less likely to interact with these nanoaggregates – a phenomenon previously noted in ceria-radical interaction studies (Schlick et al., 2016). In contrast, the *in-situ*-synthesized sample was strongly aggregated, highly porous, and sponge-like, making it more accessible to radicals and ultimately more prone to dissolution. Thus, besides chemical factors like pH and radical presence, physical factors such as particle size and agglomeration must also be considered *in-situ* experiments.

To summarize, concentration of radiolytic products will be different depending on the type of the used liquid. The electron beam should decrease the pH of water in the liquid cell, but according to some models, the pH would be increase in solutions containing Ce ions, because of localized OH^- ions production. This is why the beam can successfully induce ceria nucleation, but after longer exposure, it causes dissolving. The pH fluctuations depend on the time exposure and beam intensity, shifting up or down. This could be consistent with the Schneider's model, since it says that the level of H_3O^+ ions remains high, longer than the level of hydrated electrons, which can be scavenged by other species. According to Abellan's model, the pH should increase under the beam, but they do not take into account all the diffusion effects in the liquid cell, so this could be also one of the explanations for those contradicting results.

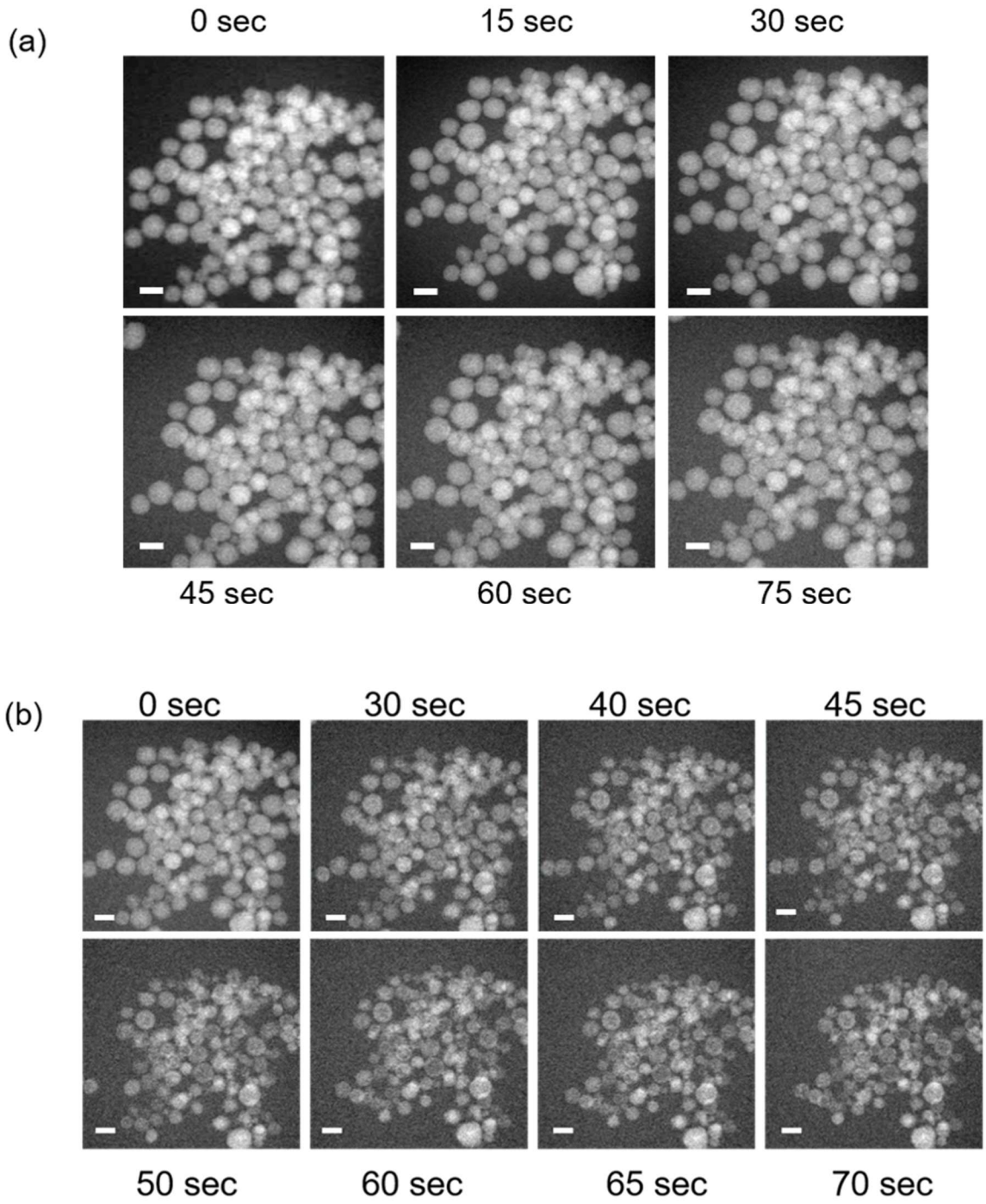

Figure 21 (a) Time frames extracted from Movie 5, no dissolution of the laboratory synthesized Ce_xO_y NAs under the beam in water with a flow rate of 0.8 µl/s; (b) Time frames extracted from Movie 6, dissolution of the laboratory synthesized Ce_xO_y NAs under the beam in water with a flow rate of 0.5 µl/s. Scale bar: 100 nm.

3.5.2. Ceria NAs decoration with Au NPs – *in-situ* experiment

In Figure 22 and Figure 23 the time frames from the decoration experiment in LC-TEM are presented.

Dynamic variant with flow of 1 mM $HAuCl_4$ solution at a flow rate of 1 µl/s and electron dose of 0.04 $e^-/Å^2s$ – it was not possible to catch the very initial steps of Au NPs deposition, nevertheless it is quite clear that large gold particles grow rapidly, overlapping ceria NAs, see Figure 22.

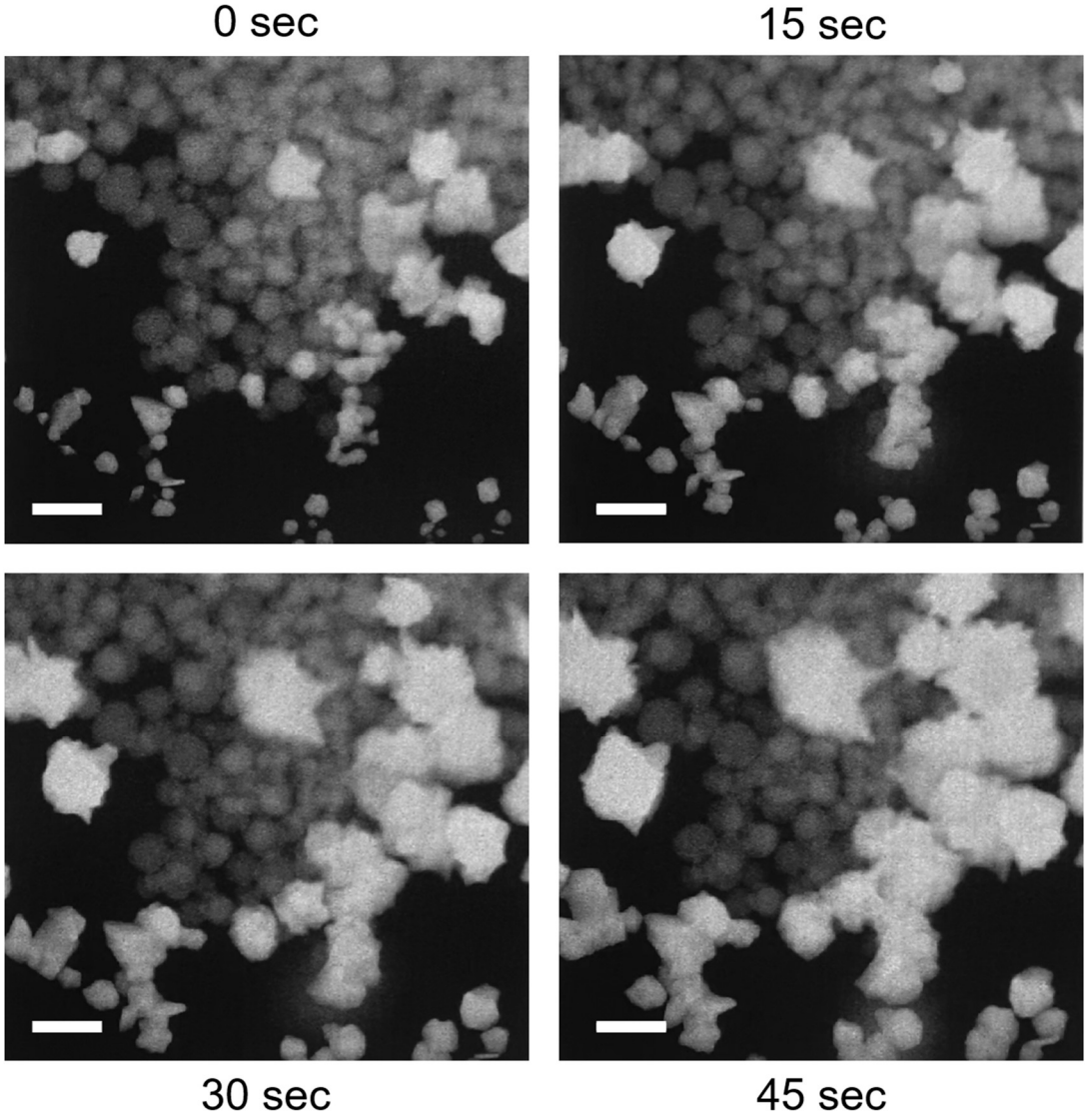

Figure 22 Au NPs synthesis on ceria NAs surface in LC-TEM during dynamic experiment. Extracted from Movie 7. Scale bar: 200 nm.

Static variant when the liquid cell was only filled with 1 mM $HAuCl_4$ solution (without flow) and electron dose of 0.04 $e^-/Å^2s$ – despite the same dose rate, Au deposits much slower, starting with the tiny nanospheres like in the *ex-situ* experiments. The static experiment of Au NPs synthesis can be seen in Figure 23.

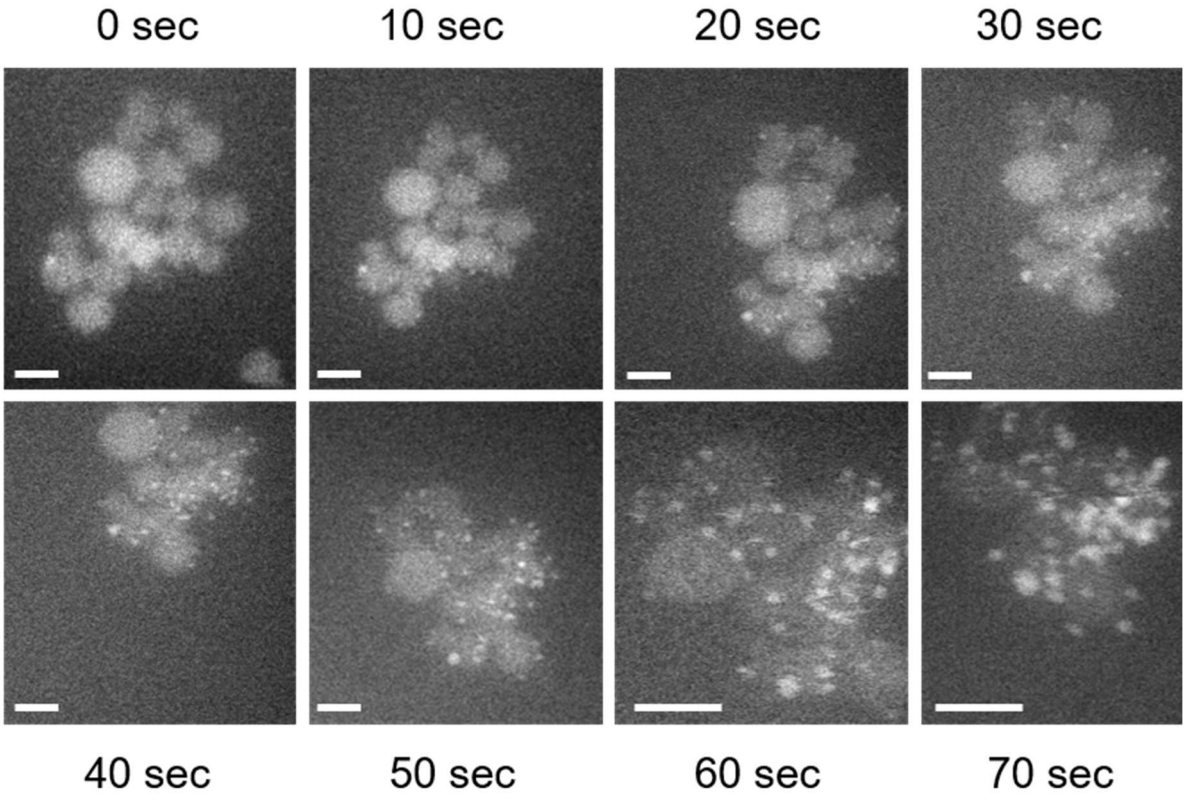

Figure 23 Au NPs synthesis on ceria NAs surface in LC-TEM during static experiment. Extracted from Movie 8. Scale bar: 100 nm.

The purpose of these experiments was to use the electron beam as a reducing agent for Au nanoparticle nucleation and to examine the influence of flow on the growth of Au structures, hence the static and dynamic setups. The results showed immediate Au structures growth on ceria NAs surface in both setups, although with different dynamics. However, unlike the uniform spheres formed *ex-situ*, these structures were clearly larger, star-like shaped and were partially covering the ceria. The difference in the dynamics is probably due to the access to fresh solution. When the flow is active, gold ions are being provided to the ceria constantly and easily reduced by the scanning beam. In static variant however, reaction is limited by diffusion of gold ions in the liquid cell. *Post-mortem* analysis of the disassembled LC from both experiments revealed other interesting variations, see Figure 24. There were distinct differences in Au morphology between the top chip (Figure 24(a)) and bottom chip (Figure 24(b)) from the dynamic experiment. On the top chip, the same large Au NPs were observed as during *in-situ* experiments; in some cases, they were looking more like stars, covering several ceria spheres, although only a few gold-ceria nanostructures were found, suggesting that most large structures formed in the liquid between the chips and were likely flushed away by liquid flow. On the

bottom chip, only tiny Au NPs decorating the ceria NAs were identified and they were very similar to the morphology of the *ex-situ* synthesized catalyst. Morphologically, structures on the bottom chip were consistent between both static and dynamic experiments, so the flowing did not affect the resulting structures. Two vital results can be brought from those experiments: (1) processes on the top chip are mostly controlled by the effects of the solution flow, while (2) processes on the bottom chip are mainly controlled by the effects of the electron beam.

This difference may be due to electron beam scattering within the liquid layer of the LC. As the electron beam transduce through the liquid cell, it loses energy through inelastic collisions with water molecules, yet the cascading chain of secondary reactions continues to propagate (Korpanty et al., 2022; Lee et al., 2021). This cascade expands both in the spatial distribution and the number of generated radicals as the penetration depth increases. By the time the electrons reach the bottom of the liquid cell, the radial distribution of the cascade has broadened significantly due to the increasing cross-sectional area of scattering events. This phenomenon highlights the interplay between the electron energy deposition profile, the diffusion of radical species, and the geometry of the reactor, all of which influence the spatial dynamics of chemical reactions initiated by radiolysis. Therefore, Au NPs deposited at the bottom are more numerous, although their size is smaller due to this lowered energy.

In the static experiment, from the EDS maps, the ceria nanoaggregates appear to be fully enveloped by Au, see Figure 24(c) and Figure 24(d). Gold covering ceria NAs is visible on both the top and the bottom chips. This suggests that without the flow, the electron beam generates more reducing agents, that are not flushed away from the scanned area. This effect induces much more intensive Au deposition, which leads to forming a thin golden coverage around the nanoaggregates.

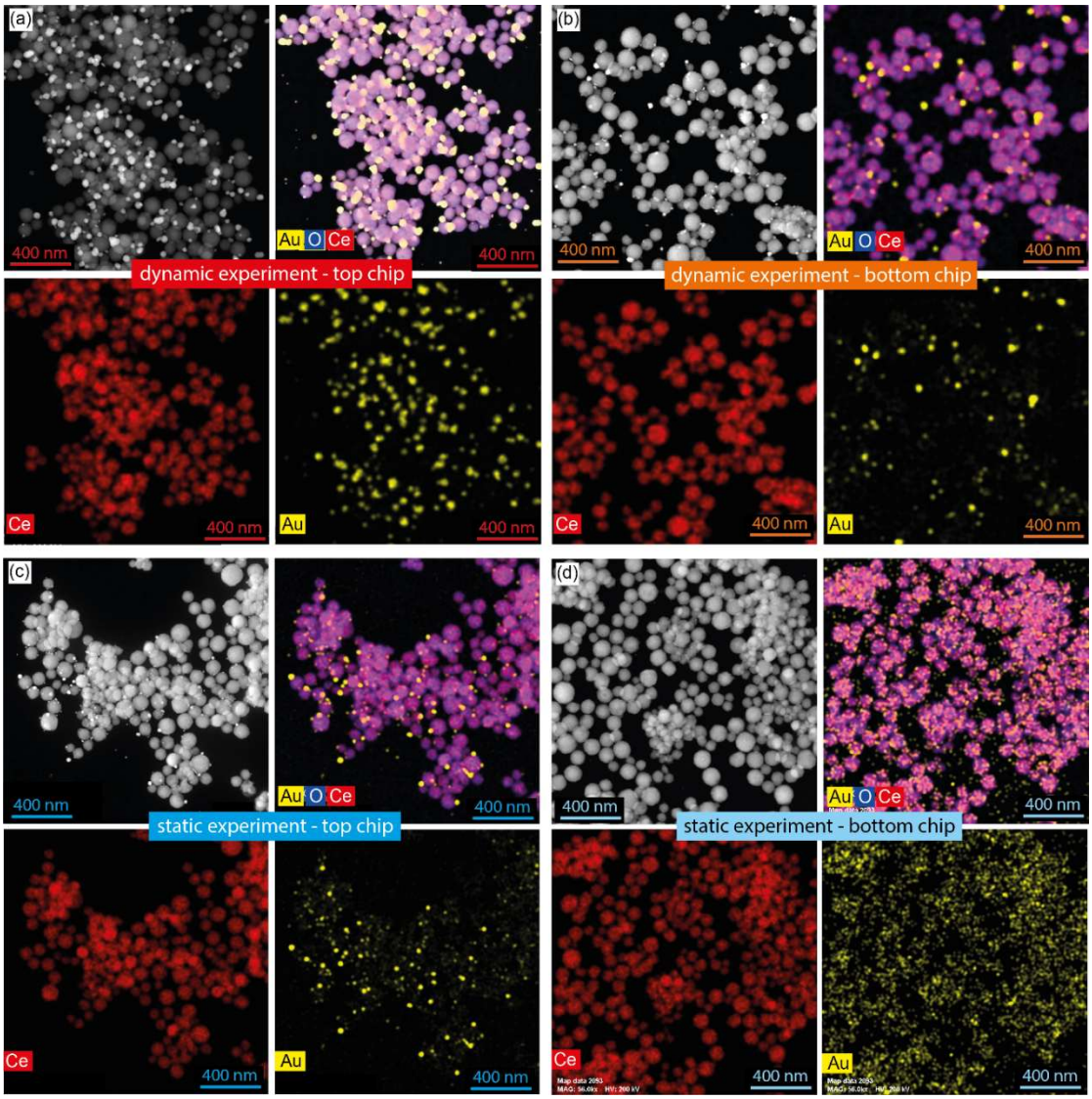

Figure 24 STEM-HAADF images of the ceria NAs decorated with Au NPs with the corresponding EDS maps, showing Ce, O and Au distribution. (a) top chip, dynamic experiment, large Au NPs are covering ceria NAs; (b) bottom chip, dynamic experiment, Au NPs are noticeably smaller; (c) top chip, static experiment, Au forms nanoparticles decorating the ceria NAs, but also forms a coverage on the whole NAs; (d) bottom chip, static experiment, Au coverage is again visible on the whole NAs.

The main goal of the static experiment, however, was to investigate the potential diffusion effects of radical agents within the liquid cell. The idea was to determine whether irradiating a localized region of the sample with the electron beam would influence the outcomes in other areas within the liquid cell and what distance would these effect reach. If diffusion occurred, the next step would be to explore whether there would be observable differences between regions directly exposed to the electron beam and those not exposed and at what distance between them. To test this hypothesis, during the experiment, the electron beam was focused on one edge of a silicon nitride window within the liquid cell.

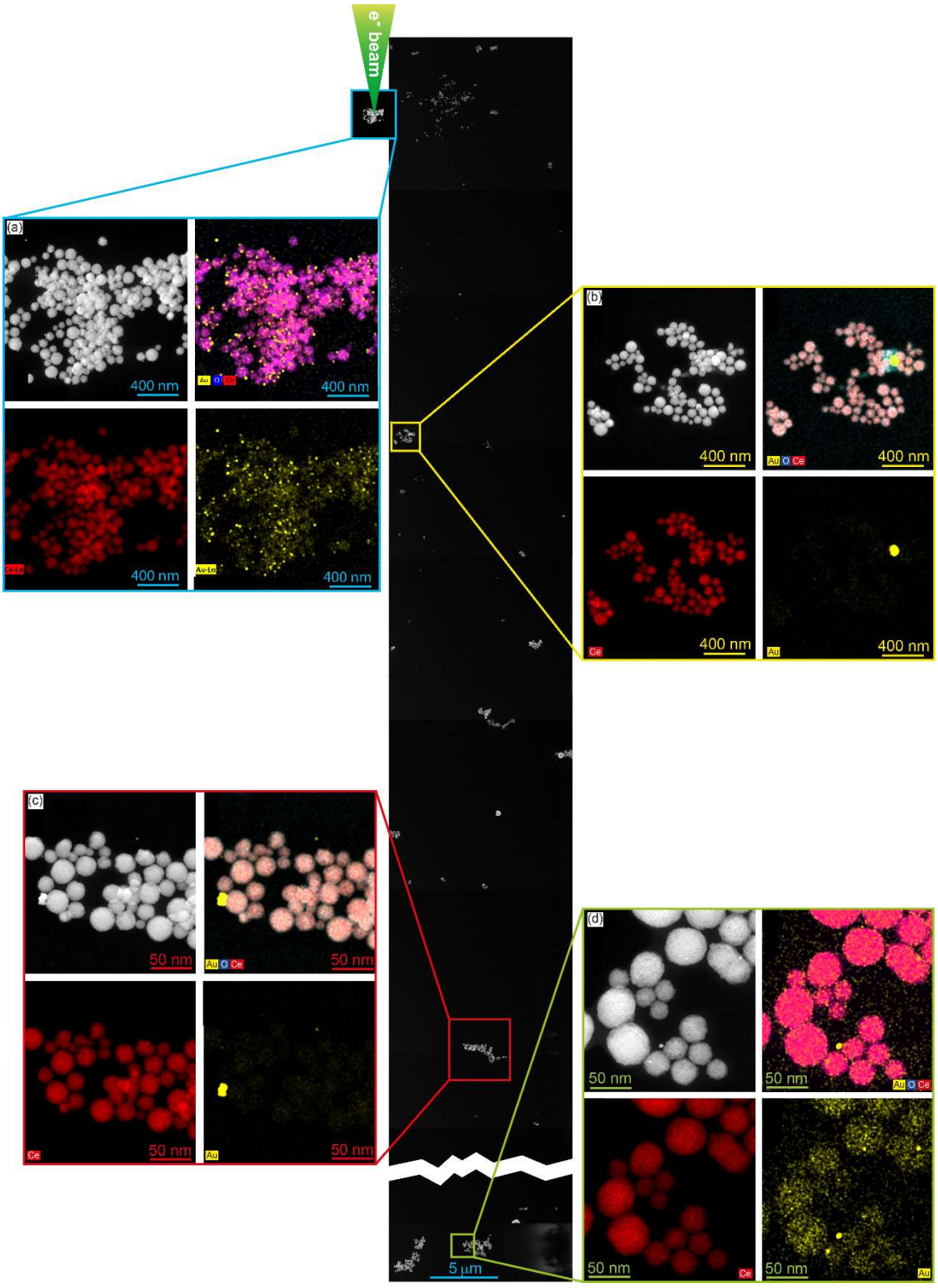

Figure 25 Post-mortem investigation of the top e-chip from the static experiment. Central image of the SiN membrane acquired step-by-step from the illuminated (top) to the non-illuminated (bottom) area. EDS maps of the Au decorated ceria NAs were taken from different areas of the chip. See main text for details.

This localized irradiation generated radical species in a confined area and the results of beam induced synthesis were described above and presented in Figure 25. Subsequently, after the experiment in liquid, the e-chip was imaged under *post-mortem* conditions to assess any spatial variations within the liquid cell. Using a step-by-step approach, HAADF images were captured along the entire length of the SiN window. This allowed us to systematically evaluate the effects of radical's diffusion and compare irradiated regions with non-irradiated ones. The results of this methodology are shown also in Figure 25. In the area illuminated by the electron beam, growth of numerous Au NPs was observed, which is confirmed by EDS mapping, Figure 25(a). On the other hand, images taken in the non-illuminated areas, show only some individual Au NPs, Figure 25(b-d). They are noticeably bigger than the ones in Figure 25(a), as they have most probably grown during searching for the e-chip window at low magnification in the TEM – therefore their large sizes. The beam was focused locally, inducing high amount of reducing agents to nucleate and synthesize the Au crystals. In the static experiment there were apparently some diffusion effects. It allowed radical agents – primarily hydrated electrons in this case – to reach the surface of the ceria nanoaggregates and trigger gold deposition throughout the liquid cell.

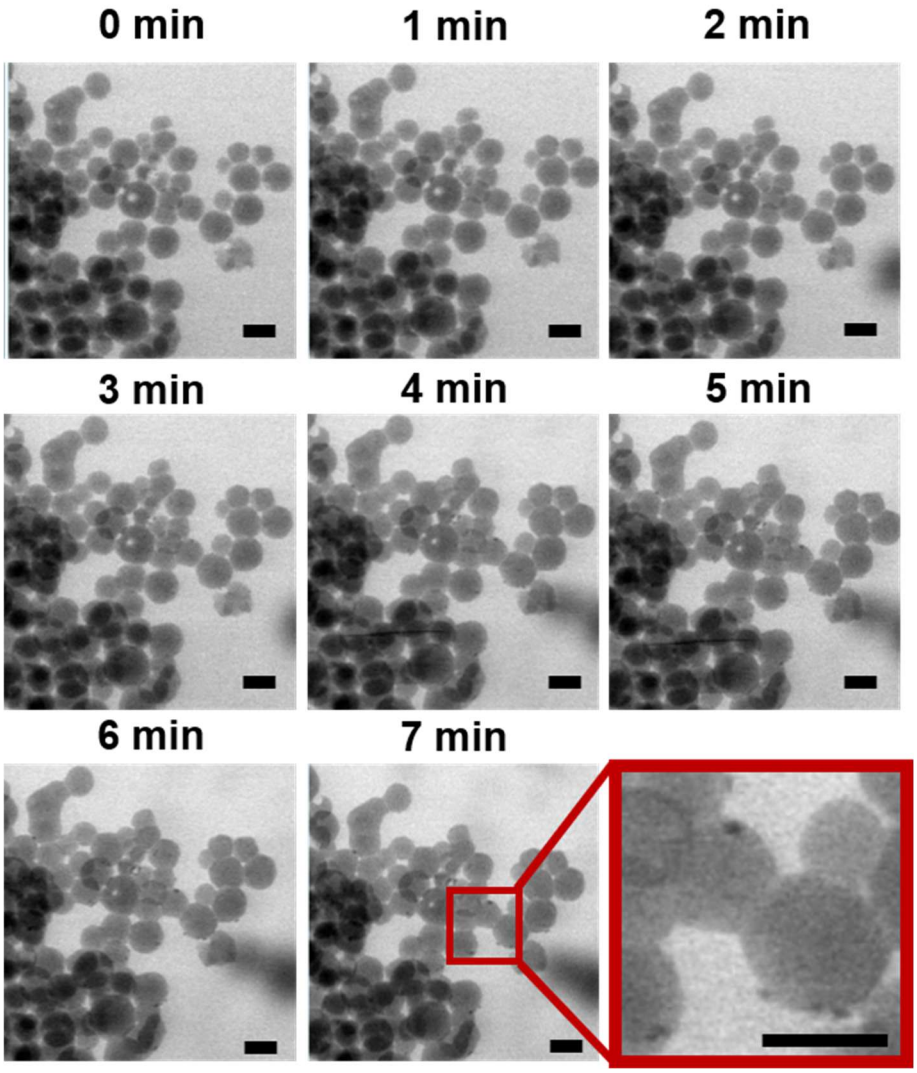

Figure 26 Au NPs deposition in LC-TEM from 0.1 mM solution. Extracted from Movie 9. Scale bar: 100 nm.

Ceria NAs decorated with Au NPs at low concentration (0.1 mM $HAuCl_4$ solution) at a flow rate of 0.05 µl/s and electron dose of 11 $e^-/Å^2s$ – the large star-like, large sized Au structures were unexpected and undesired for the catalytic applications discussed in this thesis, therefore, the experiment was repeated with 0.1 mM $HAuCl_4$ solution. Despite much higher dose rate, the synthesis was slow at such extremely low concentration. Nevertheless after 3 minutes of constant illumination some tiny Au nanoparticles started to appear and slowly grow, see Figure 26.

4. Summary and conclusion

The presented study explored the synthesis, transformation, and behavior of multicomponent nanosystem composed of ceria nanoaggregates decorated with Au nanoparticles. The main goal of this thesis was to analyze the influence of the electron beam in the TEM on the observed reaction, providing novel insights into the evolution of the nanosystem and into the effects that may occur during LC-TEM experiments. The described results provide valuable insights into the real-time imaging of nanomaterials, presenting a deep analysis of the synthesis mechanisms, the beam effects and how to minimize them. The main conclusions of this thesis can be divided in the following paragraphs:

Structural evolution and pH fluctuations – in the first experiment, cerium oxide was synthesized directly from a precursor using the electron beam as reducing agent. It was demonstrated, that the electrons can be used to initiate nucleation and stimulate the *in-situ* synthesis of metal oxide nanostructures directly within the liquid cell. The beam-induced crystallization is rapid and leads to the formation of vast, foam-like structure composed of very small nanospheres.

Furthermore, depending on the electron dose rate, the beam could be used either to induce growth or dissolution of the nanoaggregates. This kind of observations is highly valuable for the liquid phase microscopy field, as it highlights the main challenges of the LC-TEM experiments. As this thesis presents, the electron beam ion-reducing influence is one thing, but its impact of the pH level is even more crucial. It seems that those two effects contradict each other, and depending on the time and applied electron dose rate, one of them prevails.

For the ceria synthesis on the pre-synthesized ceria NAs, there was an obvious dose rate dependency – intense nucleation was visible at high magnification, i. e. high electron dose, whereas dissolution started at lower magnification, i.e. low electron dose. This effect can be explained by the co-existence of two opposite forces. Nucleation prevails at high magnification with strong hydrated electrons generation, but their amount is limited at lower dose rate; electrons are scavenged, while other ions' concentration remains high and the effect of reductive dissolving surpasses. An attempt to identify this threshold, at which these two trends switch, would be undoubtedly exciting and valuable for the community and the field, although such project would be time- and cost-consuming. And it would be probably very hard to apply such model for different materials. Furthermore, pre-synthesized ceria nanoaggregates exhibited greater resistance to dissolution compared to *in-situ* synthesized ones. This resistance was attributed to some kind of a protective shell, which increased the diffusion distance for radicals, reducing their interaction with the nanoaggregate core. In contrast, *in-situ*-synthesized nanoaggregates formed highly porous, sponge-like structures, making them more susceptible to pH-driven degradation. These results indicate that both chemical (pH) and physical (morphology) factors must be considered in LC-TEM studies to accurately interpret dissolution dynamics.

Finally, a flow-rate dependency was registered during presented experiments in pure water. Dissolution of ceria NAs occurred when the flow rate was below 0.5 µl/s and was not observed at higher flow rates (>0.8 µl/s), which was explained by fluxing away all the radicals from the liquid cell, before they could interact with the pre-synthesised nanostructures. This

phenomenon suggests that controlled liquid flow can mitigate radiolytic dissolution, making it a valuable parameter for optimizing LC-TEM experiments. It is a simple yet effective strategy to prevent nanostructures from degradation.

Gold decoration – two experiments were performed, with and without the flow of Au precursor. Furthermore, the effects of gold crystallization both on the top and bottom chip were analyzed.

In the LC-TEM movies it is presented that the flow of solution in the dynamic variant influences the Au nucleation and growth dynamics, providing fresh ions and leading to a formation of large star-like structures on the ceria NAs surface. On the other hand, in the static variant, where there is a limited concentration of gold ions, only the formation of small Au NPs was observed, resulting in a similar structure like in the *ex-situ* experiments. Growth dynamics was even slower, during the decoration using 0.01 mM solution of gold precursor, which was also presented in the movie. In any case, the electron beam was very effective in crystallization of gold nanostructures and no other reducing agent was used.

The *post-mortem* analysis of both chips from the static and dynamic experiment revealed another interesting effect. While it was reported before, that the electron beam loses its energy, transducing through the liquid layer inside the cell, there is lack of reports about how this energy loss affects the nanostructures inside. Here, this effect was demonstrated during the decoration with Au and the dependency is especially visible in the dynamic experiment. The star-like structures that were observed in the *in-situ* experiment are visible only on the top chip, whereas on the bottom chip numerous tiny Au nanoparticles were identified, which suggests broadened radial distribution of the electrons, yet their sizes were very small, confirming that the energy of the electron beam reduced because of the scattering in liquid.

Finally, a series of step-by-step images of the membrane from the static experiment was presented, to investigate diffusion effects of the precursor in conditions without the flow. Presented results indicate that electron beam exposure can induce the formation of a thin gold coverage around ceria nanoaggregates, while structures formed in non-illuminated areas maintain a morphology similar to *ex-situ* samples. Additionally, diffusion effects allow radical agents, particularly hydrated electrons, to reach ceria surfaces and facilitate gold deposition even without direct electron beam interaction.

Electrochemical experiments – a wide analysis of the $Au@Ce_xO_y/C$ catalytic system for the EOR was performed. Cyclic voltammetry measurements showed, that the studied system is more effective than a pure Au/C catalyst. The activity was also examined during a 3-hours measurement by IRRAS, to analyze the products in real time and demonstrated that $Au@Ce_xO_y/C$ successfully breaks the carbonic bond in ethanol, leading to high and efficient generation of CO_2 with limited generation of other, non-desirable by-products. It confirms the positive effect of using the ceria NAs as supports and reinforces the idea of fabricating multicomponent catalysts, that are both less expensive and more active.

Main conclusions for this work can be presented as following:

- The electron beam in TEM may be used to generate reducing agents for synthesis of ceria nanostructures. But depending on the electron dose rate and the relation between concentration of radicals and pH fluctuations, the beam may be also used to dissolve the nanostructures.
- Ceria NAs fabricated *ex-situ* were more stable in LC-TEM than the structures synthesized under the beam, because of their less porous morphology.
- The flow rate may be a crucial parameter for LC-TEM experiments and by adjusting it, beam induced dissolution of nanomaterials can be suppressed. It also may influence the morphology of the nanomaterials fabricated during LC-TEM.
- During LC-TEM experiments, the energy of the electron beam is reduced due to transducing and scattering in the liquid. Therefore, structures fabricated on the bottom e-chip differ from the ones fabricated on the top e-chip.
- The fabricated Au@Ce_xO_y/C catalyst is more active towards EOR and CO_2 generation than pure Au/C catalyst, which is due to better oxygen mobility and availability provided by redox processes on ceria NAs.

In this thesis, the effects of pH and flow-rate during the LC-TEM experiments were widely and deeply examined and discussed. One of the primary challenges in liquid-phase TEM studies is electron beam-induced radiolysis, which can lead to unintended chemical reactions and significantly alter the experimental environment. Here, these effects were investigated. The presented results are useful in preparing methodologies for LC-TEM experiments, with new strategies of avoiding those undesired beam effects. This is crucial for conducting more reliable experiments in liquid phase microscopy, especially when it comes to synthesis of multicomponent nanosystems.

Another valuable strategy that is discussed here is a wide *post-mortem* analysis of both top and bottom chips with the step-by-step imaging of the SiN_x window. It provides much more details, presenting spatial distribution of materials. It also reveals differences in morphology determined by the local effects of the electron beam, which is necessary to reliably analyze the impact of the beam. It also reveals the strong role of diffusion effects in those processes. All those strategies can improve accuracy of the LC-TEM experiments.

Beyond addressing fundamental challenges, the findings of this dissertation have broader implications for the field of nanoscience, particularly in catalysis, materials synthesis and the development of functional nanomaterials. Understanding the role of pH variations and radiolysis in nanostructures behavior enables researchers to design more stable and controllable nanosystems for a wide range of applications. Furthermore, the presented methodologies are a valuable contribution to the liquid phase electron microscopy field, revealing and proving how powerful is this technique and how wide studies can be performed with it.

5. Literature

1. Abad, A., Concepción, P., Corma, A., & García, H. (2005). A collaborative effect between gold and a support induces the selective oxidation of alcohols. *Angewandte Chemie International Edition*, *44*(26), 4066-4069.

2. Abellan, P., Mehdi, B. L., Parent, L. R., Gu, M., Park, C., Xu, W., Zhang, Y., Arslan, I., Zhang, J-G., Wang, C-M., Evans, J. E. & Browning, N. D. (2014). Probing the degradation mechanisms in electrolyte solutions for Li-ion batteries by *in-situ* transmission electron microscopy. *Nano letters*, *14*(3), 1293-1299.

3. Abbe, E. (1882). The Relation of Aperture and Power in the Microscope (continued). *Journal of the Royal Microscopical Society*, 2(*4*), 460-473.

4. Abellan, P., Moser, T. H., Lucas, I. T., Grate, J. W., Evans, J. E., & Browning, N. D. (2017). The formation of cerium (III) hydroxide nanoparticles by a radiation mediated increase in local pH. *RSC advances*, 7(*7*), 3831-3837.

5. Abrams, I. M., & McBain, J. W. (1944). A closed cell for electron microscopy. *Science*, 100(*2595*), 273-274.

6. Alagarasi, A. (2013). Introduction to nanomaterials. *Indian Institute of Technology Madras*, 1-24.

7. Amendola, V., & Meneghetti, M. (2009). Laser ablation synthesis in solution and size manipulation of noble metal nanoparticles. *Physical chemistry chemical physics*, *11*(20), 3805-3821.

8. Asghar, M. S. A., Inkson, B. J., & Möbus, G. (2017). Giant Radiolytic Dissolution Rates of Aqueous Ceria Observed *in-situ* by Liquid-Cell TEM. *ChemPhysChem*, *18*(10), 1247-1251.

9. Asghar, M. S. A., Inkson, B. J., & Möbus, G. (2017). Giant Radiolytic Dissolution Rates of Aqueous Ceria Observed *in-situ* by Liquid-Cell TEM. *ChemPhysChem*, *18*(10), 1247-1251.

10. Bakonyi, I., Tóth-Kádár, E., Tarnoczi, T., Varga, L. K., Cziraki, A., Geröcs, I., & Fogarassy, B. (1993). Structure and properties of fine-grained electrodeposited nickel. *Nanostructured Materials*, *3*(1-6), 155-161.

11. Baletto, F., Mottet, C., & Ferrando, R. (2001). Microscopic mechanisms of the growth of metastable silver icosahedra. *Physical Review B*, *63*(15), 155408.

12. Becerril-Castro, I. B., Calderon, I., Pazos-Perez, N., Guerrini, L., Schulz, F., Feliu, N., ... & Alvarez-Puebla, R. A. (2022). Gold nanostars: Synthesis, optical and SERS analytical properties. *Analysis & Sensing*, *2*(3), e202200005.

13. Bianconi, A., Marcelli, A., Dexpert, H., Karnatak, R., Kotani, A., Jo, T., & Petiau, J. (1987). Specific intermediate-valence state of insulating 4f compounds detected by L 3 X-ray absorption. *Physical Review B*, *35*(2), 806.

14. Bozzini, B., D'Urzo, L., Gianoncelli, A., Kaulich, B., Kiskinova, M., Prasciolu, M., & Tadjeddine, A. (2008). *In-situ* soft X-ray dynamic microscopy of electrochemical processes. *Electrochemistry communications*, *10*(11), 1680-1683.

15. Bozzini, B., D'Urzo, L., Gianoncelli, A., Kaulich, B., Prasciolu, M., Sgura, I., Tondo, E. & Kiskinova, M. (2009). An *in-situ* synchrotron-based soft X-ray microscopy investigation of Ni electrodeposition in a thin-layer cell. *The Journal of Physical Chemistry C*, *113*(22), 9783-9787.

16. Breysse, M., Guenin, M., Claudel, B., Latreille, H., & Véron, J. (1972). Catalysis of carbon monoxide oxidation by cerium dioxide: I. Correlations between catalytic activity and electrical conductivity. *Journal of Catalysis*, *27*(2), 275-280.

17. Bunluesin, T., Gorte, R. J., & Graham, G. W. (1998). Studies of the water-gas-shift reaction on ceria-supported Pt, Pd, and Rh: Implications for oxygen-storage properties. *Applied Catalysis B: Environmental*, *15*(1-2), 107-114.

18. Carrettin, S., Concepción, P., Corma, A., López Nieto, J. M., & Puntes, V. F. (2004). Nanocrystalline CeO2 increases the activity of Au for CO oxidation by two orders of magnitude. *Angewandte Chemie International Edition*, *43*(19), 2538-2540.

19. Carter, C. B., & Williams, D. B. (Eds.). (2016). Transmission electron microscopy: Diffraction, imaging, and spectrometry. *Springer*.

20. Caruso, F., Shi, X., Caruso, R. A., & Susha, A. (2001). Hollow titania spheres from layered precursor deposition on sacrificial colloidal core particles. *Advanced Materials*, *13*(10), 740-744.

21. Cazaux, J. (1995). Correlations between ionization radiation damage and charging effects in transmission electron microscopy. *Ultramicroscopy*, *60*(3), 411-425.

22. Chee, S. W., Pratt, S. H., Hattar, K., Duquette, D., Ross, F. M., & Hull, R. (2015). Studying localized corrosion using liquid cell transmission electron microscopy. *Chemical Communications*, 51(*1*), 168-171.

23. Chen, Y., Hu, P., Lee, M. H., & Wang, H. (2008). Au on (1 1 1) and (1 1 0) surfaces of CeO2: A density-functional theory study. *Surface Science*, *602*(10), 1736-1741.

24. Chen, Z., Cui, Z. M., Niu, F., Jiang, L., & Song, W. G. (2010). Pd nanoparticles in silica hollow spheres with mesoporous walls: a nanoreactor with extremely high activity. *Chemical communications*, *46*(35), 6524-6526.

25. Chen, Z., Cui, Z. M., Li, P., Cao, C. Y., Hong, Y. L., Wu, Z. Y., & Song, W. G. (2012). Diffusion induced reactant shape selectivity inside mesoporous pores of Pd@ meso-SiO2 nanoreactor in Suzuki coupling reactions. *The Journal of Physical Chemistry C*, *116*(28), 14986-14991.

26. Choi, S. H., Na, H. B., Park, Y. I., An, K., Kwon, S. G., Jang, Y., Park, M-h., Moon, J., Son, J. S., Song, I. C., Moon, W. K. & Hyeon, T. (2008). Simple and generalized synthesis of oxide− metal heterostructured nanoparticles and their applications in multimodal biomedical probes. *Journal of the American Chemical Society*, *130*(46), 15573-15580.

27. Claus, P. (2005). Heterogeneously catalysed hydrogenation using gold catalysts. *Applied Catalysis A: General*, *291*(1-2), 222-229.

28. Cleveland, C. L., & Landman, U. (1991). The energetics and structure of nickel clusters: Size dependence. *The Journal of chemical physics*, *94*(11), 7376-7396.

29. Dahle, J. T., Livi, K., & Arai, Y. (2015). Effects of pH and phosphate on CeO2 nanoparticle dissolution. *Chemosphere*, *119*, 1365-1371.

30. Daigle, E. (2019). Microcell fabrication and resolution enhancement for *in-situ* liquid cell electron microscopy. PhD Thesis, McMaster University, Canada.

31. Deng, D., Yu, L., Chen, X., Wang, G., Jin, L., Pan, X., Deng, J., Sun, G. & Bao, X. (2013). Iron encapsulated within pod-like carbon nanotubes for oxygen reduction reaction. *Angewandte Chemie*, *125*(1).

32. Deshpande, S., Patil, S., Kuchibhatla, S. V., & Seal, S. (2005). Size dependency variation in lattice parameter and valency states in nanocrystalline cerium oxide. *Applied Physics Letters*, *87*(13).

33. Din, M. I., & Rehan, R. (2017). Synthesis, characterization, and applications of copper nanoparticles. *Analytical Letters*, *50*(1), 50-62.

34. Drake, I. J., Liu, T. C., Gilles, M., Tyliszczak, T., Kilcoyne, A. D., Shuh, D. K., Mathies, R. A. & Bell, A. T. (2004). An *in-situ* cell for characterization of solids by soft x-ray absorption. *Review of scientific instruments*, *75*(10), 3242-3247.

35. Drexler, K. E. (1986). Engines of creation: the coming era of nanotechnology. *Anchor Book, New York*, 1-10.

36. Dutta, P., Pal, S., Seehra, M. S., Shi, Y., Eyring, E. M., & Ernst, R. D. (2006). Concentration of Ce3+ and oxygen vacancies in cerium oxide nanoparticles. *Chemistry of Materials*, *18*(21), 5144-5146.

37. Esch, F., Fabris, S., Zhou, L., Montini, T., Africh, C., Fornasiero, P., Comelli, G., & Rosei, R. (2005). Electron localization determines defect formation on ceria substrates. *Science*, *309*(5735), 752-755.

38. Eskelsen, J. R., Xu, J., Chiu, M., Moon, J. W., Wilkins, B., Graham, D. E., Gu, B. & Pierce, E. M. (2018). Influence of structural defects on biomineralized ZnS nanoparticle dissolution: an in-situ electron microscopy study. *Environmental science & technology*, *52*(3), 1139-1149.

39. Faro, M. L., La Rosa, D., Antonucci, V., & Arico, A. S. (2009). Intermediate temperature solid oxide fuel cell electrolytes. *Journal of the Indian Institute of Science*, *89*(4), 363-380.

40. Feynman, R. P. (1960). There's plenty of room at the bottom. *Engineering and Science*, *23*(5), 22-36.

41. Findik, F. (2021). Nanomaterials and their applications. *Period. Eng. Nat. Sci*, *9*(3), 62-75.

42. Fritsch, B., Körner, A., Couasnon, T., Blukis, R., Taherkhani, M., Benning, L. G., Jank, M. P. M., Spiecker, E. & Hutzler, A. (2023). Tailoring the Acidity of Liquid Media with Ionizing Radiation: Rethinking the Acid–Base Correlation beyond pH. The journal of physical chemistry letters, 14(20), 4644-4651.

43. Fronzi, M., Piccinin, S., Delley, B., Traversa, E., & Stampfl, C. (2009). Water adsorption on the stoichiometric and reduced CeO 2 (111) surface: A first-principles investigation. *Physical Chemistry Chemical Physics*, *11*(40), 9188-9199.

44. Fu, Q., Weber, A., & Flytzani-Stephanopoulos, M. (2001). Nanostructured Au–CeO2 catalysts for low-temperature water–gas shift. *Catalysis Letters*, *77*, 87-95.

45. Fujiwara, K. (1961). Relativistic dynamical theory of electron diffraction. *Journal of the Physical Society of Japan*, 16(*11*), 2226-2238.

46. Gamler, J. T., Ashberry, H. M., Skrabalak, S. E., & Koczkur, K. M. (2018). Random alloyed versus intermetallic nanoparticles: a comparison of electrocatalytic performance. *Advanced Materials*, *30*(40), 1801563.

47. Gan, L., Heggen, M., O'Malley, R., Theobald, B., & Strasser, P. (2013). Understanding and controlling nanoporosity formation for improving the stability of bimetallic fuel cell catalysts. *Nano letters*, *13*(3), 1131-1138.

48. Gao, W., Hou, Y., Hood, Z. D., Wang, X., More, K., Wu, R., Xia, Y., Pan, X. & Chi, M. (2018). Direct *in-situ* observation and analysis of the formation of palladium nanocrystals with high-index facets. *Nano Letters*, *18*(11), 7004-7013.

49. Garrett, B. C., Dixon, D. A., Camaioni, D. M., Chipman, D. M., Johnson, M. A., Jonah, C. D., Kimmel, G.A., Miller, J.H., Rescigno, T.N., Rossky, P.J., Xantheas, S.S., Colson, S.D., Laufer, A. H., Ray, D., Barbara, P. F., Bartels, D. M., Becker, K. H., Bowen Jr., K. H., Bradforth, S. E., Carmichael, I., Coe, C. V., Corrales, L. R., Cowin, J. P., Dupuis, M., Eisenthal, K. B., Franz, J. A., Gutowski, M. S., Jordan, K. D., Kay, B. D., LaVerne, J. A., Lymar, S. V., Madey, T. E., McCurdy, C. W., Meisel, D., Mukamel, S., Nilsson, A. R., Orlando, T. M., Petrik, N. G., Pimblott, S. M., Rustad, J. R., Schenter, G. K., Singer, S. J., Tokmakoff, A., Wang, L-S. & Zwier, T. S. (2004). Role of water in electron-initiated processes and radical chemistry: Issues and scientific advances. *Chemical reviews*, *105*(1), 355-390.

50. Gawande, M. B., Branco, P. S., Parghi, K., Shrikhande, J. J., Pandey, R. K., Ghumman, C. A. A.,Bundaleski, N., Teodoro, O. M. N. D. & Jayaram, R. V. (2011). Synthesis and

characterization of versatile MgO–ZrO 2 mixed metal oxide nanoparticles and their applications. *Catalysis Science & Technology*, *1*(9), 1653-1664.

51. Gawande, M. B., Goswami, A., Felpin, F. X., Asefa, T., Huang, X., Silva, R., Zou, X., Zboril, R., & Varma, R. S. (2016). Cu and Cu-based nanoparticles: synthesis and applications in catalysis. *Chemical reviews*, *116*(6), 3722-3811.

52. de Groot, F. M., de Smit, E., van Schooneveld, M. M., Aramburo, L. R., & Weckhuysen, B. M. (2010). In-situ scanning transmission X-ray microscopy of catalytic solids and related nanomaterials. *ChemPhysChem*, *11*(5), 951-962.

53. Giannozzi, P., Baroni, S., Bonini, N., Calandra, M., Car, R., Cavazzoni, C., Ceresoli, D., Chiarotti, G. L., Cococcioni, M., Dabo, I., Dal Corso, A., Fabris, S., Fratesi, G., de Gironcoli, S., Gebauer, R., Gertsmann, U., Gougoussis, C., Kokalj, A., Lazzeri, M., Martin-Samos, L., Marzari, N., Mauri, F., Mazzarello, R., Paolini, S., Pasquarello, A., Paulatto, L., Sbraccia, C., Scandolo, S., Sclauzero, G., Seitsonen, A. P., Smogunov, A., Umari, P. & Wentzcovitch, R. M. (2009). QUANTUM ESPRESSO: a modular and open-source software project for quantum simulations of materials. *Journal of physics: Condensed matter*, *21*(39), 395502.

54. Giannozzi, P., Andreussi, O., Brumme, T., Bunau, O., Nardelli, M. B., Calandra, M., Car, R., Cavazzoni, C., Ceresoli, D., Cococcioni, M., Colonna, N., Carnimeo, I., Dal Corso, A., de Gironcoli, S., Delugas, P., DiStasio Jr., R. A., Ferretti, A., Floris, A., Fratesi, G., Fugallo, G., Gebauer, R., Gertsmann, U., Giustino, F., Gorni, T., Jia, J., Kawamura, M., Roza, H-Y., Paulatto, L., Poncé, S., Rocca, D., Sabatini, R., Santra, B., Schlipf, M., Seitsonen, A. P., Smogunov, A., Timrov, I., Thonhauser, T., Umari, P., Vast, N., Wu, X. & Baroni, S. (2017). Advanced capabilities for materials modelling with Quantum ESPRESSO. *Journal of physics: Condensed matter*, *29*(46), 465901.

55. Giannozzi, P., Baseggio, O., Bonfà, P., Brunato, D., Car, R., Carnimeo, I., Cavazzoni, C., de Gironcoli, S., Delugas, P., Ferrari Rufino, F., Ferretti, A., Marzari, N., Timrov, I., Urru, A. & Baroni, S. (2020). Quantum ESPRESSO toward the exascale. *The Journal of chemical physics*, *152*(15).

56. Ghosh Chaudhuri, R., & Paria, S. (2012). Core/shell nanoparticles: classes, properties, synthesis mechanisms, characterization, and applications. *Chemical reviews*, *112*(4), 2373-2433.

57. Gu, Q., Zhu, J., Weng, G. J., Li, J. J., & Zhao, J. W. (2022). Core-satellite nanostructures and their biomedical applications. *Microchimica Acta*, *189*(12), 470.

58. Guay, D., Stewart-Ornstein, J., Zhang, X., & Hitchcock, A. P. (2005). *In-situ* spatial and time-resolved studies of electrochemical reactions by scanning transmission X-ray microscopy. *Analytical chemistry*, *77*(11), 3479-3487.

59. Habas, S. E., Lee, H., Radmilovic, V., Somorjai, G. A., & Yang, P. (2007). Shaping binary metal nanocrystals through epitaxial seeded growth. *Nature materials*, *6*(9), 692-697.

60. Harris, P. J. F. (1986). Sulphur-induced faceting of platinum catalyst particles. *Nature*, 323(*6091*), 792-794.

61. He, K., Sawczyk, M., Liu, C., Yuan, Y., Song, B., Deivanayagam, R., Nie, A., Hu, X., Dravid, V. P., Lu, J., Sukotjo, C., Lu, Y-p., Kral, P., Shokuhfar, T. & Shahbazian-Yassar, R. (2020). Revealing nanoscale mineralization pathways of hydroxyapatite using *in-situ* liquid cell transmission electron microscopy. *Science Advances*, *6*(47), eaaz7524.

62. Head, A. R., Karslıoğlu, O., Gerber, T., Yu, Y., Trotochaud, L., Raso, J., Kerger, P. & Bluhm, H. (2017). CO adsorption on Pd (100) studied by multimodal ambient pressure X-ray photoelectron and infrared reflection absorption spectroscopies. *Surface Science*, *665*, 51-55.

63. Henglein, A. (1989). Non-metallic silver clusters in aqueous solution: stabilization and chemical reactions. *Chemical physics letters*, *154*(5), 473-476.

64. Ho, P. F., & Chi, K. M. (2004). Size-controlled synthesis of Pd nanoparticles from β-diketonato complexes of palladium. *Nanotechnology*, *15*(8), 1059.

65. Hofmeister, H., Nepijko, S. A., Ievlev, D. N., Schulze, W., & Ertl, G. (2002). Composition and lattice structure of fivefold twinned nanorods of silver. *Journal of crystal growth*, *234*(4), 773-781.

66. Hou, Y., Kondoh, H., Ohta, T., & Gao, S. J. A. S. S. (2005). Size-controlled synthesis of nickel nanoparticles. *Applied Surface Science*, *241*(1-2), 218-222.

67. Höller, R. P., Dulle, M., Thomä, S., Mayer, M., Steiner, A. M., Förster, S., Fery, A., Kuttner, C. & Chanana, M. (2016). Protein-assisted assembly of modular 3D plasmonic raspberry-like core/satellite nanoclusters: correlation of structure and optical properties. *ACS nano*, *10*(6), 5740-5750.

68. Hu, J., Dong, Y. L., ur Rahman, Z., Ma, Y. H., Ren, C. L., & Chen, X. G. (2014). *In-situ* preparation of core-satellites nanostructural magnetic-Au NPs composite for catalytic degradation of organic contaminants. *Chemical Engineering Journal*, *254*, 514-523.

69. Huang, W., & Gao, Y. (2014). Morphology-dependent surface chemistry and catalysis of CeO 2 nanocrystals. *Catalysis Science & Technology*, *4*(11), 3772-3784.

70. Huang, B., Gillen, R., & Robertson, J. (2014). Study of CeO2 and its native defects by density functional theory with repulsive potential. *The Journal of Physical Chemistry C*, *118*(42), 24248-24256.

71. Huang, Y. B., Wang, Q., Liang, J., Wang, X., & Cao, R. (2016). Soluble metal-nanoparticle-decorated porous coordination polymers for the homogenization of heterogeneous catalysis. *Journal of the American Chemical Society*, *138*(32), 10104-10107.

72. Hulliger, J. (1994). Chemistry and crystal growth. *Angewandte Chemie International Edition in English*, *33*(2), 143-162.

73. Idriss, H. (2004). Ethanol reactions over the surfaces of noble metal/cerium oxide catalysts. Platinum metals review, 48(3), 105-115

74. Iijima, S. (1991). Helical microtubules of graphitic carbon. *Nature*, *354*(6348), 56-58.

75. Jana, N. R., Gearheart, L., & Murphy, C. J. (2001). Seed-mediated growth approach for shape-controlled synthesis of spheroidal and rod-like gold nanoparticles using a surfactant template. *Advanced Materials*, *13*(18), 1389-1393.

76. Jayakrishnan, D. S. (2012). Electrodeposition: the versatile technique for nanomaterials. In *Corrosion protection and control using nanomaterials* (pp. 86-125). Woodhead Publishing.

77. Jeevanandam, J., Barhoum, A., Chan, Y. S., Dufresne, A., & Danquah, M. K. (2018). Review on nanoparticles and nanostructured materials: history, sources, toxicity and regulations. *Beilstein journal of nanotechnology*, *9*(1), 1050-1074.

78. Jia, Q., Caldwell, K., Strickland, K., Ziegelbauer, J. M., Liu, Z., Yu, Z., Ramaker, D. E. & Mukerjee, S. (2015). Improved oxygen reduction activity and durability of dealloyed PtCo x catalysts for proton exchange membrane fuel cells: strain, ligand, and particle size effects. *ACS catalysis*, *5*(1), 176-186.

79. Jia, Q., Li, J., Caldwell, K., Ramaker, D. E., Ziegelbauer, J. M., Kukreja, R. S., Kongkanad, A. & Mukerjee, S. (2016). Circumventing metal dissolution induced degradation of Pt-alloy catalysts in proton exchange membrane fuel cells: revealing the asymmetric volcano nature of redox catalysis. *ACS Catalysis*, *6*(2), 928-938.

80. Jiang, N. (2017). Note on *in-situ* (scanning) transmission electron microscopy study of liquid samples. *Ultramicroscopy*, *179*, 81-83.

81. de Jonge, N., & Ross, F. M. (2011). Electron microscopy of specimens in liquid. *Nature nanotechnology*, 6(*11*), 695-704.

82. Jungjohann, K. L., Bliznakov, S., Sutter, P. W., Stach, E. A., & Sutter, E. A. (2013). *In-situ* liquid cell electron microscopy of the solution growth of Au–Pd core–shell nanostructures. *Nano letters*, *13*(6), 2964-2970.

83. Kas, J. J., Vila, F. D., Pemmaraju, C. D., Tan, T. S., & Rehr, J. J. (2021). Advanced calculations of X-ray spectroscopies with FEFF10 and Corvus. *Journal of Synchrotron Radiation*, *28*(6), 1801-1810.

84. Khan, I., Saeed, K., & Khan, I. (2019). Nanoparticles: Properties, applications and toxicities. *Arabian journal of chemistry*, *12*(7), 908-931.

85. Kim, K., Yoo, J. D., Lee, S., Bae, M., Bae, J., Jung, W., & Han, J. W. (2017). A simple descriptor to rapidly screen CO oxidation activity on rare-earth metal-doped CeO2:

from experiment to first-principles. *ACS applied materials & interfaces*, *9*(18), 15449-15458.

86. Kim, D., Shin, K., Kwon, S. G., & Hyeon, T. (2018). Synthesis and biomedical applications of multifunctional nanoparticles. *Advanced Materials*, *30*(49), 1802309.

87. Kim, Y. G., Lee, Y., Lee, N., Soh, M., Kim, D., & Hyeon, T. (2024). Ceria-based therapeutic antioxidants for biomedical applications. *Advanced Materials*, *36*(10), 2210819.

88. Kinoshita, S. (Ed.). (2013). *Pattern Formations and Oscillatory Phenomena*. Newnes.

89. Kirkland, A. I., Jefferson, D. A., Duff, D. G., Edwards, P. P., Gameson, I., Johnson, B. F. G., & Smith, D. J. (1993). Structural studies of trigonal lamellar particles of gold and silver. *Proceedings of the Royal Society of London. Series A: Mathematical and Physical Sciences*, *440*(1910), 589-609.

90. Kirz, J., & Rarback, H. (1985). Soft x-ray microscopes. *Review of scientific instruments*, *56*(1), 1-13.

91. Kleijn, S. E., Lai, S. C., Koper, M. T., & Unwin, P. R. (2014). Electrochemistry of nanoparticles. *Angewandte Chemie International Edition*, *53*(14), 3558-3586.

92. Knoll, M., & Ruska, E. (1932). Das elektronenmikroskop. *Zeitschrift für physik*, 78, 318-339.

93. Korpanty, J., Gnanasekaran, K., Venkatramani, C., Zang, N., & Gianneschi, N. C. (2022). Organic solution-phase transmission electron microscopy of copolymer nanoassembly morphology and dynamics. *Cell Reports Physical Science*, *3*(3).

94. Kowal, A., Li, M., Shao, M., Sasaki, K., Vukmirovic, M. B., Zhang, J. H., Marinkovic, N. S., Liu, P., Frenkel, A. I. & Adzic, R. R. (2009). Ternary Pt/Rh/SnO2 electrocatalysts for oxidizing ethanol to CO2. *Nature materials*, *8*(4), 325-330.

95. Krans, N. A., Ahmad, N., Alloyeau, D., De Jong, K. P., & Zečević, J. (2019). Attachment of iron oxide nanoparticles to carbon nanofibers studied by *in-situ* liquid phase transmission electron microscopy. *Micron*, *117*, 40-46.

96. Kroto, H. W., Heath, J. R., O'Brien, S. C., Curl, R. F., & Smalley, R. E. (1985). C60: Buckminsterfullerene. *Nature*, *318*(6042), 162-163.

97. Kumar, S., Sahoo, P. K., & Satpati, A. K. (2017). Electrochemical and SECM investigation of MoS2/GO and MoS2/rGO nanocomposite materials for HER electrocatalysis. *ACS omega*, *2*(11), 7532-7545.

98. Kwon, S. G., Krylova, G., Phillips, P. J., Klie, R. F., Chattopadhyay, S., Shibata, T., Bunel, E. E., Liu, Y., Prakapenka, V. B., Lee, B. & Shevchenko, E. V. (2015). Heterogeneous nucleation and shape transformation of multicomponent metallic nanostructures. *Nature materials*, *14*(2), 215-223.

99. Lai, S. Y., Qiu, Y., & Wang, S. (2006). Effects of the structure of ceria on the activity of gold/ceria catalysts for the oxidation of carbon monoxide and benzene. *Journal of Catalysis*, *237*(2), 303-313.

100. Lam, E., Hrapovic, S., Majid, E., Chong, J. H., & Luong, J. H. (2012). Catalysis using gold nanoparticles decorated on nanocrystalline cellulose. *Nanoscale*, *4*(3), 997-1002.

101. LaMer, V. K., & Dinegar, R. H. (1950). Theory, production and mechanism of formation of monodispersed hydrosols. *Journal of the american chemical society*, *72*(11), 4847-4854.

102. Landon, P., Collier, P. J., Papworth, A. J., Kiely, C. J., & Hutchings, G. J. (2002). Direct formation of hydrogen peroxide from H 2/O 2 using a gold catalyst. *Chemical Communications*, (18), 2058-2059.

103. Laurent, S., Forge, D., Port, M., Roch, A., Robic, C., Vander Elst, L., & Muller, R. N. (2008). Magnetic iron oxide nanoparticles: synthesis, stabilization, vectorization, physicochemical characterizations, and biological applications. *Chemical reviews*, *108*(6), 2064-2110.

104. Lawrence, N. J., Brewer, J. R., Wang, L., Wu, T. S., Wells-Kingsbury, J., Ihrig, M. M., Wang, G., Soo, Y-L., Mei, W-N. & Cheung, C. L. (2011). Defect engineering in cubic cerium oxide nanostructures for catalytic oxidation. *Nano letters*, *11*(7), 2666-2671.

105. Lee, J., Nicholls, D., Browning, N. D., & Mehdi, B. L. (2021). Controlling radiolysis chemistry on the nanoscale in liquid cell scanning transmission electron microscopy. *Physical Chemistry Chemical Physics*, *23*(33), 17766-17773.

106. Lem, S. (1959). *Eden*. Kraków: Wydawnictwo Literackie.

107. Lem, S. (1964). *Niezwyciężony*. Kraków: Wydawnictwo Literackie.

108. Lem, S. (1964). *Summa Technologiae*. Kraków: Wydawnictwo Literackie.

109. Liu, W., & Flytzanistephanopoulos, M. (1995a). Total oxidation of carbon monoxide and methane over transition metal fluorite oxide composite catalysts: I. Catalyst composition and activity. *Journal of Catalysis*, *153*(2), 304-316.

110. Liu, W., & Flytzanistephanopoulos, M. (1995b). Total oxidation of carbon-monoxide and methane over transition metal fluorite oxide composite catalysts: II. Catalyst characterization and reaction-kinetics. *Journal of Catalysis*, *153*(2), 317-332.

111. Liu, P., & Nørskov, J. K. (2001). Ligand and ensemble effects in adsorption on alloy surfaces. *Physical Chemistry Chemical Physics*, *3*(17), 3814-3818.

112. Liu, Z. P., Jenkins, S. J., & King, D. A. (2005). Origin and activity of oxidized gold in water-gas-shift catalysis. *Physical Review Letters*, *94*(19), 196102.

113. Loh, N. D., Sen, S., Bosman, M., Tan, S. F., Zhong, J., Nijhuis, C. A., Král, P., Matsudaira, P. & Mirsaidov, U. (2017). Multistep nucleation of nanocrystals in aqueous solution. *Nature chemistry*, *9*(1), 77-82.

114. Lundahl, P., Stokes, R., Smith, E., Martin, R., & Graham, D. (2008). Synthesis and characterisation of monodispersed silver nanoparticles with controlled size ranges. *Micro & Nano Letters*, *3*(2), 62.

115. Mao, Y., Jiang, W., Wang, S., Liu, M., Xuan, S., Gong, X., & Leung, K. C. F. (2016). Mesoporous SiO2 yolk shell confined core-satellite Ag nanoparticles: Preparation and catalytic activity. *Journal of Alloys and Compounds*, *680*, 406-414.

116. Marinkovic, N. S., Li, M., & Adzic, R. R. (2020). Pt-Based Catalysts for Electrochemical Oxidation of Ethanol. Electrocatalysis, 1-39

117. Mayrhofer, K. J. J., Blizanac, B. B., Arenz, M., Stamenkovic, V. R., Ross, P. N., & Markovic, N. M. (2005). The impact of geometric and surface electronic properties of Pt-catalysts on the particle size effect in electrocatalysis. *The Journal of Physical Chemistry B*, *109*(30), 14433-14440.

118. Milazzo, R. G., Privitera, S., Litrico, G., Scalese, S., Mirabella, S., La Via, F., Lombardo, S. & Rimini, E. (2017). Formation, morphology, and optical properties of electroless deposited gold nanoparticles on 3C-SiC. *The Journal of Physical Chemistry C*, *121*(8), 4304-4311.

119. Mitchell, J. W. (1997). On the role of silver molecules in photographic sensitivity. *The Imaging Science Journal*, *45*(1), 2-7.

120. Montini, T., Melchionna, M., Monai, M., & Fornasiero, P. (2016). Fundamentals and catalytic applications of CeO2-based materials. *Chemical reviews*, *116*(10), 5987-6041.

121. Moseley, H. G. (1914). LXXX. The high-frequency spectra of the elements. Part II. *The London, Edinburgh, and Dublin Philosophical Magazine and Journal of Science*, 27(*160*), 703-713.

122. Mullen, G. M., Evans, E. J., Siegert, B. C., Miller, N. R., Rosselet, B. K., Sabzevari, I., Brush, A., Duan, Z. & Mullins, C. B. (2018). The interplay between ceria particle size, reducibility, and ethanol oxidation activity of ceria-supported gold catalysts. *Reaction Chemistry & Engineering*, *3*(1), 75-85.

123. Munoz, F. F., Acuña, L. M., Albornoz, C. A., Leyva, A. G., Baker, R. T., & Fuentes, R. O. (2015). Redox properties of nanostructured lanthanide-doped ceria spheres prepared by microwave assisted hydrothermal homogeneous co-precipitation. *Nanoscale*, *7*(1), 271-281.

124. Murphy, C. J., & Jana, N. R. (2002). Controlling the aspect ratio of inorganic nanorods and nanowires. *Advanced Materials*, *14*(1), 80-82.

125. Narayanan, R., & El-Sayed, M. A. (2004). Shape-dependent catalytic activity of platinum nanoparticles in colloidal solution. *Nano letters*, 4(*7*), 1343-1348.

126. Natter, H., & Hempelmann, R. (1996). Nanocrystalline copper by pulsed electrodeposition: the effects of organic additives, bath temperature, and pH. *The Journal of Physical Chemistry*, *100*(50), 19525-19532.

127. Niederberger, M., Garnweitner, G., Buha, J., Polleux, J., Ba, J., & Pinna, N. (2006). Nonaqueous synthesis of metal oxide nanoparticles: Review and indium oxide as case study for the dependence of particle morphology on precursors and solvents. *Journal of Sol-Gel Science and Technology*, *40*, 259-266.

128. Noh, S., An, H., Shin, J. H., & Shim, J. H. (2017). Unexpected catalytic behavior of core-satellite gold nanostructures towards electroreduction of oxygen. *Electrochemistry Communications*, *78*, 1-5.

129. Nyoka, M., Choonara, Y. E., Kumar, P., Kondiah, P. P., & Pillay, V. (2020). Synthesis of cerium oxide nanoparticles using various methods: implications for biomedical applications. *Nanomaterials*, *10*(2), 242.

130. Oja, S. M., Fan, Y., Armstrong, C. M., Defnet, P., & Zhang, B. (2016). Nanoscale electrochemistry revisited. *Analytical chemistry*, *88*(1), 414-430.

131. Okamoto, H. (2008). Ce-O (cerium-oxygen). *Journal of Phase Equilibria and Diffusion*, *29*, 545-547.

132. van Omme, J. T., Wu, H., Sun, H., Beker, A. F., Lemang, M., Spruit, R. G., Maddala, S., P., Rakowski, A., Friedrich, H., Patterson, J. P. & Garza, H. H. P. (2020). Liquid phase transmission electron microscopy with flow and temperature control. *Journal of Materials Chemistry C*, *8*(31), 10781-10790.

133. Oxtoby, D. W. (2000). Catching crystals at birth. *Nature*, *406*(6795), 464-465.

134. Palumbo, G., Doyle, D. M., El-Sherik, A. M., Erb, U., & Aust, K. T. (1991). Intercrystalline hydrogen transport in nanocrystalline nickel. *Scripta metallurgica et materialia*, *25*(3), 679-684.

135. Parashar, M., Shukla, V. K., & Singh, R. (2020). Metal oxides nanoparticles via sol–gel method: a review on synthesis, characterization and applications. *Journal of Materials Science: Materials in Electronics*, *31*(5), 3729-3749.

136. Parlinska-Wojtan, M., Tarnawski, T. R., Depciuch, J., De Marco, M. L., Sobczak, K., Matlak, K., Pawlyta, M., Schaeublin, R. & Chee, S. W. (2024). Understanding the Growth of Electrodeposited PtNi Nanoparticle Films Using Correlated *In-situ* Liquid Cell Transmission Electron Microscopy and Synchrotron Radiation. *Nano Letters*, 24(*40*), 12361-12367.

137. Parsons, D. F., Matricardi, V. R., Moretz, R. C., & Turner, J. N. (1974). Electron microscopy and diffraction of wet unstained and unfixed biological objects. *Advances in biological and medical physics*, 15, 161-270.

138. Perrichon, V., Laachir, A., Bergeret, G., Fréty, R., Tournayan, L., & Touret, O. (1994). Reduction of cerias with different textures by hydrogen and their reoxidation by oxygen. *Journal of the Chemical Society, Faraday Transactions*, *90*(5), 773-781.

139. Plakhova, T. V., Romanchuk, A. Y., Yakunin, S. N., Dumas, T., Demir, S., Wang, S., Minasian, S. G., Shuh, D. K., Tyliszczak, T., Shiryaev, A. A., Egorov, A. V., Ivanov, V. K. & Kalmykov, S. N. (2016). Solubility of nanocrystalline cerium dioxide: Experimental data and thermodynamic modeling. *The Journal of Physical Chemistry C*, *120*(39), 22615-22626.

140. Phokha, S., Pinitsoontorn, S., Chirawatkul, P., Poo-Arporn, Y., & Maensiri, S. (2012). Synthesis, characterization, and magnetic properties of monodisperse CeO 2 nanospheres prepared by PVP-assisted hydrothermal method. *Nanoscale research letters*, *7*, 1-13.

141. Phokha, S., Swatsitang, E., & Maensiri, S. (2015). Room-temperature ferromagnetism in pure CeO 2 nanoparticles prepared by a simple direct thermal decomposition. *Electronic Materials Letters*, *11*, 1012-1020.

142. Pushkarev, V. V., Kovalchuk, V. I., & d'Itri, J. L. (2004). Probing defect sites on the CeO2 surface with dioxygen. *The Journal of Physical Chemistry B*, *108*(17), 5341-5348.

143. Pokropivny, V., Lohmus, R., Hussainova, I., Pokropivny, A., & Vlassov, S. (2007). *Introduction to nanomaterials and nanotechnology* (pp. 45-100). Tartu: Tartu University Press.

144. Puntes, V. F., Zanchet, D., Erdonmez, C. K., & Alivisatos, A. P. (2002). Synthesis of hcp-Co nanodisks. *Journal of the American Chemical Society*, *124*(43), 12874-12880.

145. Quantum ESPRESSO (2022) *what can QE do* [Online]. Available at: https://www.quantum-espresso.org/what-can-qe-do/ (Accessed: 29 October 2024)

146. Radi, A., Pradhan, D., Sohn, Y., & Leung, K. T. (2010). Nanoscale shape and size control of cubic, cuboctahedral, and octahedral Cu− Cu2O core− shell nanoparticles on Si (100) by one-step, templateless, capping-agent-free electrodeposition. *ACS nano*, *4*(3), 1553-1560.

147. Radisic, A., Vereecken, P. M., Hannon, J. B., Searson, P. C., & Ross, F. M. (2006a). Quantifying electrochemical nucleation and growth of nanoscale clusters using real-time kinetic data. *Nano letters*, 6(*2*), 238-242.

148. Radisic, A., Vereecken, P. M., Searson, P. C., & Ross, F. M. (2006b). The morphology and nucleation kinetics of copper islands during electrodeposition. *Surface Science*, 600(*9*), 1817-1826.

149. Reed, K., Cormack, A., Kulkarni, A., Mayton, M., Sayle, D., Klaessig, F., & Stadler, B. (2014). Exploring the properties and applications of nanoceria: is there still plenty of room at the bottom?. *Environmental Science: Nano*, *1*(5), 390-405.

150. Rehr, J. J., Kas, J. J., Vila, F. D., Prange, M. P., & Jorissen, K. (2010). Parameter-free calculations of X-ray spectra with FEFF9. *Physical Chemistry Chemical Physics*, *12*(21), 5503-5513.

151. Reiss, P., Protiere, M., & Li, L. (2009). Core/shell semiconductor nanocrystals. *small*, *5*(2), 154-168.

152. Reverberi, A. P., Kuznetsov, N. T., Meshalkin, V. P., Salerno, M., & Fabiano, B. (2016). Systematical analysis of chemical methods in metal nanoparticles synthesis. *Theoretical Foundations of Chemical Engineering*, *50*, 59-66.

153. Ring, E. A., & de Jonge, N. (2012). Video-frequency scanning transmission electron microscopy of moving gold nanoparticles in liquid. *Micron*, *43*(11), 1078-1084.

154. Rodriguez, J. A., Wang, X., Liu, P., Wen, W., Hanson, J. C., Hrbek, J., Pérez, M. & Evans, J. (2007). Gold nanoparticles on ceria: importance of O vacancies in the activation of gold. *Topics in Catalysis*, *44*, 73-81.

155. Ross, J. R. (2018). *Contemporary Catalysis: Fundamentals and Current Applications*. Elsevier.

156. Roux, S., Garcia, B., Bridot, J. L., Salomé, M., Marquette, C., Lemelle, L., Gillet, P., Blum, L., Perriat, P. & Tillement, O. (2005). Synthesis, characterization of dihydrolipoic acid capped gold nanoparticles, and functionalization by the electroluminescent luminol. *Langmuir*, *21*(6), 2526-2536.

157. Ruska, E. (1942). Beitrag zur übermikroskopischen Abbildung bei höheren Drucken. *Kolloid-Zeitschrift*, 100(*2*), 212-219.

158. Ruska, E. (1956). Ein Hochauflosendes 100kV Elektronenmikroskop mit Kleinfelddurchstrahlung. Proc. Int. Conf Electron Microsc., London, 1954, pp. 673-693.

159. Schärtl, W. (2010). Current directions in core–shell nanoparticle design. *Nanoscale*, *2*(6), 829-843.

160. Schlick, S., Danilczuk, M., Drews, A. R., & Kukreja, R. S. (2016). Scavenging of hydroxyl radicals by ceria nanoparticles: effect of particle size and concentration. *The Journal of Physical Chemistry C*, *120*(12), 6885-6890.

161. Schmid, G. (1992). Large clusters and colloids. Metals in the embryonic state. *Chemical reviews*, *92*(8), 1709-1727.

162. Schneider, N. M., Norton, M. M., Mendel, B. J., Grogan, J. M., Ross, F. M., & Bau, H. H. (2014). Electron–water interactions and implications for liquid cell electron microscopy. *The Journal of Physical Chemistry C*, 118(*38*), 22373-22382.

163. Shannon, R. D. (1976). Revised effective ionic radii and systematic studies of interatomic distances in halides and chalcogenides. *Foundations of Crystallography*, *32*(5), 751-767.

164. Shao, M., Peles, A., & Shoemaker, K. (2011). Electrocatalysis on platinum nanoparticles: particle size effect on oxygen reduction reaction activity. *Nano letters*, *11*(9), 3714-3719.

165. Shao, M., Chang, Q., Dodelet, J. P., & Chenitz, R. (2016). Recent advances in electrocatalysts for oxygen reduction reaction. *Chemical reviews*, *116*(6), 3594-3657.

166. Sharma, P. A. W. A. N., & Bhargava, M. J. R. D. (2013). Applications and characteristics of nanomaterials in industrial environment. *Res Dev (IJCSEIERD)*, *3*(4), 63-72.

167. Silva, C. D., Corradini, P. G., Del Colle, V., Mascaro, L. H., de Lima, F. H. B., & Pereira, E. C. (2020). Pt/Rh/Pt and Pt/Ru/Pt multilayers for the electrochemical oxidation of methanol and ethanol. *Electrochimica Acta*, *354*, 136674.

168. Sneed, B. T., Young, A. P., & Tsung, C. K. (2015). Building up strain in colloidal metal nanoparticle catalysts. *Nanoscale*, *7*(29), 12248-12265.

169. Song, S., Wang, X., & Zhang, H. (2015). CeO2-encapsulated noble metal nanocatalysts: enhanced activity and stability for catalytic application. *NPG Asia Materials*, *7*(5), e179-e179.

170. De Souza, C. D., Nogueira, B. R., & Rostelato, M. E. C. (2019). Review of the methodologies used in the synthesis gold nanoparticles by chemical reduction. *Journal of Alloys and Compounds*, *798*, 714-740.

171. Spendelow, J. S., & Wieckowski, A. (2004). Noble metal decoration of single crystal platinum surfaces to create well-defined bimetallic electrocatalysts. *Physical Chemistry Chemical Physics*, 6(*22*), 5094-5118.

172. Su, H., Mehdi, B. L., Patterson, J. P., Sommerdijk, N. A. J. M., Browning, N. D., & Friedrich, H. (2019). Growth kinetics of cobalt carbonate nanoparticles revealed by liquid-phase scanning transmission electron microscopy. *The Journal of Physical Chemistry C*, *123*(41), 25448-25455.

173. Sun, Y., & Xia, Y. (2003). Triangular nanoplates of silver: synthesis, characterization, and use as sacrificial templates for generating triangular nanorings of gold. *Advanced Materials*, *15*(9), 695-699.

174. Sun, Y., Mayers, B., Herricks, T., & Xia, Y. (2003). Polyol synthesis of uniform silver nanowires: a plausible growth mechanism and the supporting evidence. *Nano letters*, *3*(7), 955-960.

175. Sun, Q., Zhang, X. Q., Wang, Y., & Lu, A. H. (2015). Recent progress on core-shell nanocatalysts. *Chinese Journal of Catalysis*, *36*(5), 683-691.

176. Suzuki, S., Ohta, Y., Kurimoto, T., Kuwabata, S., & Torimoto, T. (2011). Modulating the immobilization process of Au nanoparticles on TiO2 (110) by electrostatic interaction between the surface and ionic liquids. *Physical Chemistry Chemical Physics*, *13*(30), 13585-13593.

177. Swartz, S. L., Seabaugh, M. M., Holt, C. T., & Dawson, W. J. (2001). Fuel processing catalysts based on nanoscale ceria. *Fuel Cells Bulletin*, 4(*30*), 7-10.

178. Tan, L., Chen, D., Liu, H., & Tang, F. (2010). A silica nanorattle with a mesoporous shell: an ideal nanoreactor for the preparation of tunable gold cores. *Advanced Materials*, *43*(22), 4885-4889.

179. Tan, K. S., & Cheong, K. Y. (2013). Advances of Ag, Cu, and Ag–Cu alloy nanoparticles synthesized via chemical reduction route. *Journal of nanoparticle research*, *15*, 1-29.

180. Tang, J., Shi, Z., Berry, R. M., & Tam, K. C. (2015). Mussel-inspired green metallization of silver nanoparticles on cellulose nanocrystals and their enhanced catalytic reduction of 4-nitrophenol in the presence of β-cyclodextrin. *Industrial & Engineering Chemistry Research*, *54*(13), 3299-3308.

181. Taniguchi, N. (1974). On the basic concept of'nano-technology'. In *Proc. Intl. Conf. Prod. Eng. Tokyo, Part II, 1974*. Japan Society of Precision Engineering.

182. Tao, A., Sinsermsuksakul, P., Yang, P. (2006). Polyhedral Silver Nanocrystals with Distinct Scattering Signatures. *Angewandte Chemie International Edition*, 45(*28*), 4597–4601

183. Tarnawski, T., & Parlińska-Wojtan, M. (2024). Opportunities and Obstacles in LCTEM Nanoimaging–A Review. *Chemistry-Methods*, *4*(3), e202300041.

184. Thota, S., Wang, Y., & Zhao, J. (2018). Colloidal Au–Cu alloy nanoparticles: synthesis, optical properties and applications. *Materials Chemistry Frontiers*, *2*(6), 1074-1089.

185. Timoshenko, J., & Roldan Cuenya, B. (2020). *In-situ*/operando electrocatalyst characterization by X-ray absorption spectroscopy. *Chemical reviews*, *121*(2), 882-961.

186. Xia, Y., Xiong, Y., Lim, B., & Skrabalak, S. E. (2009). Shape-controlled synthesis of metal nanocrystals: simple chemistry meets complex physics? *Angewandte Chemie International Edition*, *48*(1), 60-103.

187. Xiong, Y., McLellan, J. M., Chen, J., Yin, Y., Li, Z. Y., & Xia, Y. (2005). Kinetically controlled synthesis of triangular and hexagonal nanoplates of palladium and their SPR/SERS properties. *Journal of the American Chemical Society*, *127*(48), 17118-17127.

188. Xiong, Y., & Xia, Y. (2007). Shape-controlled synthesis of metal nanostructures: the case of palladium. *Advanced Materials*, *19*(20), 3385-3391.

189. Xiong, Y., McLellan, J. M., Yin, Y., & Xia, Y. (2007). Synthesis of palladium icosahedra with twinned structure by blocking oxidative etching with citric acid or citrate ions. *Angewandte Chemie International Edition*, 46(*5*), 790-794.

190. Xu, Z., Hou, Y., & Sun, S. (2007). Magnetic core/shell Fe3O4/Au and Fe3O4/Au/Ag nanoparticles with tunable plasmonic properties. *Journal of the American Chemical Society*, *129*(28), 8698-8699.

191. Xu, Z., Lai, E., Shao-Horn, Y., & Hamad-Schifferli, K. (2012). Compositional dependence of the stability of AuCu alloy nanoparticles. *Chemical communications*, *48*(45), 5626-5628.

192. Xu, Z., Hao, X., Dai, Y., Kübel, C., Shaffer, M. S., Watts, B., & Li, Q. (2024). Synchrotron scanning transmission x-ray spectro-microscopy (STXM) characterisation of β-SiC nanowhisker AZ91 magnesium alloy nanocomposites. *Journal of Electron Spectroscopy and Related Phenomena*, *276*, 147477.

193. Yang, Z., Woo, T. K., & Hermansson, K. (2006). Effects of Zr doping on stoichiometric and reduced ceria: A first-principles study. *The Journal of chemical physics*, 124(*22*).

194. Yang, J., Andrei, C. M., Botton, G. A., & Soleymani, L. (2017). In liquid observation and quantification of nucleation and growth of gold nanostructures using *in-situ* transmission electron microscopy. *The Journal of Physical Chemistry C*, 121(*13*), 7435-7441.

195. Yang, Y., Feijóo, J., Briega-Martos, V., Li, Q., Krumov, M., Merkens, S., de Salvo, G., Chuvilin, A., Jin, J., Huang, H., Pollock, C. J., Salmeron, M. B., Wang, C., Muller, D. A., Abruna, H. D. & Yang, P. (2023). Operando methods: A new era of electrochemistry. *Current Opinion in Electrochemistry*, 101403.

196. Yao, S. Y., Xu, W. Q., Johnston-Peck, A. C., Zhao, F. Z., Liu, Z. Y., Luo, S., Senanayake, S. D., Martinez-Arias, A., Liu, W. J. & Rodriguez, J. A. (2014). Morphological effects of the nanostructured ceria support on the activity and stability of CuO/CeO_2 catalysts for the water-gas shift reaction. *Physical Chemistry Chemical Physics*, *16*(32), 17183-17195.

197. Yoon, J. H., Lim, J., & Yoon, S. (2012). Controlled assembly and plasmonic properties of asymmetric core–satellite nanoassemblies. *ACS nano*, *6*(8), 7199-7208.

198. You, X., He, R., Gao, F., Shao, J., Pan, B., & Cui, D. (2007). Hydrophilic high-luminescent magnetic nanocomposites. *Nanotechnology*, *18*(3), 035701.

199. Yu, H., Chen, M., Rice, P. M., Wang, S. X., White, R. L., & Sun, S. (2005). Dumbbell-like bifunctional Au− Fe3O4 nanoparticles. *Nano letters*, *5*(2), 379-382.

200. Yu, P., Hayes, S. A., O'Keefe, M., Stoffer, J. O., & O'Keefe, T. J. (2006). The phase stability of cerium species in aqueous systems: II. the Ce (III/IV)-H_2O-H_2O_2/O_2 systems. Equilibrium considerations and Pourbaix diagram calculations.

201. Wang, Z. L. (2000). Transmission electron microscopy of shape-controlled nanocrystals and their assemblies. *The Journal of Physical Chemistry B*, *104*(6), 1153-1175.

202. Wang, C., Xu, C., Zeng, H., & Sun, S. (2009). Recent progress in syntheses and applications of dumbbell-like nanoparticles. *Advanced materials*, *21*(30), 3045-3052.

203. Washio, I., Xiong, Y., Yin, Y., & Xia, Y. (2006). Reduction by the end groups of poly (vinyl pyrrolidone): a new and versatile route to the kinetically controlled synthesis of Ag triangular nanoplates. *Advanced Materials*, *18*(13), 1745-1749.

204. Watt, J., Cheong, S., & Tilley, R. D. (2013). How to control the shape of metal nanostructures in organic solution phase synthesis for plasmonics and catalysis. *Nano Today*, *8*(2), 198-215.

205. Watzky, M. A., & Finke, R. G. (1997). Transition metal nanocluster formation kinetic and mechanistic studies. A new mechanism when hydrogen is the reductant: slow, continuous nucleation and fast autocatalytic surface growth. *Journal of the American Chemical Society*, *119*(43), 10382-10400.

206. Weiner, R. G., Chen, D. P., Unocic, R. R., & Skrabalak, S. E. (2016). Impact of membrane-induced particle immobilization on seeded growth monitored by *in-situ* liquid scanning transmission electron microscopy. *Small*, *12*(20).

207. White, E. R., Singer, S. B., Augustyn, V., Hubbard, W. A., Mecklenburg, M., Dunn, B., & Regan, B. C. (2012). *In-situ* transmission electron microscopy of lead dendrites and lead ions in aqueous solution. *Acs Nano*, *6*(7), 6308-6317.

208. Wiley, B., Herricks, T., Sun, Y., & Xia, Y. (2004). Polyol synthesis of silver nanoparticles: use of chloride and oxygen to promote the formation of single-crystal, truncated cubes and tetrahedrons. *Nano Letters*, 4(*9*), 1733-1739.

209. Wiley, B., Sun, Y., Mayers, B., & Xia, Y. (2005). Shape-controlled synthesis of metal nanostructures: the case of silver. *Chemistry–A European Journal*, *11*(2), 454-463.

210. Wiley, B. J., Xiong, Y., Li, Z. Y., Yin, Y., & Xia, Y. (2006a). Right bipyramids of silver: a new shape derived from single twinned seeds. *Nano letters*, 6(*4*), 765-768.

211. Wiley, B. J., Wang, Z., Wei, J., Yin, Y., Cobden, D. H., & Xia, Y. (2006b). Synthesis and electrical characterization of silver nanobeams. *Nano letters*, *6*(10), 2273-2278.

212. Woehl, T. J., Park, C., Evans, J. E., Arslan, I., Ristenpart, W. D., & Browning, N. D. (2014). Direct observation of aggregative nanoparticle growth: Kinetic modeling of the size distribution and growth rate. *Nano letters*, *14*(1), 373-378.

213. Woehl, T. J., & Abellan, P. (2017). Defining the radiation chemistry during liquid cell electron microscopy to enable visualization of nanomaterial growth and degradation dynamics. *Journal of microscopy*, *265*(2), 135-147.

214. Wu, X., Lu, C., Zhou, Z., Yuan, G., Xiong, R., & Zhang, X. (2014). Green synthesis and formation mechanism of cellulose nanocrystal-supported gold

nanoparticles with enhanced catalytic performance. *Environmental Science: Nano*, *1*(1), 71-79.

215. Wu, T. S., Zhou, Y., Sabirianov, R. F., Mei, W. N., Soo, Y. L., & Cheung, C. L. (2016). X-ray absorption study of ceria nanorods promoting the disproportionation of hydrogen peroxide. *Chemical Communications*, 52(*28*), 5003-5006.

216. Wu, H., Li, T., Maddala, S. P., Khalil, Z. J., Joosten, R. R., Mezari, B., Hensen, E. J. M. de With, G., Friedrich, H., van Bokhoven, J. A. & Patterson, J. P. (2021). Studying reaction mechanisms in solution using a distributed electron microscopy method. *ACS nano*, *15*(6), 10296-10308.

217. Vollmer, C., & Janiak, C. (2011). Naked metal nanoparticles from metal carbonyls in ionic liquids: Easy synthesis and stabilization. *Coordination Chemistry Reviews*, *255*(17-18), 2039-2057.

218. Zhang, X., Zhao, Y., Xu, S., Yang, Y., Liu, J., Wei, Y., & Yang, Q. (2014a). Polystyrene sulphonic acid resins with enhanced acid strength via macromolecular self-assembly within confined nanospace. *Nature communications*, *5*(1), 1-9.

219. Zhang, X., Zhao, Y., & Yang, Q. (2014b). PS-SO3H@ phenylenesilica with yolk–double-shell nanostructures as efficient and stable solid acid catalysts. *Journal of catalysis*, *320*, 180-188.

220. Zheng, H., Smith, R. K., Jun, Y. W., Kisielowski, C., Dahmen, U., & Alivisatos, A. P. (2009). Observation of single colloidal platinum nanocrystal growth trajectories. *Science*, 324(*5932*), 1309-1312.

221. Zheng, Y., Qiao, J., Yuan, J., Shen, J., Wang, A. J., & Huang, S. (2018). Controllable synthesis of PtPd nanocubes on graphene as advanced catalysts for ethanol oxidation. *International Journal of Hydrogen Energy*, *43*(10), 4902-4911.

222. Zhou, W., Wu, J., & Yang, H. (2013). Highly uniform platinum icosahedra made by hot injection-assisted GRAILS method. *Nano letters*, *13*(6), 2870-2874.

223. Zhu, Y. J., & Chen, F. (2014). Microwave-assisted preparation of inorganic nanostructures in liquid phase. *Chemical reviews*, *114*(12), 6462-6555.

224. Zhu, G. Z., Prabhudev, S., Yang, J., Gabardo, C. M., Botton, G. A., & Soleymani, L. (2014). *In-situ* liquid cell TEM study of morphological evolution and degradation of Pt–Fe nanocatalysts during potential cycling. *The Journal of Physical Chemistry C*, 118(*38*), 22111-22119.

225. Zimmermann, P., Peredkov, S., Abdala, P. M., DeBeer, S., Tromp, M., Müller, C., & van Bokhoven, J. A. (2020). Modern X-ray spectroscopy: XAS and XES in the laboratory. *Coordination Chemistry Reviews*, *423*, 213466.

Scientific output

1) **Articles**
a) **Related to the PhD dissertation**

Tarnawski, T., & Parlińska-Wojtan, M. (2024). Opportunities and Obstacles in LCTEM Nanoimaging–a review. *Chemistry-Methods*, *4*(3), e202300041.

Parlinska-Wojtan, M., **Tarnawski, T. R.**, Depciuch, J., De Marco, M. L., Sobczak, K., Matlak, K., Pawlyta, M., Schaeublin, R. E. & Chee, S. W. (2024). Understanding the Growth of Electrodeposited PtNi Nanoparticle Films Using Correlated In Situ Liquid Cell Transmission Electron Microscopy and Synchrotron Radiation. *Nano Letters*, *24*(40), 12361-12367.

Parlinska-Wojtan, M., Depciuch, J., **Tarnawski, T.**, Tomczyk, W., Pawlyta, M. & Sobczak, K. (in preparation). Synthesis, dissolution and Au decoration of Ce_xO_y nanoparticles by *in-situ* liquid cell TEM.

Depciuch, J., **Tarnawski, T.**, Tomczyk, W., Maximenko, A., Matlak, K., Sobczak, K., Pawlik, P. & Parlinska-Wojtan, M. (in preparation). Evolution of CeO_2 and Ce_2O_3 phases in Ce_xO_y high surface nanospheres supporting gold catalysts during Ethanol Oxidation Reaction – XANES & operando IRRAS study.

b) **Other articles**

Łukowiec, D., Wasiak, T., Janas, D., Drzymała, E., Depciuch, J., **Tarnawski, T.**, Kubacki, J., Wacławek, S. & Radoń, A. (2022). Pd decorated Co–Ni nanowires as a highly efficient catalyst for direct ethanol fuel cells. *International Journal of Hydrogen Energy*, *47*(97), 41279-41293.

2) **Conferences**

6th International Symposium on Surface Imaging/Spectroscopy at the Solid/Liquid Interface ISSIS, IKiFP PAN, Kraków 6-9 VI 2021, poster, "Platinum decorated SnO2 mesoporous spheres as catalysts for ethanol oxidation reaction".

Joint Meeting of PSRS and SOLARIS Centre Users, PSRS oraz Narodowe Centrum Promieniowania Synchrotronowego SOLARIS, Wydział Fizyki, Astronomii i Informatyki Stosowanej UJ Kraków, 20-23 IX 2022, poster, „LC-TEM observations of growth and dissolution of CeO_2 NPs and their decoration by Au NPs".

Transhumanism: Ideas, strategies and doubts, Polish Transhumanism Society, 21-22 V 2022, organization and presentation: "Nanotechnology and alternative fuel cells".

Joint Meeting of PSRS and SOLARIS Centre Users, PSRS oraz Narodowe Centrum Promieniowania Synchrotronowego SOLARIS, Wydział Fizyki, Astronomii i Informatyki Stosowanej UJ Kraków, 20-23 IX 2022, poster, „LC-TEM observations of growth and dissolution of CeO_2 NPs and their decoration by Au NPs".

36th European Conference on Surface Science (ECOSS 36), 28 VIII - 1 IX 2023, Łódź, Polska; poster: "Growth of PtNi Nanoparticles Films: correlation between in-situ Liquid Cell Transmission Electron Microscopy and bulk Experiments".

VIII Konferencja Naukowa „Bezpieczeństwo energetyczne – filary i perspektywa rozwoju", 11-12 IX 2023, Rzeszów, Polska; prezentacja ustna: „Nanokatalizatory oparte na miedzi do zastosowań w ogniwach paliwowych zasilanych etanolem".

The Liquid Phase Electron Microscopy GRC Imaging and Elucidating Nanomaterial Formation, Morphology and Dynamics, 28 I - 2 II 2024, Lucca (Barga), Lucca, Włochy; poster: "Real time observation of Cu2O nanocubes formation in the Liquid Cell TEM".

List of Figures

List of Tables

List of Movies

Movie 1: Synthesis of ceria NPs induced by the electron beam in TEM. Corresponding to **Figure 18**.

Movie 2: Radiolytic dissolution of ceria NPs in TEM, while the precursor solution is flowing through the liquid cell. Corresponding to **Figure 19**.

Movie 3: Formation of ceria nanostructures on pre-synthesised ceria NAs from the precursor solution in TEM. Corresponding to **Figure 20(a)**.

Movie 4: Radiolytic dissolution of the pre-synthesised ceria NAs in TEM, while the precursor solution is flowing through the liquid cell. Corresponding to **Figure 20(b)**.

Movie 5: Pre-synthesised ceria NAs in TEM, while water is flowing through the liquid cell with flow rate 0.8 µl/s. Corresponding to **Figure 21(a)**.

Movie 6: Radiolytic dissolution of the pre-synthesised ceria NAs in TEM, while water is flowing through the liquid cell with flow rate 0.5 µl/s. Corresponding to **Figure 21(b)**.

Movie 7: Synthesis of Au NPs on ceria NAs induced by the electron beam in TEM. Dynamic experiment. Corresponding to **Figure 22**.

Movie 8: Synthesis of Au NPs on ceria NAs induced by the electron beam in TEM. Static experiment. Corresponding to **Figure 23**.

Movie 9: Synthesis of Au NPs on ceria NAs induced by the electron beam in TEM. Concentration of the Au precursor solution 0.1 mM. Corresponding to **Figure 26**.

Appendix

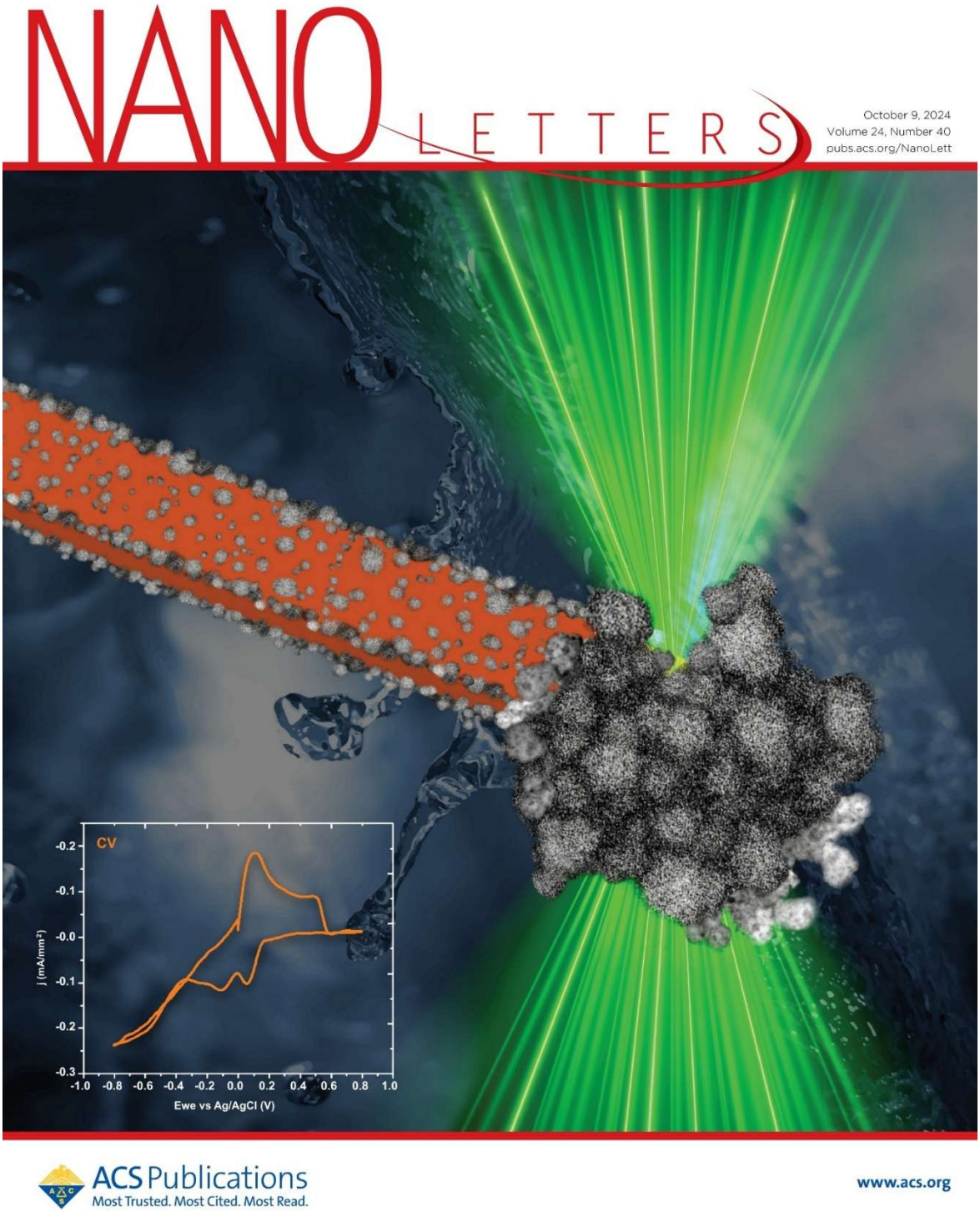

Nano Lett. 2024, 24, 40, 12361-12367
https://doi.org/10.1021/acs.nanolett.4c02228
Published August 15, 2024